NICOLAUS COPERNICUS
UNIVERSITY
IN TORUŃ
Faculty of Physics, Astronomy
and Informatics

RUHR
UNIVERSITÄT
BOCHUM
RUB

DOCTORAL THESIS

Thermal and Electrical Properties of Nanolayer Polymers

Author: Ameneh Mikaeeli

Double Degree-Ph.D. Student

Nicolaus Copernicus University in Toruń, Poland

(Faculty of Physics, Astronomy and Informatics)

&

Ruhr University Bochum, Germany

(Faculty of Physics and Astronomy)

Supervisors:

Dr. hab. Michał Pawlak Prof. at NCU

Prof. Dr. Andreas D. Wieck

Toruń, 2026

PhD Thesis

Nicolaus Copernicus University in Toruń, Poland
Faculty of Physics, Astronomy and Informatics
Ruhr University Bochum, Germany
Faculty of Physics and Astronomy

Title:

Thermal and Electrical Properties of Nanolayer Polymers

Author

Ameneh Mikaeeli
Ameneh.mikaeeli@doktorant.umk.pl
Ameneh.mikaeeli@ruhr-uni-bochum.de

Supervisors

Dr. hab. Michał Pawlak Prof. at NCU
Prof. Dr. Andreas D. Wieck

June 2026

Abstract

This doctoral thesis investigates the electrical and thermal transport properties of conductive poly(3,4-ethylenedioxythiophene):poly(styrenesulfonate) (PEDOT:PSS) thin films. Due to their high electrical conductivity, optical transparency, mechanical flexibility, and solution processability, PEDOT:PSS materials have attracted considerable attention for applications in flexible electronics, transparent electrodes, sensors, photovoltaic devices, and thermoelectric materials. However, the thermal transport behavior of conductive polymers and its relationship with electrical transport remain incompletely understood. To address this, PEDOT:PSS (F HC Solar) thin films with varying morphology, thickness, conductivity, and anisotropic structure were fabricated. The effects of film thickness, substrate type, and temperature on charge and heat transport were investigated using glass, silicon-doped gallium arsenide (GaAs:Si), and indium tin oxide (ITO)-coated glass substrates. Electrical transport properties were investigated using Hall-effect measurements in the Van der Pauw configuration and conductive atomic force microscopy (C-AFM), while thermal transport properties were studied using photothermal infrared radiometry (PTR) and thermoreflectance (TR) techniques, enabling determination of both cross-plane and in-plane thermal conductivity. The obtained results showed that charge transport in this particular PEDOT:PSS (F HC Solar) thin films occurs via tunneling mechanisms rather than conventional hopping transport, independent of film thickness and substrate type. PEDOT:PSS thin films deposited on ITO-coated glass substrates exhibited very high electrical conductivity values, which is highly important for transparent electrode applications in photovoltaic and solar-cell technologies. A major contribution of this work is the development of a custom-built electric-field-assisted spin-coating system, which enabled simultaneous application of a lateral electric field during thin-film deposition together with real-time current monitoring during film formation and solidification. The applied electric field induced directional reorientation of PEDOT:PSS dipolar structures, resulting in anisotropic electrical conductivity and directional charge transport within the thin films.

Another important contribution of this thesis is the comprehensive investigation of thermal transport properties in PEDOT:PSS thin films, which remains a relatively unexplored topic in the literature. Both theoretical and experimental analyses of in-plane and cross-plane thermal and electrical conductivities were performed, and the correlation between thermal and electrical transport was systematically investigated using the Wiedemann-Franz law. The results demonstrated that enhanced electrical conductivity was accompanied by enhanced thermal conductivity, indicating an electronic contribution to heat propagation and highlighting the importance of coupled transport behavior for thermoelectric applications. Furthermore, using C-AFM local charge concentrations and conductive regions on the PEDOT:PSS thin-film surface were studied. In agreement with the tunneling transport model, the observed local current variations indicate charge transport between conductive polymer segments associated with polaronic and bipolaronic structures within the polymer network. This thesis provides a comprehensive investigation of coupled electrical and thermal transport phenomena in PEDOT:PSS (F HC Solar) thin films and contributes to the understanding and optimization of conductive polymer materials for flexible electronic, thermoelectric, and energy-conversion applications.

Abstrakt

Niniejsza rozprawa doktorska bada właściwości transportu elektrycznego i cieplnego przewodzących cienkich warstw poli(3,4-etylenodioksytiofenu):poli(styrenosulfonianu) (PEDOT:PSS). Ze względu na wysoką przewodność elektryczną, przezroczystość optyczną, elastyczność mechaniczną oraz możliwość przetwarzania z roztworu, materiały PEDOT:PSS wzbudziły znaczne zainteresowanie w zastosowaniach obejmujących elastyczną elektronikę, przezroczyste elektrody, czujniki, urządzenia fotowoltaiczne oraz materiały termoelektryczne. Jednak mechanizm transportu ciepła w przewodzących polimerach oraz ich związek z transportem elektrycznym pozostają nadal nie w pełni zrozumiane. W celu rozwiązania tego problemu wytworzono cienkie warstwy PEDOT:PSS (F HC Solar) o zróżnicowanej morfologii, grubości, przewodności i strukturze anizotropowej. Wpływ grubości warstwy, rodzaju podłoża i temperatury na transport ładunku oraz ciepła badano z wykorzystaniem podłoży szklanych, arsenku galu domieszkowanego krzemem (GaAs:Si) oraz szkła pokrytego tlenkiem indu i cyny (ITO). Właściwości transportu elektrycznego analizowano za pomocą pomiarów efektu Halla w konfiguracji Van der Pauwa oraz przewodzącej mikroskopii sił atomowych (C-AFM), natomiast właściwości transportu cieplnego badano metodami fototermicznej radiometrii podczerwonej (PTR) i termoreflektancji (TR), co umożliwiło wyznaczenie przewodności cieplnej zarówno w płaszczyźnie warstwy, jak i w kierunku prostopadłym do niej. Uzyskane wyniki wykazały, że transport ładunku w badanych cienkich warstwach PEDOT:PSS (F HC Solar) zachodzi poprzez mechanizmy tunelowe, a nie poprzez konwencjonalny transport skokowy, niezależnie od grubości warstwy i rodzaju podłoża. Cienkie warstwy PEDOT:PSS osadzone na podłożach szklanych pokrytych ITO wykazywały bardzo wysoką przewodność elektryczną, co ma kluczowe znaczenie dla zastosowań przezroczystych elektrod w technologiach fotowoltaicznych i ogniwach słonecznych. Istotnym osiągnięciem tej pracy jest opracowanie autorskiego systemu spin-coatingu wspomaganego polem elektrycznym, który umożliwił jednoczesne przyłożenie bocznego pola elektrycznego podczas osadzania cienkiej warstwy oraz monitorowanie prądu w czasie rzeczywistym w trakcie formowania i utwardzania filmu. Zastosowane pole elektryczne wywołało kierunkową reorientację dipolowych struktur PEDOT:PSS, prowadząc do anizotropowej przewodności elektrycznej oraz kierunkowego transportu ładunku w cienkich warstwach.

Kolejnym ważnym wkładem tej rozprawy jest kompleksowe badanie właściwości transportu cieplnego w cienkich warstwach PEDOT:PSS, które pozostaje stosunkowo słabo zbadanym zagadnieniem w literaturze. Przeprowadzono zarówno teoretyczne, jak i eksperymentalne analizy przewodności cieplnej i elektrycznej w płaszczyźnie warstwy oraz w kierunku prostopadłym do niej, a korelację pomiędzy transportem cieplnym i elektrycznym systematycznie analizowano z wykorzystaniem prawa Wiedemann–Franz. Wyniki wykazały, że wzrostowi przewodności elektrycznej towarzyszył wzrost przewodności cieplnej, co wskazuje na elektroniczny udział w propagacji ciepła i podkreśla znaczenie sprzężonych procesów transportowych dla zastosowań termoelektrycznych. Ponadto, przy użyciu C-AFM badano lokalne koncentracje ładunku oraz przewodzące obszary na powierzchni cienkich warstw PEDOT:PSS. Zgodnie z modelem transportu tunelowego zaobserwowane lokalne zmiany natężenia prądu wskazują na transport ładunku pomiędzy przewodzącymi segmentami polimeru związanymi ze strukturami polaronowymi i bipolaronowymi w sieci polimerowej. Niniejsza rozprawa przedstawia kompleksowe badanie sprzężonych zjawisk transportu elektrycznego i cieplnego w cienkich warstwach PEDOT:PSS (F HC Solar) oraz wnosi istotny wkład w zrozumienie i optymalizację przewodzących materiałów polimerowych przeznaczonych do zastosowań w elastycznej elektronice, urządzeniach termoelektrycznych i technologiach konwersji energii.

For my parents Sarah and NourAli

Acknowledgments

I would like to express my sincere gratitude to all those who supported me throughout the course of my doctoral studies and the completion of this dissertation.

First and foremost, I would like to express my deepest gratitude to my supervisors, Dr. hab. Michał Pawlak Prof. at NCU and Prof. Dr. Andreas D. Wieck, for their continuous guidance, valuable discussions, encouragement, and support throughout this research work. Their scientific insight and mentorship have been invaluable to my academic development.

I would also like to sincerely thank Dr. Nathan Jukam for his support and assistance during my research stay at Ruhr University Bochum (RUB), especially with laboratory work and experimental activities. Special thanks to Ms. Nadine Viteritti for patiently teaching me how to work with laboratory equipment at RUB. I am also grateful to Dr. Arne Ludwig at RUB for his guidance and support during my study at RUB. I would like to thank Peter Zajac for his help with the C-AFM device and for his assistance with laboratory construction and technical work at RUB.

My sincere appreciation to Prof. Dorota Korte for hosting me in her laboratory at the University of Nova Gorica, Slovenia, where I had the opportunity to learn thermal methods, particularly photothermal beam deflection and thermal lens. I am especially grateful for our scientific collaboration and the paper we published together. I would also like to thank Dr. Humberto Cabrera for hosting me in his laboratory at ICTP, Italy, where he introduced me to the thermal lens method and collaborated with me on a scientific publication.

I am grateful to Dr. Robert Szczęsny from the Faculty of Chemistry at NCU for his assistance with thin-film deposition for the doped PEDOT:PSS samples investigated in this dissertation. I would also like to sincerely thank Dr. Dariusz Dziczek from the Faculty of Physics at NCU for his support and help with thermal experimental setups (PTR and TR). I gratefully acknowledge Dr. Aleksandra Wierzbicka and Dr. Monika Ożga (Institute of Physics, Polish Academy of Sciences, Warsaw, Poland) for their assistance with the XRD and SEM measurements, respectively. I would like to express my heartfelt gratitude to Prof. Dr. Katarzyna Hrynkiewicz, former Director of the Doctoral School Academia Copernicana, for her support and kindness during her time as Director and throughout my doctoral studies. I would also like to express my sincere gratitude to the secretariats and administrative staff at RUB and NCU, especially Justyna, Dany, and Heike for their help and kindness.

I would like to thank my family for their unconditional love and support. My great brothers, Aziz, Rasoul and Mansour and the best sister a person can have Asieh. I would also like to thank the friends I met during my doctoral studies. Markus Sifft, one of the first friends I met at RUB, whose energy, and inspiring spirit always motivated me as well as Jan Fischer, Armin Ghorbanietemad, and Philip for the wonderful times we shared at RUB- our walks through the botanical garden after lunch, and our special Raman/Mango-lassi moments, which I will always remember. And thank to Prof. Daniel Hägele. Special thanks to my wonderful office mates and dear friends at RUB, Danial Kohminaei, Skeeb Sadat, and Jannis Rüggen, for our memorable evening gatherings, trips, sushi times, and countless happy moments together. Their friendship made my time at RUB truly unforgettable. Jannick Dechou for his warm heart, and inspiring friendship. I would also like to thank Lennart Anderson for his kindness and the interesting conversations we shared, and Amar Alok for his kindness.

Table of Contents

List of Figures

List of Tables

List of Abbreviations, Symbols and Units

AC	Alternating Current
AFM	Atomic Force Microscopy
AOM	Acousto-Optic Modulator
C-AFM	Conductive Atomic Force Microscopy
CAS	Chemical Abstracts Service
CNF	Cellulose Nanofiber
CP	Conductive Polymer
CTR	Thermoreflectance Coefficient
$CuCl_2$	Copper(II) Chloride
$CuCl_2 \cdot xH_2O$	Copper(II) Chloride Hydrate
DC	Direct Current
DMSO	Dimethyl Sulfoxide
DPSS	Diode-Pumped Solid-State Laser
EDOT	3,4-Ethylenedioxythiophene
EF	Fermi Level
F HC Solar	Highly Conductive PEDOT:PSS Formulation (Ossila)
FDTR	Frequency-Domain Thermoreflectance
FIT	Fluctuation-Induced Tunneling
FTIR	Fourier Transform Infrared Spectroscopy
GaAs:Si	Silicon-Doped Gallium Arsenide
GO	Graphene Oxide
ICP	Intrinsically Conducting Polymer
ITO	Indium Tin Oxide
LbL	Layer-by-Layer
MCT	Mercury Cadmium Telluride
MVRH	Mott Variable-Range Hopping
OLED	Organic Light-Emitting Diode
OPV	Organic Photovoltaic
PANI	Polyaniline
PEDOT	Poly(3,4-ethylenedioxythiophene)
PEDOT:PSS	Poly(3,4-ethylenedioxythiophene):Poly(styrenesulfonate)
PPy	Polypyrrole
PTR	Photothermal Infrared Radiometry
PSS	Poly(styrenesulfonate)
PVA	Poly(vinyl alcohol)
SEM	Scanning Electron Microscopy
SMU	Source Measure Unit
SO_3H	Sulfonic Acid Group
SSR	Schaefer–Siebert–Roth Model
TR	Thermoreflectance
TR-PTR	Combined Thermoreflectance–Photothermal Infrared Radiometry
UPS	Ultraviolet Photoelectron Spectroscopy
UV-Vis	Ultraviolet–Visible Spectroscopy

VDP	Van der Pauw
VRH	Variable-Range Hopping
VRH-3D	Three-Dimensional Variable-Range Hopping
WF Law	Wiedemann–Franz Law
XRD	X-ray Diffraction
Al	Aluminium
Au	Gold
In	Indium
ZT	Thermoelectric Figure of Merit
S	Second
Min	Minute
χ^2	Reduced Chi-Square
η	Thermal Anisotropy Coefficient (Anisotropy Ratio)
α	Thermal Diffusivity
k_e	Electronic Thermal Conductivity
$k_{\parallel}$	In-Plane Thermal Conductivity
$k_{\perp}$	Cross-Plane Thermal Conductivity
$k_{\parallel}/k_{\perp}$	Ratio of Thermal Anisotropy
ρC	Volumetric Heat Capacity
ω	Angular Modulation Frequency
λ	Hankel Transform Variable
θ_{TR}	Complex Thermoreflectance Signal
$\Delta R/R$	Relative Reflectivity Change
C_{TR}	Thermoreflectance Coefficient
ΔT	Temperature Oscillation Amplitude
E	Infrared Emission/Radiance
A/V	Ampere per Volt (Current Amplifier Gain Unit)
K	Kelvin
MHz	Megahertz
Hz	Hertz
nV	Nanovolt
GΩ	Gigaohm
mW	Milliwatt
$S(k_r)$	sensitivity vector
$S(C_{eff})$	(volumetric heat capacity)
σ	Electrical conductivity
$R_{\parallel}$	Resistance Parallel to the Applied Electric Field
$R_{\perp}$	Resistance Perpendicular to the Applied Electric Field
$\sigma_{\parallel}$	Electrical Conductivity Parallel to the Applied Electric Field
$\sigma_{\perp}$	Electrical Conductivity Perpendicular to the Applied Electric Field
Λ_e	Electronic Thermal Conductivity
Λ_{ph}	Phonon Thermal Conductivity
ZT	Thermoelectric Figure of Merit
S	Seebeck Coefficient
L	Lorenz Number

T	Absolute Temperature
γ (E)	Field-Dependent Enhancement Factor
σ_0 (T)	Zero-Field Conductivity
I	Electric Current
V	Applied Voltage
L	Film Thickness
Rq	Root Mean Square Surface Roughness
Ra	Average Surface Roughness
°C	Degree Celsius
eV	Electron Volt
mV	Millivolt
V	Volt
V mm^{-1}	Volt per Millimetre
A	Ampere
µA	Microampere
nA	Nanoampere
Ω	Ohm
Ω cm	Ohm Centimetre
S/cm	Siemens per Centimetre
wt.%	Weight Percent
rpm	Rotation Per Minute
nm	Nanometre
µm	Micrometre
mm	Millimetre
mm^2	Square Millimetre
μm^2	Square Micrometre
W cm^{-2}	Watt per Square Centimetre

Chapter 1
Introduction and Literature Review

1.1 Intrinsically Conducting Polymers (ICPs)

1.1.1 Historical Background of Conductive Polymers

Intrinsically conducting polymers (ICPs) have attracted considerable scientific interest over the past several decades, particularly in organic electronics and optoelectronics [1-7]. Although early observations related to electrically active polymers can be traced back to investigations performed during the nineteenth century on electrically stimulated aniline-based systems [8], the modern development of conductive polymer science began much later with the discovery of highly conductive doped conjugated polymers. A major breakthrough occurred in 1977 when it was demonstrated that polyacetylene could exhibit high electrical conductivity after halogen doping [9]. This discovery represented a fundamental milestone in polymer physics because it showed that organic polymeric materials could possess electronic properties comparable to those of semiconductors and, under certain conditions, even to those of metallic systems. Despite the limited environmental stability and poor practical applicability of early polyacetylene films, this achievement initiated intensive research into electrically conductive organic materials. Following the discovery of conductive polyacetylene, numerous conjugated polymer systems were investigated, including polyaniline (PANI), polypyrrole (PPy), and polyphenylene derivatives [10]. Continued research into conjugated polymer systems revealed that thiophene-based polymers exhibit particularly favorable stability and transport properties. Shortly afterward, electrically conductive polythiophenes were successfully synthesized via oxidation, leading to the development of various polythiophene derivatives [11]. Among these materials, PEDOT, first introduced in the late 1980s, emerged as one of the most important conductive polymers due to its relatively high conductivity, good environmental stability, optical transparency, and electrochemical performance [12]. However, pristine PEDOT presents several practical limitations, including poor solubility and limited processability, which restrict its direct application in solution-based fabrication technologies. To overcome these limitations, PEDOT was combined with PSS, forming the PEDOT:PSS polymer complex [12,13]. The incorporation of PSS significantly improved water dispersibility and enabled straightforward thin-film fabrication via low-cost solution processing. The development of PEDOT:PSS represented an important advancement in the field of conductive polymers because it combined relatively high electrical conductivity with excellent processability, optical transparency, and mechanical flexibility [13,14]. Consequently, PEDOT:PSS has become one of the most extensively studied conductive polymer systems for applications including organic light-emitting diodes, flexible electronics, transparent electrodes, thermoelectric devices, sensors, and energy conversion systems. In recent years, conductive polymers have gained increasing attention as potential alternatives to conventional transparent conductive materials such as ITO [15,16]. Unlike brittle inorganic oxides, conductive polymers can be deposited on flexible substrates and processed using scalable manufacturing techniques, making them highly attractive for next-generation flexible and wearable electronic devices.

1.2 PEDOT:PSS and Transport Characterization Challenges

PEDOT:PSS is one of the most widely studied intrinsically conducting polymers due to its unique combination of electrical conductivity, optical transparency, mechanical flexibility, and solution processability [17-22]. In contrast to conventional inorganic conductive materials, PEDOT:PSS can be deposited from aqueous solution using low-cost fabrication methods such as spin coating and printing techniques, making it highly attractive for large-area and flexible electronic applications. Despite its technological importance, PEDOT:PSS remains a complex material from the perspective of transport physics. The material consists of conductive PEDOT-rich domains surrounded by insulating or weakly conductive PSS regions, resulting in a heterogeneous and phase-separated morphology [23, 24]. Consequently, the electrical transport properties strongly depend on structural disorder, film morphology, substrate interactions, additives, film thickness, and processing conditions. In many cases, charge transport cannot be adequately described using conventional band transport models and instead involves thermally activated hopping or tunneling processes between conductive regions [25, 29]. In addition to electrical transport, thermal transport in PEDOT:PSS is governed by complex interactions between phonon-mediated heat conduction and possible charge-carrier-assisted heat transport. Due to the anisotropic organization of polymer chains and conductive pathways, significant differences may exist between in-plane and cross-plane transport properties. Understanding the relationship between electrical conductivity and thermal conductivity is therefore essential for evaluating transport mechanisms in conductive polymer systems. The characterization of transport properties in PEDOT:PSS thin films presents several experimental challenges. Electrical and thermal transport measurements performed at different length scales may probe different physical processes, while substrate effects and directional anisotropy can significantly influence the measured properties. Furthermore, no single experimental technique is sufficient to fully characterize the coupled electrical and thermal transport behavior of conductive polymer systems. For this reason, complementary characterization methods are required to investigate transport phenomena in PEDOT:PSS thin films. In the present work, electrical transport properties were investigated using Van der Pauw four-probe measurements and C-AFM, while thermal transport behavior was studied using PTR and TR techniques. Furthermore, the Wiedemann-Franz law was used to examine the correlation between the thermal and electrical conductivities of PEDOT:PSS thin films. The combination of these methods enables the investigation of transport phenomena across multiple length scales and transport directions, allowing correlations among morphology, electrical conductivity, thermal conductivity, and anisotropic behavior to be established.

1.3 Research Hypothesis

The present doctoral thesis is based on the hypothesis that the combined investigation of electrical and thermal transport properties, together with the analysis of their correlation, enables a comprehensive characterization of transport phenomena in nanostructured conductive polymers. In particular, it is hypothesized that variations in morphology, anisotropy, substrate properties, and processing conditions directly influence both charge and heat transport mechanisms in conductive polymers, especially in PEDOT:PSS thin films. Furthermore, the application of different theoretical transport models is expected to provide deeper insight into the underlying charge-transport mechanisms and their contributions to thermal transport.

To verify this hypothesis, PEDOT:PSS (F HC Solar) thin films with different morphologies, thicknesses, conductivities, and anisotropic structures were fabricated and systematically investigated using complementary transport characterization techniques. Electrical transport properties were studied using Hall-effect measurements based on the Van der Pauw configuration, including temperature-dependent electrical conductivity measurements. In addition, conductive atomic force microscopy (C-AFM) was used to investigate nanoscale charge-transport pathways and local conductivity. To elucidate the dominant charge-transport mechanisms, the experimental results were analyzed using various theoretical models, including tunneling and hopping. Thermal transport properties were characterized using photothermal infrared radiometry (PTR) and thermoreflectance (TR) techniques to determine cross-plane and in-plane thermal conductivities, respectively. Furthermore, the Wiedemann–Franz law was employed to estimate the electronic contribution to heat transport and assess the relationship between charge-carrier transport and thermal conductivity. Special attention was given to the correlation between electrical and thermal transport properties, substrate-induced effects, anisotropic transport behavior, and the role of morphology in determining transport performance in conductive polymer thin films.

1.4 Aim and Objectives of the Thesis

The main aim of this doctoral thesis is to investigate the electrical and thermal transport properties of PEDOT:PS thin films and to demonstrate that combined thermal and electrical characterization methods provide comprehensive information about charge transport in this conductive polymer. To achieve this aim, the following objectives were defined:

1. To fabricate PEDOT:PSS thin films with controlled thickness, morphology, and conductivity using different deposition and processing approaches.
2. To investigate the influence of substrate type, film thickness, and temperature on the electrical and thermal transport properties of PEDOT:PSS thin films.
3. To identify the dominant charge transport mechanisms governing conductivity in PEDOT:PSS using theoretical transport models (Hopping and Tunneling models).
4. To characterize thermal transport properties and evaluate thermal anisotropy in PEDOT:PSS thin films as well as the relation between thermal and electrical anisotropy.
5. To investigate the contribution of charge carriers to heat propagation and assess the applicability of the Wiedemann-Franz framework in PEDOT:PSS thin films.
6. To fabricate PEDOT:PSS thin films by spin-coating under a laterally applied electric field during thin film solidification and investigate their anisotropic electrical conductivity.
7. To perform current-time and voltage-time measurements on samples fabricated under an applied electrical field to investigate ionic transport processes within the polymer and to gain a deeper understanding of the mechanisms governing charge transport in PEDOT:PSS thin films during polymer solidification.
8. To investigate the local distribution of charge carriers and nanoscale conductivity variations in PEDOT:PSS thin films using C-AFM, and to determine the spatially resolved cross-plane electrical conductivity in different regions of the films in order to gain insight into local charge transport pathways, conductivity heterogeneities, and their relationship to film morphology and microstructure.

1.5 Scope of the Thesis

This doctoral thesis focuses on the experimental and theoretical investigation of the electrical and thermal transport properties of PEDOT:PSS thin films prepared by solution-based deposition methods. The work includes the study of substrate-dependent transport behavior, film-thickness effects, thermal and electrical anisotropy, and temperature-dependent transport mechanisms. The investigation is limited to PEDOT:PSS-based conductive polymer thin films deposited on glass, indium tin oxide (ITO)-coated glass, and GaAs:Si substrates. The thesis emphasizes characterizing transport using complementary electrical and thermal measurement techniques and does not include large-scale device fabrication or advanced quantum-mechanical modeling.

1.6 Original Scientific Contributions

1. Development and implementation of a custom-built lateral electric-field-assisted spin-coating setup for PEDOT:PSS (F HC Solar) thin film deposition, enabling simultaneous application of a continuous in-plane electric field and real-time electrical monitoring during film deposition, solvent evaporation, and solidification. The proposed approach demonstrated strong and reproducible directional in-plane electrical anisotropy, in which the electrical resistance measured perpendicular to the applied electric field was significantly lower than that measured parallel to the field. These findings highlight the importance of investigating anisotropy in the design and optimization of conductive polymer-based electronic devices and applications. Furthermore, the method enabled indirect observation of transient electrical evolution during film formation, providing experimental evidence of dynamic dipolar and morphological reorganization of PEDOT:PSS complexes, as well as insight into solvent evaporation, ionic mobility, and the transition from ionic to electronic transport prior to structural freezing of the polymer network.
2. The investigation of thermal transport properties in conductive polymers remains considerably less explored than electrical transport characterization, despite its critical importance for understanding thermoelectric performance and optimizing the thermoelectric figure of merit. As illustrated in Figure 1.1, the number of publications related to thermal conductivity measurements in conductive polymer thermoelectric materials is significantly smaller than those focused on electrical conductivity and Seebeck coefficient measurements. This demonstrates that heat transport mechanisms in conductive polymers remain insufficiently understood and highlights the scientific relevance and timeliness of the present work.

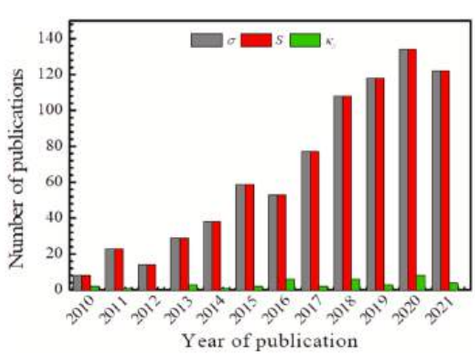

Figure 1.1. Annual number of publications related to electrical conductivity (σ), Seebeck coefficient (S), and thermal conductivity (κ) measurements in organic thermoelectric materials (2010–2021), showing the limited number of thermal transport studies in conductive polymers [30].

In this context, the present doctoral thesis contributes to the field by comprehensively investigating electrical and thermal transport phenomena in conductive PEDOT:PSS (F HC Solar) thin films. In particular, both in-plane and cross-plane thermal conductivity were experimentally determined using TR and PTR measurement setups, respectively. Furthermore, the relationship between thermal transport behavior and electrical anisotropy was systematically investigated. The originality of the present work lies not only in the characterization of electrical and thermal transport properties, but also in the demonstration of their correlation within PEDOT:PSS thin films. The obtained results showed that enhanced electrical conductivity was accompanied by enhanced in-plane thermal transport, suggesting a significant electronic contribution to heat propagation. Moreover, the experimental findings suggested the applicability of the Wiedemann–Franz framework to this particular PEDOT:PSS (F HC Solar) system, providing evidence of correlated charge and heat transport mechanisms in conductive polymer thin films. However, it should be noted that the Lorenz number in conducting polymers is not necessarily constant, and therefore, the classical Wiedemann-Franz law may not be strictly applicable.

3. Identification of tunneling-dominated charge transport as the primary conduction mechanism in highly conductive PEDOT:PSS (F HC Solar) thin films through temperature-dependent electrical conductivity measurements. The results demonstrated that charge transport in this PEDOT:PSS system occurs predominantly via tunneling rather than hopping. Furthermore, the combined analysis of electrical conductivity, thermal transport, anisotropy behavior, and nanoscale conductive pathways provided a comprehensive understanding of transport phenomena in nanostructured conductive polymers, contributing to the future design and optimization of conductive polymer-based thermoelectric devices.
4. Observation of enhanced in-plane thermal conductivity correlated with increasing electrical conductivity, indicating electronic contribution to heat propagation.
5. Investigation of substrate-induced effects on the electrical transport properties of PEDOT:PSS thin films deposited on glass, ITO-coated glass, and GaAs:Si substrates. For all investigated substrate systems, optimized ohmic electrical contacts were developed and implemented to ensure reliable and reproducible electrical transport measurements. Furthermore, PEDOT:PSS thin films deposited on ITO-coated glass substrates exhibited enhanced electrical conductivity values up to approximately 8000 S/cm, which is highly important for potential applications as transparent conductive electrodes in photovoltaic and solar-cell devices.
6. Correlation of nanoscale conductive pathways observed by C-AFM with macroscopic electrical transport behavior in PEDOT:PSS thin films. The C-AFM measurements revealed heterogeneous nanoscale conductive domains associated with PEDOT-rich regions and demonstrated that films prepared under an applied lateral electric field exhibited a higher density and improved connectivity of conductive pathways than non-field-treated or doped samples. Furthermore, correlating in-plane macroscopic conductivity measurements with cross-plane local conductivity obtained from C-AFM measurements using the equation $\sigma = (I \cdot L)/(V \cdot A)$ enabled a direct investigation of

vertical charge transport pathways and local charge distribution on the PEDOT:PSS surface. These observations correlated with the enhanced macroscopic electrical conductivity and anisotropic transport behavior measured in the films, providing direct insight into the relationship between microstructural organization and charge transport mechanisms in conductive polymers.

7. Investigation of $CuCl_2$-doped PEDOT:PSS thin films and their nanoscale charge transport behavior using C-AFM. The incorporation of metal salt particles was expected to enhance charge transport and improve electrical conductivity through increased carrier concentration and interdomain connectivity. However, the experimental results revealed a reduced density of conductive hotspots and lower local current levels compared to electric-field-treated PEDOT:PSS films, indicating that $CuCl_2$ incorporation may disrupt PEDOT domain connectivity and increase carrier scattering. These findings demonstrate the complex influence of metal-salt doping on the microstructure and transport behavior of conductive polymers.

1.7 Structure of the Thesis

The thesis consists of seven chapters organized as follows:

Chapter 2 presents the materials and sample preparation procedures used to fabricate PEDOT:PSS thin films. Different PEDOT:PSS formulations, substrates, and deposition approaches are described, including electric-field-assisted spin coating and preparation procedures for electrical and thermal characterization. Chapter 3 describes the experimental methods used to investigate the electrical and thermal transport properties of PEDOT:PSS thin films. The principles of the four-probe method, conductive atomic force microscopy, photothermal infrared radiometry, and thermoreflectance techniques are presented. Chapter 4 discusses the theoretical background of charge transport in conductive polymers. Particular attention is given to the Mott variable-range hopping model and fluctuation-induced tunneling model used for the interpretation of transport behavior in PEDOT:PSS thin films. Chapter 5 investigates the influence of substrate type, film thickness, temperature, and additive incorporation on the electrical transport properties of PEDOT:PSS thin films. Experimental conductivity measurements are analyzed with theoretical transport models to identify the dominant charge-transport mechanisms. Chapter 6 examines the thermal transport properties of PEDOT:PSS thin films using photothermal infrared radiometry and thermoreflectance techniques. Thermal conductivity, thermal anisotropy, and correlations between electrical and thermal transport are analyzed in the context of electron-assisted heat propagation. Chapter 7 investigates electrical anisotropy in PEDOT:PSS thin films fabricated under a lateral electric field during spin coating. The influence of electric-field-assisted processing on directional conductivity and the formation of conductive networks is examined using macroscopic electrical measurements and conductive atomic force microscopy. Finally, the thesis presents a summary of the main findings and perspectives on future research related to transport characterization and anisotropic conductive polymer systems.

1.8 References

[1] T. A. Skotheim and J. R. Reynolds, Handbook of Conducting Polymers, 3rd ed. Boca Raton, FL, USA: CRC Press, 2007.

[2] A. J. Heeger, "Semiconducting and metallic polymers: The fourth generation of polymeric materials," *J. Phys. Chem. B*, **105**, 8475–8491, (2001).

[3] D. Khokhar, S. Jadoun, R. Arif, and S. Jabin, "Functionalization of conducting polymers and their applications in optoelectronics," *Polym.-Plast. Technol. Mater*., **60**, 465–487, (2021).

[4] J. Ouyang, "Recent advances of intrinsically conductive polymers," *Acta Phys.-Chim. Sin*., **34**, 1211–1220, (2018).

[5] S. Chakraborty, R. Chatterjee, and A. Bandyopadhyay, "A brief review on fundamentals of conductive polymers (CPs)," *Organic Polymer Material Research*, **4**, 1-11, (2022).

[6] R. Dwivedi and R. K. Dwivedi, "A comprehensive review on conducting polymers for multifaceted applications," *J. Inorg. Organomet. Polym. Mater*., **8**, 1-102, (2025).

[7] F. Iervolino, R. Suriano, M. Cavallaro, L. Castoldi, and M. Levi, "Additively manufactured polymers for electronic components," *Appl. Sci*.,**15**, 8689, (2025).

[8] H. Letheby, "On the production of a blue substance by the electrolysis of sulphate of aniline," *J. Chem. Soc*., **15**, 161–163, (1862).

[9] H. Shirakawa, E. J. Louis, A. G. MacDiarmid, C. K. Chiang, and A. J. Heeger, "Synthesis of electrically conducting organic polymers: Halogen derivatives of polyacetylene," *J. Chem. Soc., Chem. Commun*., **16**, 578–580, (1977).

[10] A. F. Diaz, K. K. Kanazawa, and G. P. Gardini, "Electrochemical polymerization of pyrrole," J. Chem. Soc., Chem. Commun., **14**, 635–636, (1979).

[11] J. Roncali, "Conjugated poly(thiophenes): Synthesis, functionalization, and applications," *Chem. Rev.*, **92**, 711–738, (1992).

[12] L. Groenendaal, F. Jonas, D. Freitag, H. Pielartzik, and J. R. Reynolds, "Poly(3,4-ethylenedioxythiophene) and its derivatives," *Adv. Mater*., **12**, 481–494, (2000).

[13] S. Kirchmeyer and K. Reuter, "Scientific importance, properties and growing applications of PEDOT," *J. Mater. Chem*., **15**, 2077–2088, (2005).

[14] A. Elschner, S. Kirchmeyer, W. Lovenich, U. Merker, and K. Reuter, PEDOT: Principles and Applications of an Intrinsically Conductive Polymer. Boca Raton, FL, USA: CRC Press, 2010.

[15] K. Ellmer, "Past achievements and future challenges in the development of optically transparent electrodes," *Nat. Photon*., **6**, 809–817, (2012).

[16] J. Shi, M. Zhang, S. Ding, and G. Cao, "Recent progress in copper nanowire-based flexible transparent conductors," *Coatings*, **15**, 465, (2025).

[17] G. Prunet, P. Pawula, and C. O'Dwyer, "A review on conductive polymers and their hybrids for thermoelectric applications," *Synth. Met*., **277**, 116768, (2021).

[18] T. Cao et al., "Advances in conducting polymer-based thermoelectric materials and devices," *Microstructures*, **1**, 2021006, (2021).

[19] M. N. Gueye, A. Carella, J. Faure-Vincent, R. Demadrille, and J.-P. Simonato, “Progress in understanding structure and transport properties of PEDOT-based materials: A critical review,” *Prog. Mater. Sci*., **108**, 100616, (2020).

[20] S. R. Forrest, “The path to ubiquitous and low-cost organic electronic appliances on plastic,” *Nature*, **428**, 911–918, (2004).

[21] O. Bubnova and X. Crispin, “Towards polymer-based organic thermoelectric generators,” *Energy Environ. Sci*., **5**, 9345–9362, (2012).

[22] T. Someya, Z. Bao, and G. G. Malliaras, “The rise of plastic bioelectronics,” *Nature*, **540**, 379–385, (2016).

[23] U. Lang, E. Müller, N. Naujoks, and J. Dual, “Microscopical investigations of PEDOT thin films,” *Adv. Funct. Mater*., **19**, 1215–1220, (2009).

[24] X. Crispin, F. L. E. Jakobsson, A. Crispin, P. C. M. Grim, P. Andersson, A. Volodin, C. van Haesendonck, M. Van der Auweraer, W. R. Salaneck, and M. Berggren, “The origin of the high conductivity of PEDOT plastic electrodes,” *Chem. Mater*., **18**, 4354–4360, (2006).

[25] N. F. Mott, “Conduction in non-crystalline materials,” *Philos. Mag*., **19**, 835–852, (1969).

[26] P. Sheng, “Fluctuation-induced tunneling conduction in disordered materials,” *Phys. Rev. B*, **21**, 2180–2195, (1980).

[27] R. Colucci, G. C. Faria, L. F. Santos, and G. Gozzi, “On the charge transport mechanism of cross-linked PEDOT films,” *J. Mater. Sci.: Mater. Electron*., **30**, 16864–16872, (2019).

[28] Y. Lu, S. M. K. N. Islam, A. J. Ahmed, D. Liang, X. Loh, and D. J. Young, “Solving the interdependence between electrical conductivity and Seebeck coefficient: A case study of PEDOT,” *Chem. Asian J*., **20**, Art. no. e202401854, (2025).

[29] L. Liu, L. Liang, L. Deng, H. Wang, and G. Chen, “Is there a constant Lorentz number for organic thermoelectric materials?” *Appl. Mater. Today*, **27**, 101496, (2022).

[30] F. Fan, W. Nie, H. Tsai, N. Wang, H. Huang, Y. Cheng, R. Wen, L. Ma, F. Yan, and Y. Xia, “PEDOT for flexible and stretchable electronics: Modifications, strategies, and applications,” *Adv. Sci*., **6**, 1900813, (2019).

Chapter 2

Materials and Sample Preparation

2.1 Introduction

This chapter presents the materials and preparation procedures used for the fabrication of PEDOT:PSS thin films investigated in this work. Different PEDOT:PSS formulations, including F HC Solar, higher-solid-content dispersions, and $CuCl_2$-modified solutions, were used to study the effects of processing conditions and composition on film properties. Thin films were deposited by spin coating on various substrates, with thickness controlled using a layer-by-layer (LbL) approach. Additional processing strategies, including electric-field-assisted deposition, were introduced to tailor the film structure and electrical behaviour. The preparation of samples for electrical and thermal characterization is also described, including contact fabrication, chip carrier mounting, and the integration of metallic transducer layers. These procedures provide the experimental basis for the investigations presented in the following chapters.

2.2 Materials

Several PEDOT:PSS formulations were employed in this study to investigate the influence of processing conditions, additives, and film thickness on the electrical and morphological properties of conductive polymer thin films.

A commercially available PEDOT:PSS formulation (F HC Solar, M126-100ml, Ossila Ltd.) was used as the primary conductive polymer. This material is an aqueous dispersion of PEDOT:PSS, specifically developed for applications in organic photovoltaics, printed electronics, and sensor technologies. The formulation is characterized by a solid content in the range of 1.0-1.5 wt.% and exhibits a high electrical conductivity exceeding 500 S cm^{-1} after film formation. The work function is reported to be between 4.8 and 5.0 eV, making it suitable for use as a charge transport layer in optoelectronic devices. Additionally, the dispersion exhibits low contact angles on common substrates such as ITO, facilitating uniform thin-film deposition. The PEDOT:PSS (F HC Solar) dispersion was used as received without further purification and stored at 3-5 °C according to the manufacturer's recommendations. Table 2.1 summarizes the technical data for F HC Solar PEDOT:PSS.

In addition to the F HC Solar formulation, a PEDOT:PSS aqueous dispersion with a higher solids content (3-4 wt.%) was used to prepare thin films on glass substrates. This formulation was primarily used to investigate the influence of polymer concentration on film morphology and electrical behaviour. Furthermore, PEDOT:PSS (3-4 wt.%) solutions modified with copper (II) chloride ($CuCl_2xH_2O$) were prepared to study the effect of metal salt additives on the electrical conductivity and microstructure of the thin films. The $CuCl_2$ additive was introduced into the PEDOT:PSS dispersion prior to deposition and thoroughly mixed to ensure homogeneous distribution. Thin films were deposited on different substrate types, including glass, ITO-coated glass, and GaAs:Si.

Table 2.1. F HC Solar PEDOT:PSS technical data.

Solvent	Composition	Solid content	Work function	Resistivity	Conductivity	Particle size distribution	Viscosity	PH value
Water	PEDOT:PSS	1.0 – 1.5 wt.%	4.8 – 5.0 eV	< 0.002 Ω.cm	>500 S/cm	N/A	8 – 70 mPa.s	1.0 -2.0

2.3 PEDOT:PSS Thin Film Deposition

2.3.1 PEDOT:PSS (F HC Solar) Thin Film Preparation

The preparation of high-quality thin films is a critical step in achieving reliable and reproducible device performance, particularly in organic electronic and optoelectronic applications. In this work, PEDOT:PSS (F HC Solar) thin films were deposited onto various substrates using a spin-coating technique to ensure uniformity, cleanliness, and controlled film morphology. Thin films were prepared on glass, ITO-coated glass, and GaAs:Si substrates (5×5 mm^2 and 10×10 mm^2). Prior to coating, the substrates underwent a two-step solvent cleaning procedure using a spin coater to remove organic and particulate contaminants. First, each glass substrate was rinsed with acetone while spinning at 3500 rpm for 30 s. This was immediately followed by a second rinse using isopropanol under the same spinning conditions (3500 rpm, 30 s). This sequential solvent treatment effectively removed residual impurities and improved surface wettability. After the solvent-rinsing steps, substrates were dried under a stream of compressed air to ensure a clean, residue-free surface prior to film deposition. A defined volume of the PEDOT:PSS dispersion was deposited onto the substrate surface and spin-coated at a rotational speed of 3500 rpm for 30 s. After deposition, the films were annealed on a hot plate at 110 °C for 15 min to remove residual solvent and improve film adhesion.

To achieve precise control over the film thickness, a LbL deposition approach was employed. In this method, multiple spin-coating cycles were performed sequentially under identical conditions. After each deposition step, the films were thermally treated at 110 °C for 15 min before applying the subsequent layer. The thickness of the PEDOT:PSS films was estimated based on the thickness–spin-speed relationship provided by the manufacturer (Ossila). At a spin speed of 3500 rpm, a single deposited layer corresponds to an approximate thickness of 80 nm. By repeating the deposition process, thicker films were obtained in a controlled manner. For instance, two deposition cycles resulted in films approximately 160 nm thick, while six sequential layers yielded films up to approximately 480 nm thick. The thickness dependence on spin speed for the PEDOT:PSS (F HC Solar) formulation is illustrated in Figure 2.1, which was used as a reference for thickness estimation and process optimization.

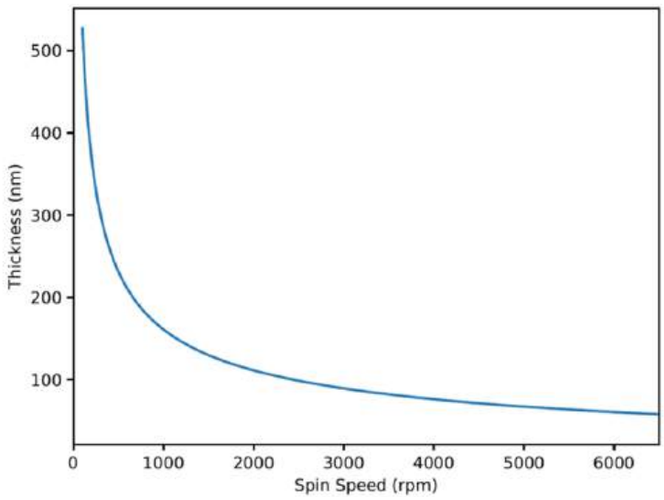

Figure 2.1. The thickness dependence on spin speed for the PEDOT:PSS (F HC Solar) formulation provided by the seller (Ossila).

2.3.2 PEDOT:PSS (3-4 wt.%) and PEDOT:PSS + $CuCl_2$ Thin Film Preparation

PEDOT:PSS thin films based on a higher solid content dispersion (3-4 wt.%) and $CuCl_2$-modified PEDOT:PSS were prepared on glass substrates (15×15 mm^2) using a spin-coating technique (Spin Coater Laurell 650SZ). The preparation procedure is based on our previously reported work [1]. Prior to deposition, the substrates were cleaned in an ultrasonic bath in acetone, ethanol, and deionized water for 5 min each, then dried under ambient conditions. The PEDOT:PSS (3-4 wt.%) dispersion was filtered through a 0.45 μm syringe filter to remove impurities and ensure uniform film formation. A volume of 200 μl of the solution was then deposited onto the glass substrate and spin-coated at 4000 rpm for 60 s, resulting in thin films with an approximate thickness of 500 nm. For the preparation of $CuCl_2$-modified PEDOT:PSS films, copper (II) chloride ($CuCl_2xH_2O$) was added to the PEDOT:PSS dispersion at a concentration of 2 mg per 1.17 mL of solution. The mixture was ultrasonicated for 5 min to ensure homogeneous distribution and subsequently filtered prior to deposition. The solution was then spin-coated under identical conditions. After deposition, all samples were annealed on a hot plate at 110 °C for 15 min. For electrical characterization, the samples were cleaved into smaller pieces (typically 5 × 5 mm^2) for temperature-dependent electrical measurements prior to mounting in the measurement setup (Van der Pauw).

2.3.3 Surface, Thickness, and Structural Characterization of PEDOT:PSS Thin Films

The surface quality and morphology of the deposited PEDOT:PSS thin films were first investigated using optical microscopy. Representative optical microscope images of PEDOT:PSS thin films deposited on different substrates are shown in Figure 2.2. Figure 2.2 (a) presents a 10 × 10 mm^2 sample deposited on a glass substrate, Figure 2.2 (b) shows a 5 × 5 mm^2 sample prepared on glass, and Figure 2.2 (c) illustrates a PEDOT:PSS thin film deposited on a GaAs:Si substrate. As observed in the optical micrographs, all samples exhibit smooth, homogeneous surfaces without visible cracks, pinholes, agglomerates, or large-scale inhomogeneities. These images represent representative PEDOT:PSS films investigated throughout this work and confirm the reproducibility and uniformity of the employment procedures.

e

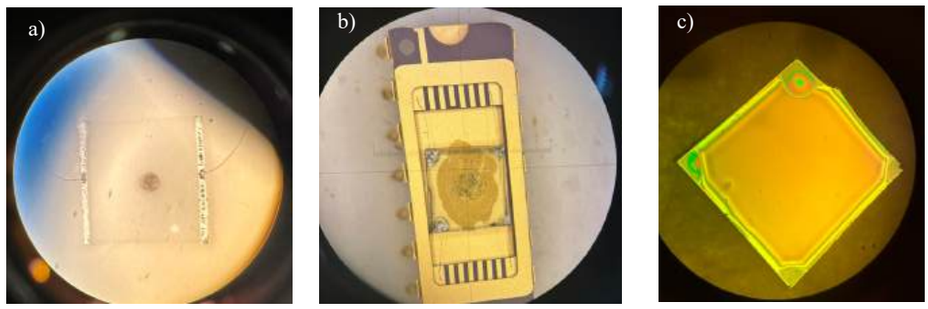

Figure 2.2. Optical microscope images of representative PEDOT:PSS thin films deposited on different substrates and with different lateral dimensions: (a) 10 × 10 mm^2 sample on a glass substrate, (b) 5 × 5 mm^2 sample on a glass substrate, and (c) 10 × 10 mm^2 sample on a GaAs:Si substrate. All samples exhibit smooth and homogeneous surfaces.

To validate the thickness values estimated from the Ossila thickness-spin-speed relationship, cross-sectional thickness measurements were performed using atomic force microscopy (AFM). The thickness values were initially estimated using the thickness-spin-speed relationship provided by the manufacturer (Ossila), shown in Figure 2.1. According to the manufacturer's data, a spin speed of 3500 rpm corresponds to an approximate single-layer film thickness of 80 nm. Thicker films were subsequently prepared using the LbL deposition approach by repeating the spin-coating and annealing cycles. Representative AFM topography images and corresponding step-height profiles for PEDOT:PSS thin films with different nominal thicknesses are presented in Figure 2.3. Figure 2.3 (a) shows the AFM measurement for a PEDOT:PSS thin film prepared at a spin speed of 3500 rpm, for which the expected thickness based on the Ossila datasheet was approximately 80 nm. The AFM step-profile analysis revealed a measured thickness of approximately 90 nm, demonstrating good agreement with the estimated value. Figure 2.3 (b) presents the AFM topography and thickness profile for a multilayer PEDOT:PSS film with a nominal thickness of approximately 480 nm obtained using the LbL deposition method. The AFM analysis indicated a thickness of approximately 400 nm. Although slight deviations between the estimated and measured thickness values were observed, the AFM results confirm the successful deposition of thicker multilayer PEDOT:PSS films and validate the overall thickness trend predicted by the Ossila thickness-spin-speed relationship. The deviations between the estimated and experimentally measured thicknesses are attributed to factors such as local surface inhomogeneities, uncertainties associated with the AFM step-profile method, scratching conditions during sample preparation, and thickness variations introduced during multilayer deposition. Nevertheless, the measured thicknesses remained within a reasonable agreement with the expected values. A comparison between the thickness values estimated from the Ossila thickness-spin-speed relationship and the experimentally measured AFM thicknesses is presented in Figure 2.4. The results demonstrate a consistent correlation between the expected and measured thicknesses, confirming that the manufacturer-provided thickness relationship can be reliably used to estimate the thickness of PEDOT:PSS thin films prepared in this work.

a)

b)

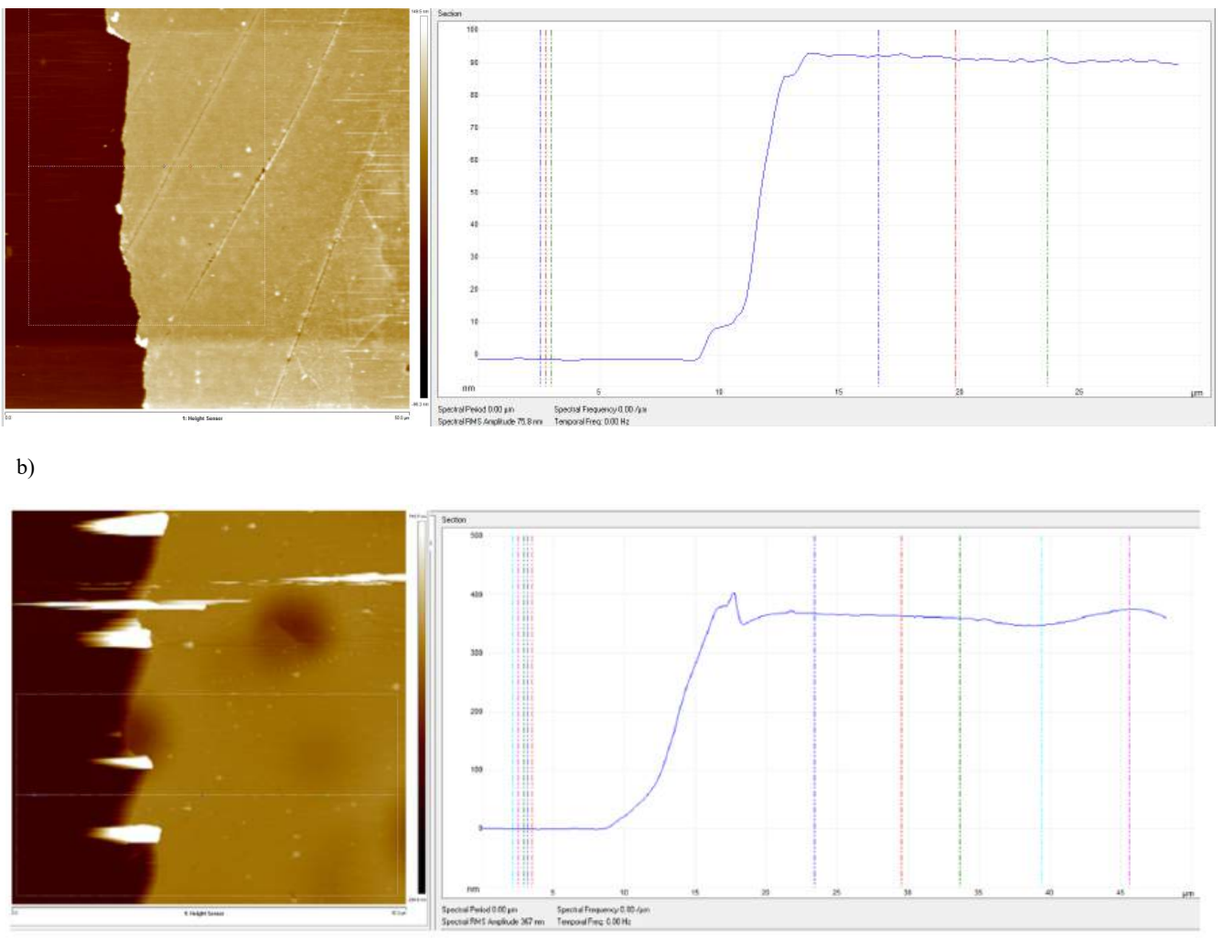

Figure 2.3. AFM topography images and corresponding cross-sectional thickness profiles of PEDOT:PSS thin films prepared using spin coating and the LbL deposition approach: (a) PEDOT:PSS thin film with a nominal thickness of approximately 80 nm deposited at 3500 rpm and (b) multilayer PEDOT:PSS thin film with a nominal thickness of approximately 480 nm. The AFM measurements confirm the successful deposition of homogeneous PEDOT:PSS films and demonstrate reasonable agreement with the thickness values estimated from the Ossila thickness-spin-speed relationship.

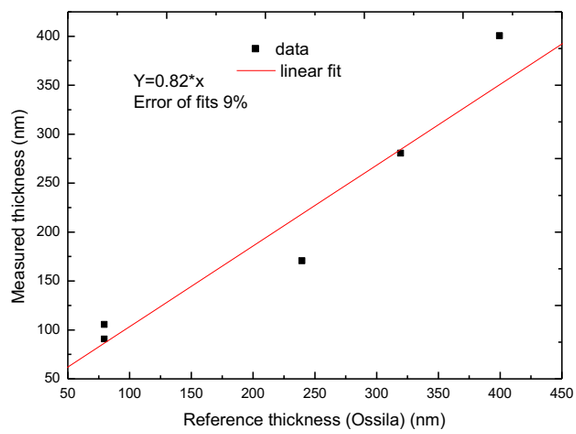

Figure 2.4. Comparison between the PEDOT:PSS thin film thicknesses estimated from the Ossila thickness-spin-speed relationship, and the experimentally measured thicknesses obtained from AFM cross-sectional analysis. The results demonstrate reasonable agreement between the expected and measured thickness values, confirming the reliability of the employed deposition procedure and thickness estimation method.

Moreover, X-ray diffraction (XRD) measurements were performed using a PANalytical X'Pert Pro MRD diffractometer equipped with a hybrid two-bounce Ge (220) monochromator and a triple-axis Ge (220) analyzer positioned in front of the detector. The instrument was fitted with a Cu-anode X-ray source that generated CuKα_1 radiation with a wavelength of λ = 1.54056 Å. to investigate the structural properties and molecular ordering of the PEDOT:PSS thin films. XRD

analysis is commonly used for PEDOT:PSS materials to assess the degree of crystallinity and structural ordering, which can influence the electrical conductivity and charge-transport properties of the films. Figure 2.5 shows the XRD pattern of a PEDOT:PSS thin film with a nominal thickness of approximately 480 nm deposited on a GaAs:Si substrate. A diffraction feature is observed near $2\theta \approx 25°$, which is commonly associated with π–π stacking and structural ordering within the PEDOT-rich domains and agrees with the values reported in literature [2]. The presence of this peak indicates the formation of an ordered PEDOT:PSS structure and is correlated with enhanced electrical conductivity of the film. The diffraction peak observed near $2\theta \approx 60°$is attributed to the GaAs:Si substrate. An additional peak near $2\theta \approx 90°$was also detected; however, its origin could not be clearly identified and therefore was not further assigned in this work.

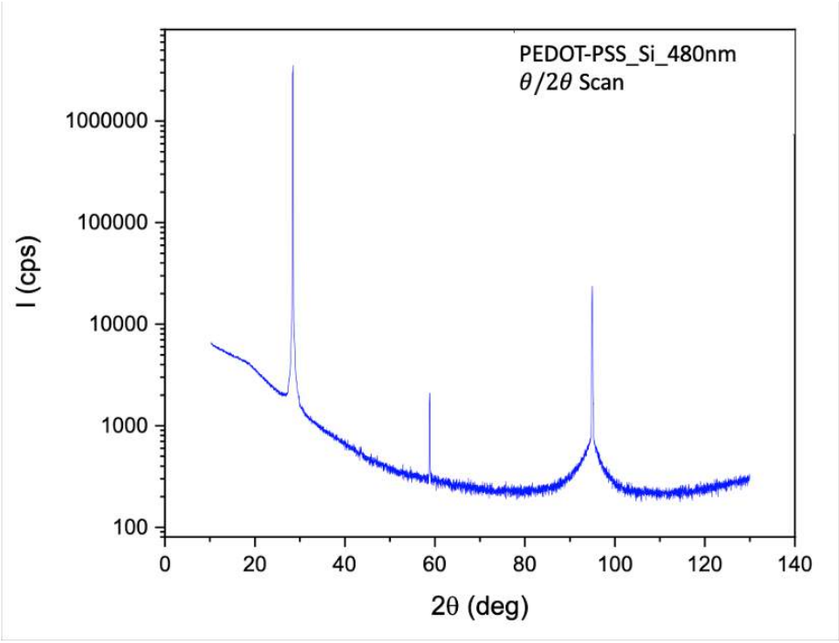

Figure 2.5. XRD pattern of the PEDOT:PSS thin film (~480 nm) deposited on a GaAs:Si substrate. The diffraction peak near $2\theta \approx 25°$ indicates structural ordering within the PEDOT:PSS film, while the peak around $2\theta \approx 60°$ originates from the GaAs:Si substrate.

In addition to AFM and XRD characterization, scanning electron microscopy (SEM, Model: Hitachi SU-70) was performed to investigate the cross-sectional morphology of the PEDOT:PSS thin film deposited on a glass substrate. The cross-sectional SEM image of the PEDOT:PSS film with a nominal thickness of approximately 480 nm is shown in Figure 2.6. The image shows the formation of a continuous, uniform PEDOT:PSS layer on the glass substrate. The bright contrast line observed at the surface corresponds to the PEDOT:PSS thin film, indicating smooth film deposition and good interface uniformity between the polymer layer and the substrate. The SEM analysis further confirms the successful fabrication of homogeneous PEDOT:PSS thin films using the spin-coating and LbL deposition procedures employed.

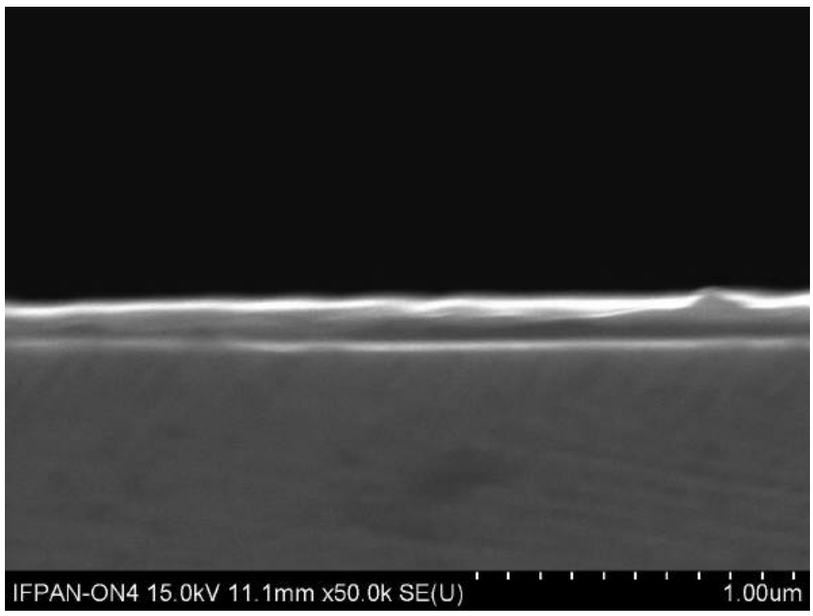

Figure 2.6. Cross-sectional SEM image of the PEDOT:PSS thin film (~480 nm) deposited on a glass substrate. The bright contrast layer at the surface corresponds to the PEDOT:PSS thin film, demonstrating smooth and uniform film deposition on the substrate.

2.4 Sample Preparation for Electrical Conductivity Measurements

For electrical characterization, the prepared PEDOT:PSS thin films were mounted on chip carriers in different configurations, depending on sample size and measurement conditions. Two types of chip carriers were employed to accommodate both room temperature and temperature-dependent electrical measurements.

2.4.1 Preparation for Large-Area Samples

For PEDOT:PSS thin films with dimensions of 10 × 10 mm^2 and 15 × 15 mm^2 were mounted onto a chip carrier designed for planar electrical characterization. Ohmic contacts were established at the four edges of the samples using silver paste (Acheson 1415, silver flakes in methyl isobutyl ketone, No. G3692, 50 g). Fine Cu-wires (Tin coated) wires were then used to connect the contact points to the chip carrier terminals. The samples were mechanically fixed to the chip carrier with an adhesive (Fixogum), and the electrical connections were reinforced by soldering the wires with Sn solder at 350 °C using a soldering station (Weller WECP-20). The sample mounted on the chip carrier is shown in Figure 2.7 (a). The prepared samples were subsequently used for electrical measurements in a Hall setup operating in the van der Pauw configuration (Figure 2.7 (b)). In this method, current is applied through the sample, while the corresponding voltage drops are measured across different contact pairs, thereby enabling determination of the sheet resistance. A detailed description of the measurement setup is provided in Chapter 3.

2.4.2 Preparation for Small-Area Samples

For temperature-dependent electrical measurements, smaller samples with dimensions of approximately 4 × 4 mm^2 and 5 × 5 mm^2 were used. Prior to thin film deposition, the substrates were cleaved to the desired size using a diamond scriber (Karl Suss HR-100). After deposition, the samples were mounted onto a dedicated chip carrier compatible with a closed-cycle cryostat system. Electrical connections were established using Al wire bonding, performed with a manual

wire-bonding machine equipped with a microscope and control electronics (MDB/ISG TC), as shown in Figure 2.7(c). To improve the electrical contact quality, silver paste was additionally applied to the edges of the samples to ensure stable, low-resistance ohmic contacts. The fully prepared and mounted sample is shown in Figure 2.7 (d). The samples were subsequently placed inside a closed-cycle cryostat for temperature-dependent electrical measurements. Further details regarding the cryostat system and measurement procedure are provided in Chapter 3.

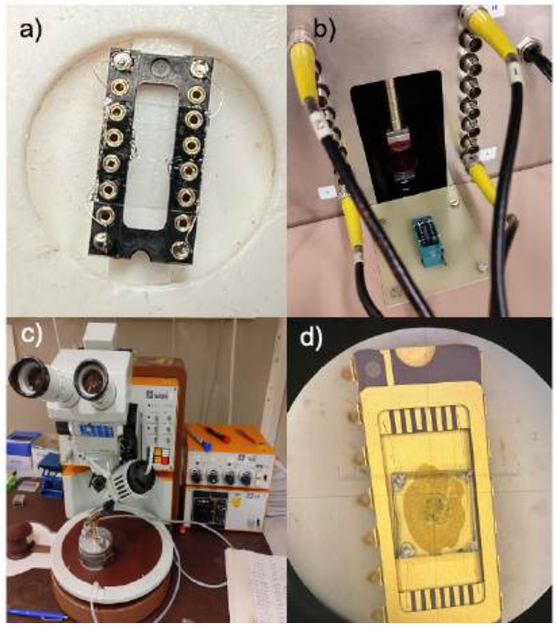

Figure 2.7. Preparation of PEDOT:PSS thin film samples for electrical measurements. (a) Large-area sample (10 × 10 mm^2/ 15 × 15 mm^2) mounted on a chip carrier with silver paste contacts and wired connections. (b) Hall-measurement setup operating in the van der Pauw configuration for room-temperature electrical characterization. (c) wire bonding process used to establish electrical connections for small-area samples. (d) Small-area sample (4 × 4 mm^2 / 5 × 5 mm^2) mounted on a chip carrier with wire-bonded contacts, ready for temperature-dependent measurements in a closed-cycle cryostat.

2.5 Electric-Field-Assisted Thin Film Deposition

In addition to conventional spin coating, PEDOT:PSS thin films were also prepared under the influence of an applied lateral electric field during deposition. This approach was used to investigate the effect of electric-field-induced alignment on the films' structural and electrical properties. The deposition was performed using a modified spin-coating setup, in which parallel indium (In) electrical contacts were formed on opposite sides of the substrate to apply a constant DC voltage during film formation. The electric field was applied throughout the spin-coating process, allowing real-time monitoring of the current response during solvent evaporation and film solidification. A detailed description of the experimental setup, including the electrode configuration, electrical connections, and data acquisition system, is provided in Chapter 7.

2.6 Preparation of Samples for Thermal Conductivity Measurements

For thermal characterization using TR and PTR methods, PEDOT:PSS (F HC Solar) thin films were deposited on glass substrates with lateral dimensions of 10 × 10 mm^2. Films with different thicknesses of approximately 240 nm, 320 nm, and 480 nm were prepared using the LbL spin-coating approach described in section 2.3.1. To enable optical thermal measurements, metallic transducer layers were deposited on top of the PEDOT:PSS films. Thin metal layers of aluminium (Al), titanium (Ti), and gold (Au) were deposited onto the films using a vacuum evaporation

system. First, a 50 nm thick Al layer was deposited uniformly over the entire film surface, serving as a thermal transducer by absorbing incident laser energy and converting it into a measurable thermal response. Subsequently, a bilayer consisting of Ti (20 nm) and Au (20 nm) was deposited on half of the sample surface. The Ti layer acts as an adhesion layer between the PEDOT:PSS and Au, while the Au layer provides high optical reflectivity required for sensitive detection in reflectance-based measurement techniques. The use of metallic transducer layers is essential for TR and PTR methods, as PEDOT:PSS exhibits relatively low optical reflectivity and limited absorption efficiency. The metal layers enhance the optical signal, improve heat generation, and provide a well-defined interface for thermal transport analysis. A schematic representation of the resulting multilayer structure is shown in Figure 2.8.

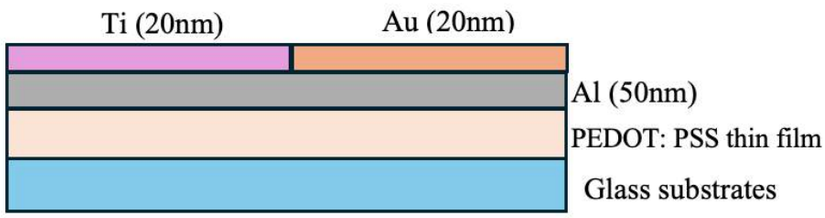

Figure 2.8. Schematic representation of the multilayer structure used for thermal measurements, consisting of a glass substrate, PEDOT:PSS (F HC Solar) thin film, aluminium (50 nm) transducer layer, and a partially deposited Ti (20 nm) / Au (20 nm) bilayer.

2.7 Conclusion

In this chapter, the materials and preparation methods for PEDOT:PSS thin films were described. Different formulations and processing approaches were employed to control film thickness, composition, and structure. Spin coating, LbL deposition, and electric-field-assisted techniques were used to fabricate the films, while appropriate sample preparation methods were developed for electrical and thermal measurements. The described procedures ensure reproducible sample fabrication and form the basis for the analysis of the electrical and thermal properties presented in the subsequent chapters.

2.8 References

[1] A. Mikaeeli, N. Jukam, R. Szczesny, A. Ludwig, I. Bolukbasi, A. D. Wieck, and M. Pawlak, “Electrical characterization of Cu-doped PEDOT:PSS polymeric thin films,” *Eng. Proc*., **56**, 327, (2024).

[2] S.-P. Rwei, Y.-H. Lee, J.-W. Shiu, R. Sasikumar, and U.-T. Shyr, “Characterization of solvent-treated PEDOT:PSS thin films with enhanced conductivities,” *Polymers*, **11**, 134, (2019).

Chapter 3

Measurement Methods

(Electrical and Thermal Techniques)

3.1. Introduction

This chapter describes the experimental techniques used to characterize the electrical and thermal transport properties of PEDOT:PSS thin films. Understanding both charge and heat transport is essential for evaluating the performance of these materials in optoelectronic and thermoelectric applications. To obtain a comprehensive assessment across different length scales and transport directions, both macroscopic and nanoscale measurement methods were utilized. In-plane electrical conductivity was measured using the four-probe technique, while cross-plane charge transport was investigated by C-AFM. Thermal transport properties were evaluated using non-contact optical methods, namely PTR and TR. The working principles, experimental configurations, and data analysis procedures for each technique are detailed in the following sections

3.2 Electrical Measurement Methods

Electrical characterization of PEDOT:PSS thin films was carried out to evaluate charge transport behavior across multiple length scales and transport directions. Both macroscopic and nanoscale measurement techniques were employed to determine in-plane and cross-plane electrical conductivity. The fundamental concepts governing electrical conductivity and the measurement approaches adopted in this work are described in the following sections.

3.2.1 Fundamentals of Electrical Conductivity

Electrical conductivity is a fundamental material property that quantifies a material's ability to conduct electric current. It reflects the ease with which charge carriers move through a material under an applied electric field and is a key parameter for evaluating electronic transport behavior in functional thin films. Electrical conductivity (σ) is defined as the inverse of electrical resistivity (ρ) [1]:

$$\sigma = \frac{1}{\rho} \qquad (3.1)$$

While conductivity describes how readily electric current flows, resistivity represents the intrinsic opposition of a material to charge transport. Both parameters are independent of sample geometry and depend solely on the material's electronic structure and scattering mechanisms [1]. In homogeneous and isotropic materials, electrical conduction follows Ohm's law in differential form [1,2]:

$$\vec{j} = \sigma \vec{E} \qquad (3.2)$$

where $\vec{j}$ is the current density ($A \cdot m^{-2}$) and $\vec{E}$ is the applied electric field ($V \cdot m^{-1}$). Materials that exhibit a linear relationship between current density and electric field are classified as Ohmic

conductors. In semiconducting and polymeric systems such as PEDOT:PSS, electrical conductivity depends not only on the presence of charge carriers but also on their mobility. The total conductivity can be expressed as [2,3]:

$$\sigma = q(n\mu_n + p\mu_p) \qquad (3.3)$$

where q is the elementary charge (1.602×10^{-19} C), n and p are the electron and hole concentrations, and μ_n and μ_p are their respective mobilities. This formulation highlights that conductivity is governed by both carrier density and transport efficiency, which are influenced by doping, temperature, and structural disorder [3]. At the microscopic level, conductivity can be further described within the Drude-Sommerfeld framework as: [2]

$$\sigma = \frac{nq^2\tau}{m^*} \qquad (3.4)$$

where τ represents the carrier relaxation time and m* is the effective mass. This relation emphasizes the role of carrier scattering, defects, and lattice interactions in determining electrical transport properties. For thin films, electrical transport is commonly characterized by sheet resistance (R□), which quantifies lateral conduction independent of sample dimensions. The electrical resistance of a thin film can be expressed as:

$$R = R_{\square}\frac{L}{W} \qquad (3.5)$$

Where R is the measured resistance, L is the length of the conductive path, and W is the width of the film. The ratio $\frac{L}{W}$ represents the number of "squares" in the geometry, while $R_{\square}$ denotes the sheet resistance of the material [4].

If the thin film thickness t is known, the bulk resistivity ρ (in $\Omega.m$) can be determined from:

$$\rho = R_{\square}.t \qquad (3.6)$$

where t is the film thickness. Accordingly, electrical conductivity σ can be determined from:

$$\sigma = \frac{1}{\rho} = \frac{1}{R_{\square}\cdot t} \qquad (3.7)$$

Because sheet resistance is independent of the sample's lateral size, it provides a practical and reliable parameter for comparing the electrical performance of thin conductive films, particularly in polymer coatings and transparent electrodes [4]. To experimentally determine the in-plane electrical conductivity of the fabricated PEDOT:PSS thin films, sheet resistance measurements were performed using a four-probe method based on the Van der Pauw configuration, as described in the following section.

3.2.2 Van der Pauw (4-Probe) Method

The Van der Pauw method [5] is one of the most widely utilized techniques for evaluating the electrical properties of thin conducting materials, including resistivity and sheet resistance. Originally developed in 1958 by Leo J. van der Pauw, this method enables the determination of sheet resistance independently of the sample's lateral geometry. Owing to this geometry-independent nature, the technique is particularly well suited for thin films of arbitrary shape. Accurate application of the Van der Pauw formalism requires several fundamental conditions to be satisfied. The conducting layer must possess uniform thickness, the material should be laterally homogeneous, and the sample must constitute a simply connected domain without isolated voids. In addition, four ohmic point contacts are positioned on the sample's four edges, with dimensions sufficiently small relative to the overall sample size so as not to perturb the current distribution. Under these conditions, the measured electrical response reflects the intrinsic transport properties of the film rather than geometrical artifacts. A key requirement of the Van der Pauw approach is that electrical characterization is performed using multiple current-injection and voltage-sensing permutations. In a typical configuration, a direct current $I_{1,2}$ is applied between contacts 1 and 2, while the resulting voltage drop $U_{4,3}$ is measured across the opposite contacts 4 and 3. The contacts are then cyclically permuted such that current $I_{2,3}$ flows between contacts 2 and 3 and the voltage $U_{1,4}$ is measured across contacts 1 and 4 [6].

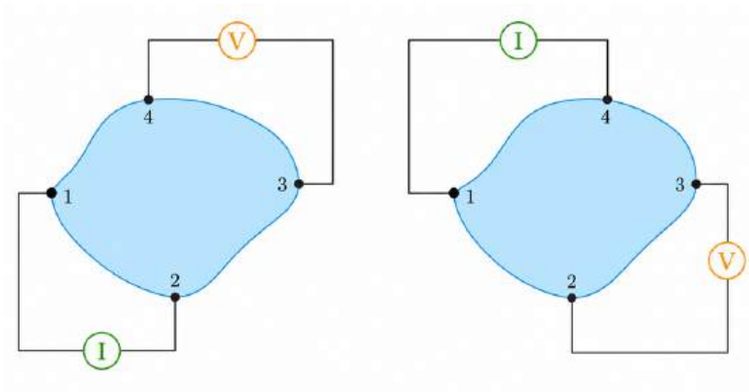

Figure 3.1. Measurements of the sheet resistance of an arbitrary, simply connected surface [Regenerated from Ref 6].

The requirement is a simply connected area with four point-like contacts placed at the edge of the sample, as shown in Figure 3.1. Two resistance values are needed:
First, a current $I_{1,2}$ is applied to contacts 1 and 2, and the voltage drop $U_{4,3}$ is measured across the opposite contacts 3 and 4. Then the contacts are cyclically permuted, current is applied to contacts 2 and 3 ($I_{2,3}$), and the voltage $U_{1,4}$ is measured. Van der Pauw was able to show that the two resistance values [6],

$$R_{1,2;4,3} = \frac{U_{4,3}}{I_{1,2}} \quad and \; R_{2,3;1,4} = \frac{U_{1,4}}{I_{2,3}} \qquad (3.8)$$

are linked to the sheet resistance through the following expression, regardless of the shape of the sample:

$$exp\left(-\pi \frac{R_{1,2;4,3}}{R_{\square}}\right) + exp\left(-\pi \frac{R_{2,3;1,4}}{R_{\square}}\right) = 1 \qquad (3.9)$$

Equation (3.9) can only be analytically solved for $R_{\square}$ if the sample has a highly symmetrical shape, such as circular or square. In that case, the two resistance values satisfy $R_{1,2;4,3} \approx R_{2,3;1,4}$, and the sheet resistance can be calculated using:

$$R_{\square}^{sym} = \frac{\frac{\pi}{ln2}\left(R_{1,2;4,3} + R_{2,3;1,4}\right)}{2} \qquad (3.10)$$

Otherwise, Equation (3.8) must be solved numerically, for example using a Newton-Raphson method. As a measure of the symmetry of a sample, the geometry factor is defined as $f = \frac{R_{\square}^{sym}}{R_{\square}}$. It equals 1 for a perfectly symmetrical sample (i.e., when $R_{\square} = R_{\square}^{sym}$), and becomes smaller as the width-to-length ratio of the sample increases. According to Van der Pauw, the resistances should yield the same values after two full cycles of contact permutation $R_{1,2;4,3} = R_{3,4;2,1}$ and $R_{2,3;1,4} = R_{4,1;3,2}$. To improve measurement accuracy, both values are measured in both current directions, and the average values R_A and R_B are taken. Deviations from these averages suggest inhomogeneities in the sample, and the measurement software issues an error if the deviation exceeds 5%. An error is also shown if the resistances differ by more than 10% when the current direction is reversed, indicating non-ideal ohmic contacts. Standard sample geometries for Van der Pauw measurements are highly symmetrical to increase measurement accuracy. Common types include rectangular samples with contacts on the corners, or cloverleaf-shaped structures. The geometry used in this study corresponds to the one shatn Figure 3.2 (b). Fiure 3.3 provides an overview of the Van der Pauw measurement procedure [6].

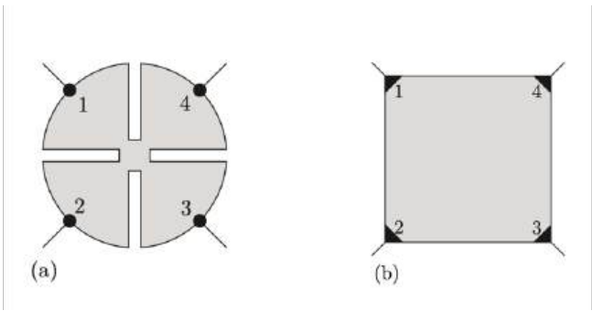

Figure 3.2. Common Van dr Pauw geometries: (a) clooverleaf and (b) square contact of configuration [6].

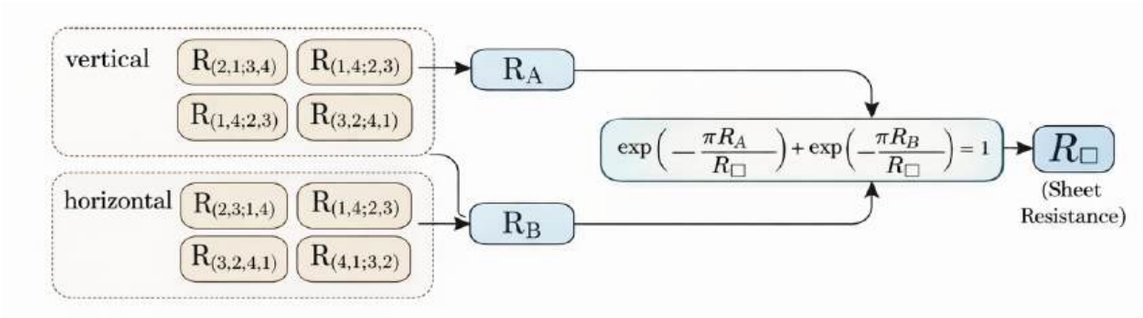

Figure 3.3. Procedure for a Van der Pauw measurement.

3.2.3 Temperature-Dependent Electrical Conductivity (Closed-Cycle Cryostat)

To investigate the charge transport mechanisms in PEDOT:PSS thin films, temperature-dependent electrical conductivity measurements were performed using the four-probe Van der Pauw configuration integrated within a closed-cycle cryostat system. This approach enabled

systematic evaluation of the in-plane electrical transport properties over a broad temperature range. The measurements were carried out using a computer-controlled DC Hall measurement system operating in four-probe mode. A switching matrix enabled automated permutation of current and voltage contacts without manual rewiring, thereby minimizing contact-handling errors and improving measurement reproducibility. The measurement current was supplied by either a Keithley 220 DC current source or a Keithley 236 Source Measure Unit (SMU), depending on the sample resistance range. Voltage signals were recorded using a Keithley 2700 digital multimeter equipped with a switching matrix. With a 6½-digit resolution and voltage sensitivity down to 100 nV, the system enabled precise detection of small voltage drops, which is particularly critical for low-conductivity polymer films. The high input impedance (>10 GΩ) ensured negligible loading effects for highly resistive samples. To enhance measurement accuracy, automated averaging over multiple cycles was performed, and the analog-to-digital converter was synchronized with the mains frequency to suppress common-mode noise. For temperature-dependent measurements, the samples were mounted in a closed-cycle pulse-tube cryostat (Bruker system), enabling controlled temperature variation from approximately 1.5 K to 300 K. The cryostat eliminates the need for liquid helium handling while providing stable, continuous temperature control. Temperature monitoring was performed using calibrated sensors positioned in close thermal contact with the sample holder. At each temperature step, sheet resistance was determined using the Van der Pauw method as described in Section 3.2.2. The corresponding resistivity was calculated from the measured sheet resistance and film thickness, and the temperature-dependent electrical conductivity was subsequently obtained via [6]:

$$\rho(T) = R_{\square}(\mathrm{T}) \cdot \mathrm{t}, \text{ and } \sigma(T) = \frac{1}{\rho(T)} \quad (3.11)$$

This procedure enabled systematic analysis of thermally activated transport processes and conduction mechanisms within the PEDOT:PSS thin films. A simplified circuit diagram of the setup is shown in Figure 3.4.

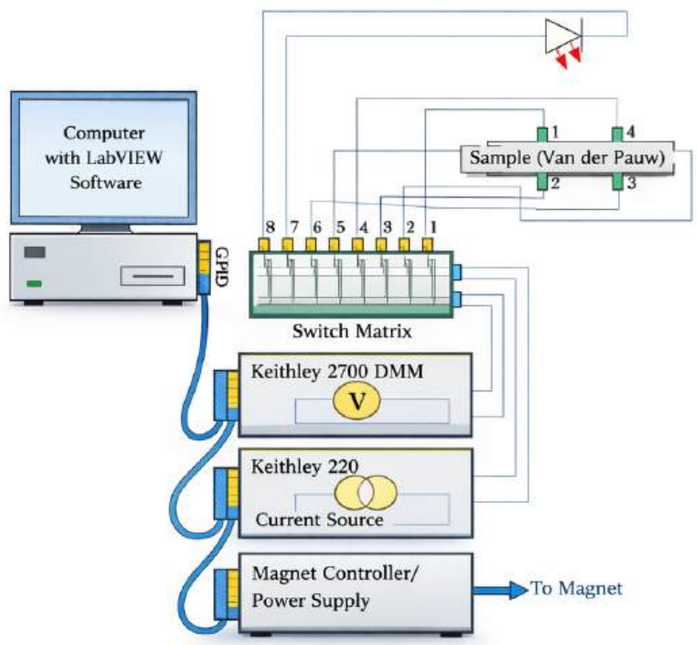

Figure 3.4. A simplified circuit diagram of the DC Hall setup.

3.2.4 Conductive Atomic Force Microscopy (C-AFM)

To investigate nanoscale charge transport pathways and cross-plane electrical conductivity, C-AFM measurements were performed using a Park Systems NX20 atomic force microscope. This technique enables the simultaneous acquisition of surface topography and local current distribution with nanometer-scale spatial resolution, thereby providing direct insight into vertical charge transport across the film thickness. In contrast to macroscopic four-probe measurements, which evaluate in-plane conductivity, C-AFM probes localized cross-plane conduction. During operation, a conductive probe is scanned in continuous contact with the sample surface while a bias voltage is applied between the tip and the grounded substrate. The resulting current flowing through the tip-sample junction is recorded at each pixel, producing spatially resolved current maps that reflect local conductivity variations across the scanned region. As illustrated in Figure 3.5, a bias voltage is applied between the conductive tip and the sample, while the bottom electrode (metal sample disk) is grounded or biased via the sample holder. When the tip is in contact with the surface, current flows vertically through the film, enabling mapping of cross-plane charge transport with nanometer resolution [7].

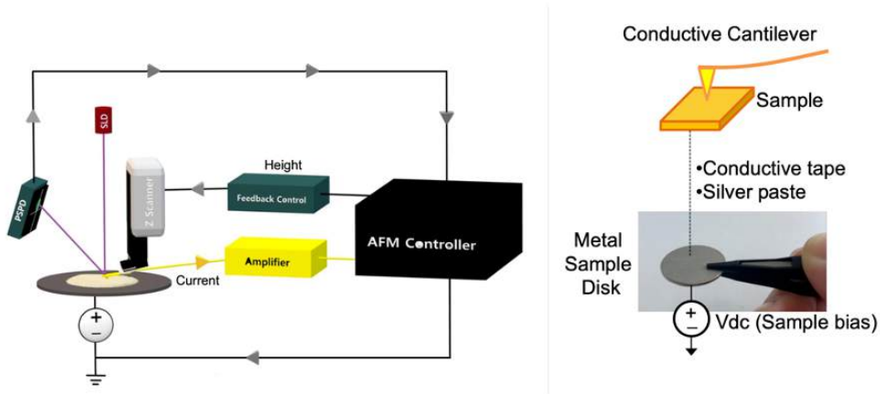

Figure 3.5. Schematic representation of C-AFM includes: a conductive cantilever tip a bias voltage source, a current preamplifier connected to the tip, a feedback loop to control tip-sample interaction force [7].

The cross-plane electrical conductivity can be estimated from the measured current data using [8]:

$$\sigma = \frac{IL}{VA} \qquad (3.12)$$

Where, I is the total measured current (sum of all pixels within the scanned image), L is the film thickness, V is the applied tip-sample bias voltage, and A is the scanned area (image size).

3.2.5 Application of Bias and Signal Optimization

After establishing stable tip-sample contact, the measurement bias was applied, and the current amplification parameters were optimized. The amplifier gain was adjusted to ensure reliable signal detection while avoiding saturation. For PEDOT:PSS thin films, gain values in the range of 10^7-10^8 A/V provided stable measurements, with lower gain settings used at higher bias or reduced scan areas. Signal quality was monitored in real time, and baseline current offsets were corrected to achieve near-zero background levels. The setpoint current was maintained in the nanoampere range (~6 nA) to ensure stable contact. Samples were mounted using conductive silver paste to

minimize drift and improve electrical grounding. Measurements were performed across multiple scan sizes, in which increased bias enhanced current contrast but required a corresponding gain adjustment to maintain unsaturated signals.

3.2.6 Influence of Bias Voltage and Transport Regimes

The applied bias voltage is a critical experimental parameter in C-AFM measurements, particularly for organic and polymeric conductors such as PEDOT:PSS. Charge transport through organic media typically exhibits three distinct regimes in current-voltage (I-V) characteristics: linear (Ohmic) transport at low voltages [36], and non-linear behavior at moderate to high voltages governed by distributed carrier traps in the organic layer. Only within the low-voltage linear regime does Ohm's law remain valid, allowing reliable extraction of conductivity from current maps. Direct acquisition of point I-V curves in contact mode is often unreliable due to thermal drift and fluctuations in the tip-sample contact area under ambient conditions. To verify linearity, bias polarity switching tests can be performed during scanning. An example is shown in Figure 3.6, where the bias polarity is reversed midway through image acquisition [8].

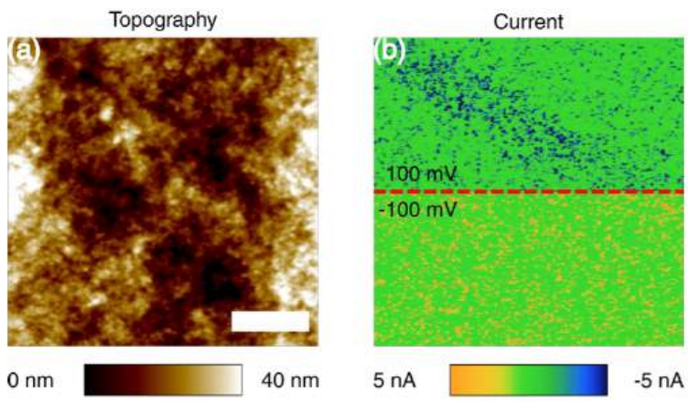

Figure 3.6. Verification of Ohmic transport regime by bias polarity switching during C-AFM imaging [8].

When the polarity is switched from +100 mV to −100 mV, the conductive domains exhibit a corresponding reversal in current contrast, transitioning from negative current (blue contrast) to positive current (yellow contrast) while maintaining a near-zero background signal. This symmetric response confirms Ohmic behavior within the selected bias range [8].

3.3 Thermal Measurement Methods

Thermal transport properties of the investigated thin films were characterized using two complementary photothermal techniques: PTR and TR. These non-contact optical methods enable the evaluation of thermal diffusivity and related thermophysical parameters by monitoring the thermal response to modulated optical excitation [9-12].

3.3.1 Photothermal Infrared Radiometry (PTR) Method

Photothermal infrared radiometry is a non-destructive technique used to determine thermal diffusivity and infrared absorption characteristics of materials. In contrast to Fourier transform infrared (FTIR) spectroscopy, PTR allows analysis of comparatively thick samples and does not require mirror-like surfaces, making it particularly suitable for polymeric and composite thin films.

In PTR measurements, a modulated optical beam heats the sample surface, generating periodic temperature oscillations. These oscillations produce infrared emission, which is detected and analyzed as a function of modulation frequency. By fitting the experimental response with an appropriate thermal model, parameters such as thermal diffusivity and effective infrared absorption coefficient can be extracted. In PTR, a modulated optical excitation heats the sample surface, generating periodic temperature oscillations that propagate into the material. These oscillations produce time-varying infrared emission, which is detected and analyzed as a function of modulation frequency. Because thermal diffusion length depends on frequency, depth-dependent thermal transport information can be extracted.

The excitation source was a diode-pumped solid-state (DPSS) laser operating at 532 nm, with a continuous output power of approximately 800 mW. The laser intensity was sinusoidally modulated over a frequency range of 100 Hz to 10 MHz using an acousto-optic modulator (AOM). Infrared radiation emitted from the thermally excited sample surface was collected using two off-axis, gold-coated parabolic mirrors. The collected emission was focused onto a mercury cadmium telluride (MCT) detector equipped with an anti-reflection-coated germanium window. For spectrally resolved measurements, optical filters were positioned in front of the detector. The detected signal was processed using a lock-in amplifier synchronized with the modulation frequency and subsequently analyzed via a computer interface. At the laser output, both pump and probe beams exhibited Gaussian intensity profiles with a measured $1/e^2$ diameter of approximately 2.42 mm. Figure 3.7 shows PTR experimental setup used for measuring thermal conductivity of PEDOT:PSS thin films [9-12].

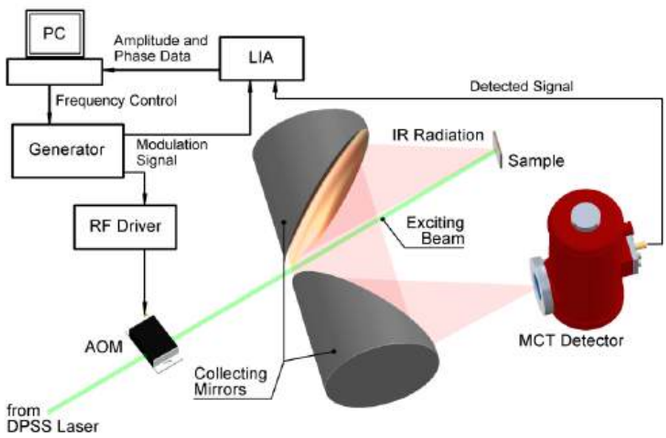

Figure 3.7. The PTR experimental set-up used in the study [9].

3.3.2. PTR Signal Description

The PTR signal originates from thermally induced infrared emission caused by laser heating. The emitted radiance depends on the instantaneous surface temperature and can be expressed, to first order, as proportional to the temperature modulation amplitude [9-12]:

$$\Delta E \approx T^3 \Delta T, \qquad (3.13)$$

Where T is the absolute temperature, ΔT the temperature oscillation amplitude. The cubic dependence arises from Planck's radiation law under small-signal approximation. Figure 3.8

illustrates the dependence of the PTR signal on temperature for a GaAs wafer coated with a 50 nm titanium (Ti) layer at a modulation frequency of 1 kHz. The experimental data exhibit a clear T^3 dependence, and the fitted curve confirms the validity of the theoretical PTR model described by Eq. (3.13).

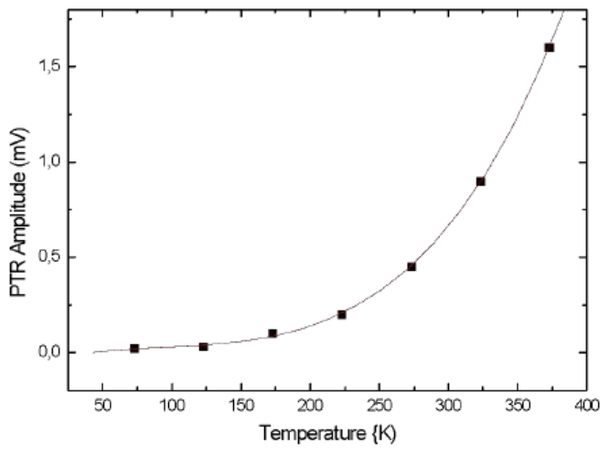

Figure 3.8. Dependence of the PTR signal on temperature for a GaAs wafer coated with a 50 nm Ti layer measured at 1 kHz modulation frequency. The fitted curve confirms the T^3 behavior predicted by PTR theory [9].

Because the thermal diffusion length decreases with increasing modulation frequency, high-frequency measurements probe near-surface regions, whereas low-frequency measurements probe deeper layers. Consequently, frequency-resolved PTR enables simultaneous extraction of: (i) thermal diffusivity, (ii) infrared absorption coefficient and (iii) carrier-related recombination contributions (in semiconductors). The PTR response typically contains both thermal and electronic components. In semiconducting materials, photocarrier generation modifies emissivity through plasma effects, although in polymeric systems the signal is predominantly thermal.

3.3.3 Thermoreflectance (TR) Method

The TR technique is an optical pump-probe technique used to determine thermal transport properties by monitoring temperature-induced variations in surface reflectivity. The method exploits the intrinsic temperature dependence of the optical reflectance of a metallic transducer layer. By periodically heating the sample and measuring the resulting reflectivity modulation, quantitative information about thermal diffusivity, thermal conductivity, and interfacial thermal resistance can be extracted. In practice, a thin metallic film is deposited on the sample surface to serve as a transducer. This metal layer converts absorbed optical energy into heat and simultaneously provides a temperature-sensitive reflectivity response. When the temperature of the metallic layer increases, phonon populations rise, leading to enhanced electron–phonon scattering. These scattering processes modify the metal's dielectric function and consequently alter its reflectance. The measured change in reflectivity is therefore directly related to the transient temperature oscillation at the surface. The relative change in reflectivity is expressed as [13-15]:

$$S_{TR} = \frac{\Delta R}{R} = \left(\frac{1}{R}\frac{\partial R}{\partial T}\right)\Delta T = C_{TR}\Delta T \qquad (3.14)$$

Where $\frac{\Delta R}{R}$ is the normalized reflectivity variation, ΔT represents the temperature oscillation amplitude, and C_{TR} is the thermoreflectance coefficient of the metallic transducer. Since the

reflectivity variation is linearly proportional to temperature within the small-signal approximation, TR provides high sensitivity to sub-Kelvin temperature oscillations. An additional advantage of this method is its applicability over a broad temperature range, including cryogenic conditions (down to approximately 50 K), making it suitable for temperature-dependent thermal studies. Figure 3.9 shows the temperature dependence of the TR signal measured from a GaAs wafer coated with a 50-nm-thick Au layer. In contrast to the PTR signal, which follows a T^3 dependence, the thermoreflectance signal exhibits an approximately linear dependence on temperature. The linear fitting of the experimental data confirms the proportional relationship between the TR signal and the surface temperature variation predicted by Eq. (3.14).

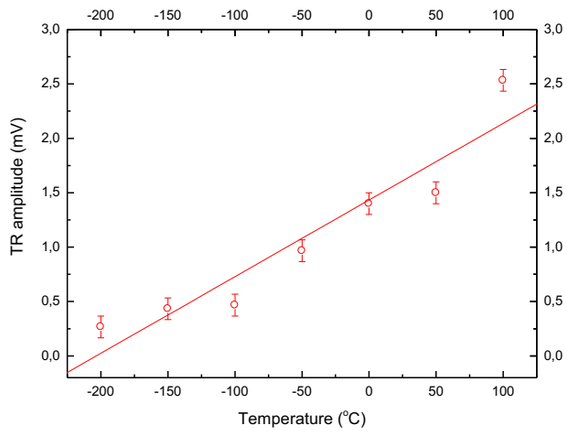

Figure 3.9. Temperature dependence of the TR signal for a GaAs wafer coated with a 50 nm thick Au transducer layer. The linear fit confirms the proportional dependence of the TR signal on temperature [9].

3.3.4 Frequency-Domain Thermoreflectance (FDTR) Experimental Configuration

A schematic representation of the frequency-domain thermoreflectance (FDTR) system employed in this study is presented in Figure 3.10. The experimental arrangement was configured in a pump-probe geometry to generate periodic thermal excitation and to monitor the resulting surface temperature response via reflectivity modulation. Thermal excitation was provided by a continuous-wave pump laser operating at a wavelength of 488 nm (CNI Laser). The pump beam intensity was sinusoidally modulated over a frequency range spanning 100 Hz to 1.5 MHz using an acousto-optic modulator (AOM 3080-120, Crystal Technology Inc., San Jose, CA, USA). The modulation signal was generated by a 30 MHz arbitrary waveform generator (Agilent 33522A, 250 MSa/s, Agilent Technologies, Santa Rosa, CA, USA), allowing precise control of the excitation frequency. Surface temperature oscillations induced by the pump beam were monitored using a probe laser operating at 638 nm (Cobolt 06-01 Series). The probe beam intensity was maintained essentially constant to avoid introducing additional thermal loading. In this configuration, the probe laser functioned solely as a reflectivity sensor. The spatial characteristics of both beams were carefully characterized prior to measurement. Beam diameters were determined using a DataRay scanning slit beam profiler (model 24-215), capable of resolving beam sizes from 2 μm to 4 mm. At the laser output, both pump and probe beams exhibited Gaussian intensity profiles with a measured $1/e^2$ diameter of approximately 2.42 μm.

During operation, the pump laser power was gradually increased to achieve measurable thermal modulation while ensuring that the probe laser power remained sufficiently low, typically within the milliwatt range, to prevent unintended heating effects. Optical alignment of the pump and probe beams was achieved using a combination of beam splitters and optical isolators, integrating both beams along a common optical axis. A dichroic mirror was employed to combine and direct the

beams toward the sample surface. Final focusing was accomplished using a microscope objective lens (Mitutoyo MY10X-803, Kawasaki, Japan), producing a co-localized excitation and detection spot. Following interaction with the sample, the reflected pump and probe beams retraced the incident optical path. Spectral filtering was implemented to isolate the probe signal: the pump contribution was suppressed using a notch filter, while additional inline bandpass filters ensured selective detection. The filtered probe beam was directed to a silicon photodetector (PDA8A2, fixed-gain detector, 320-1000 nm bandwidth, 50 MHz, 0.5 mm² active area; Thorlabs, Newton, NJ, USA), where optical intensity variations were converted into electrical voltage signals.

The detector output was analyzed using a lock-in amplifier synchronized to the pump modulation frequency. Both in-phase and out-of-phase components of the thermal response were recorded as functions of modulation frequency and spatial offset. The phase lag between excitation and detection provided information on heat diffusion dynamics, while the signal amplitude reflected the magnitude of temperature oscillations. It should be noted that minor additional phase delays could arise from post-sample optical components. These instrumental contributions were accounted for during calibration and data analysis [13].

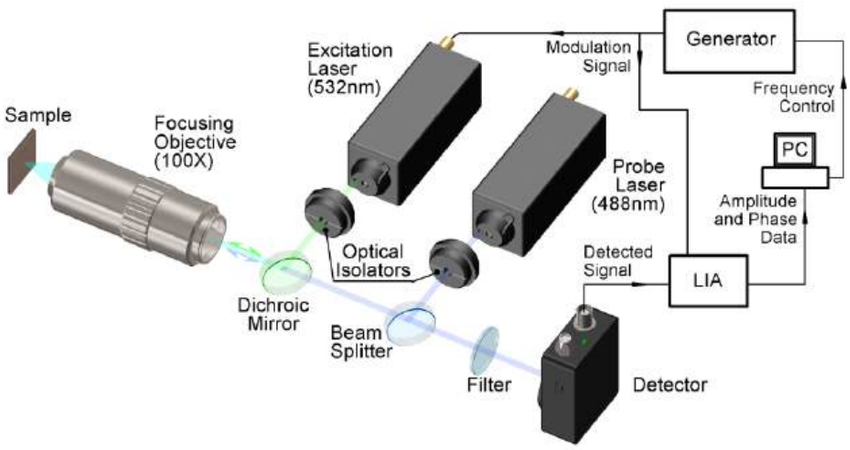

Figure 3.10. Typical FDTR experimental set-up [13].

3.3.5 Theoretical Model for Thermal Measurements

The thermal response measured in frequency-domain thermoreflectance experiments is interpreted using a multilayer heat-diffusion framework that describes periodic heat transport within the sample structure. Under harmonic optical excitation, the temperature field generated by the modulated pump beam propagates through the layered system as a thermal wave. The resulting surface temperature oscillation, detected through reflectivity modulation, can be expressed using a cylindrical heat-flow formulation combined with Hankel transformation. The complex thermoreflectance signal is given by [13-15]:

$$\theta_{TR} = \frac{-Q}{2\pi} \int_0^{\infty} \frac{D}{C} e^{-\frac{(\lambda d)^2}{8}} \lambda \, d\lambda \qquad (3.15)$$

where λ is the Hankel transform variable, Q represents the absorbed pump beam power (intensity), and d denotes the pump beam spot radius. The coefficients C and D are multilayer thermal response parameters derived from the transfer-matrix formalism describing heat propagation across the

stacked layers. For a multilayer system, heat transport is modeled through the product of individual layer and interface matrices such that

$$\begin{bmatrix} An & Bn \\ Cn & Dn \end{bmatrix} = M_3\, M_{32}\, M_2\, M_{21}\, M_1 \qquad (3.16)$$

where each matrix corresponds either to a material layer or an interface separating adjacent layers. The elements of the layer matrix are defined as:

$$A_n = cos\ h\ (\sigma_n l_n) = D_n\ ; B_n = \frac{sinh\ (\sigma_n l_n)}{k_{\perp n}\sigma_n}; C_n = -k_{\perp n}\sigma_n\ sinh\ \ h\ (\sigma_n l_n) \qquad (3.17)$$

Here, l_n denotes the thickness of the layer n, $k_{\perp n}$ is its cross-plane thermal diffusivity, and σ_n represents the complex thermal wavevector governing heat diffusion within that layer. In anisotropic materials, where thermal transport differs along in-plane and cross-plane directions, the thermal wavevector is expressed as:

$$\sigma^2 = \frac{k_{\parallel}}{k_{\perp}}(\lambda^2 + i\omega\rho C) \qquad (3.18)$$

Where $k_{\parallel}$ and $k_{\perp}$ representing the in-plane and cross-plane thermal conductivities, respectively. The parameter ω corresponds to the angular modulation frequency of the pump beam, while ρC is the volumetric heat capacity. The ratio $\frac{k_{\parallel}}{k_{\perp}}$ defines the thermal anisotropy factor of the material system. Thermal boundary resistance at interfaces is incorporated through interface matrices of the form

$$M_{n,n+1} = \begin{bmatrix} 1 & -R_{n,n+1} \\ 0 & 1 \end{bmatrix} \qquad (3.19)$$

Where $R_{n,n+1}$ denotes the thermal boundary resistance between adjacent layers. The combined thermoreflectance-photothermal radiometry (TR-PTR) modeling approach enables extraction of key thermophysical parameters, including cross-plane and in-plane thermal conductivities, thermal diffusivity, anisotropy ratios, and interfacial thermal resistances, by simultaneously fitting experimentally measured phase and amplitude responses as functions of modulation frequency. By combining the complementary sensitivities of TR and PTR measurements, the reliability of parameter estimation is significantly improved, particularly for multilayer thin-film systems exhibiting anisotropic heat transport. The frequency-dependent thermal response provides information sighthinto-surface and bulk thermal transport mechanisms, allowing denabled characterization of the PEDOT:PSS thin films and their interfaces. To evaluate the reliability and uniqueness of the extracted parameters, a comprehensive sensitivity analysis was performed prior to the final fitting procedure.

3.3.5.1 Sensitivity Analysis of Thermal Parameters For PEDOT:PSS Thin Films

A sensitivity analysis was conducted to examine the influence of thermal parameters on the FDTR response of the PEDOT:PSS thin-film structure and to assess the feasibility of independently extracting these parameters from experimental measurements. In multilayer thermal systems, several fitting parameters may yield similar responses in the measured signal, leading to parameter coupling and uncertainty during fitting. Therefore, evaluating the sensitivity behavior is essential before performing the final thermal parameter estimation.

Figures 3.11 and 3.12 present the sensitivity vectors plotted with respect to one another for the PEDOT:PSS sample. The sensitivity coefficients describe the response of the measured thermal signal to variations in thermophysical quantities such as cross-plane thermal conductivity (k_z), in-plane thermal conductivity (k_r), thermal diffusivity (α), and effective volumetric heat capacity (C_{eff}). The modulation frequency was varied from 10 Hz to 2 MHz to investigate the thermal response at different heat penetration depths. The sensitivity analysis was performed using the thermal response of the GaAs substrate as a reference in order to evaluate the thermal transport behavior of the PEDOT:PSS thin-film system. The obtained sensitivity relationships provide insight into the coupling between the sample's in-plane and cross-plane thermal transport properties. Figure 3.11 illustrates the correlation between the cross-plane thermal conductivity and thermal diffusivity for different anisotropy coefficients. In contrast, Figure 3.12 shows the sensitivity dependence between the in-plane thermal conductivity and the effective volumetric heat capacity while maintaining a fixed anisotropy ratio. As observed in Figure 3.12 (b), the sensitivity vectors S(k_r), and S(C_{eff}) exhibit an approximately linear relationship. This behavior indicates a strong correlation between the in-plane thermal conductivity and the volumetric heat capacity, making it difficult to determine either parameter independently from FDTR measurements alone. Consequently, simultaneous estimation of these parameters introduces substantial uncertainty into the fitting procedure. To reduce this ambiguity, the anisotropy coefficient was fixed prior to the final optimization of the thermal transport parameters.

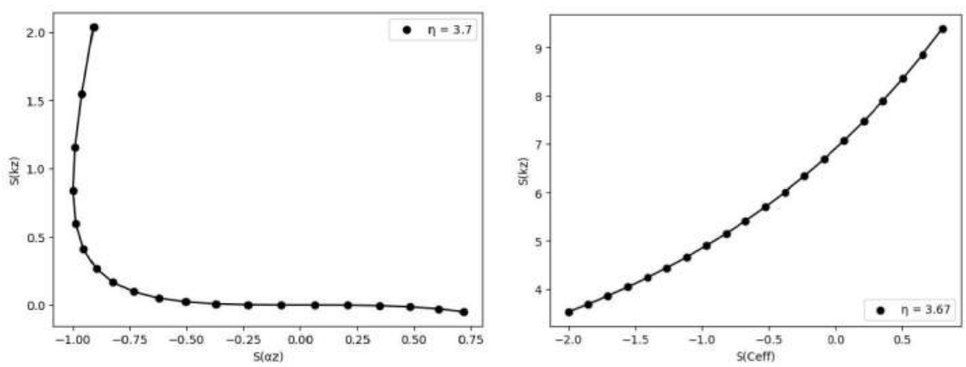

(**a**) (**b**)

Figure 3.11. Sensitivity coefficient analysis for the PEDOT:PSS thin-film system: (a) relationship between cross-plane thermal conductivity and cross-plane thermal diffusivity for different anisotropy coefficients; (b) effective volumetric heat capacity as a function of cross-plane thermal conductivity [9].

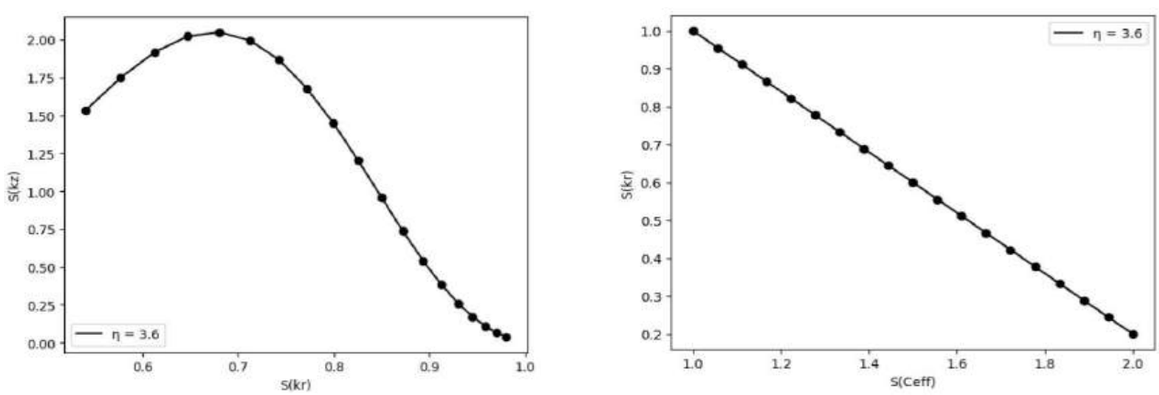

(**a**) (**b**)

Figure 3.12. Sensitivity coefficient analysis for the PEDOT:PSS thin-film system: (a) correlation between cross-plane and in-plane thermal conductivities for optimized anisotropy coefficients; (b) relationship between effective volumetric heat capacity and in-plane thermal conductivity [9].

3.3.5.2 Procedure for Estimating the Thermal Transport Properties of PEDOT:PSS Thin Films

Accurate determination of the in-plane thermal transport properties remains challenging because multiple thermophysical parameters exhibit similar sensitivity distributions over the modulation frequency range. Consequently, all parameters cannot be independently extracted simultaneously using a single experimental fitting procedure. A detailed description of this fitting methodology and the associated parameter-correlation analysis was previously reported in our earlier work on combined TR-PTR thermal characterization of nanolayers. To overcome this limitation, the anisotropy coefficient (η) was constrained prior to the final optimization process, as shown in Figure 3.13 (a). Once the anisotropy ratio is fixed, reliable estimation of the remaining thermal transport parameters becomes possible. In addition, the reduced chi-square (χ^2) analysis presented in Figure 3.13 (b) and summarized in Table 3.1 indicates that optimization of the anisotropy coefficient significantly improves the fitting stability and accuracy of the thermal measurements. Therefore, the thermal characterization of the PEDOT:PSS thin films was carried out using an alternative fitting strategy in which the anisotropy index was optimized through reduced chi-square minimization. The optimized η values obtained from this procedure are listed in Table 3.2.

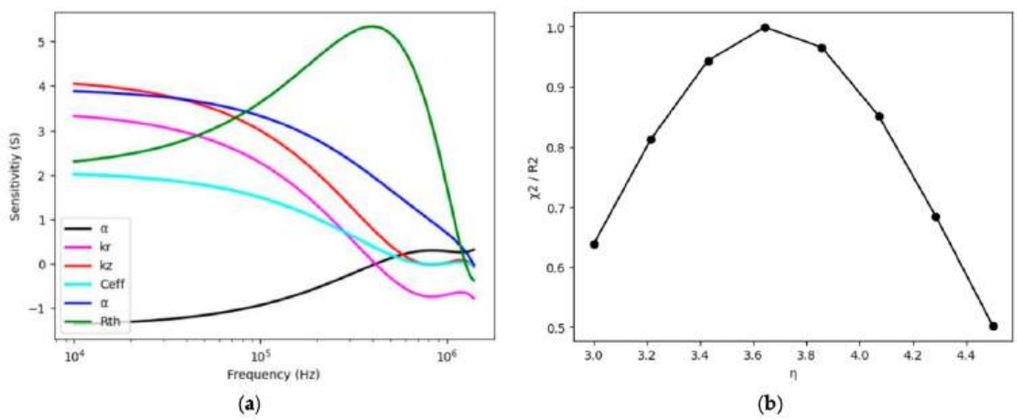

Figure 3.13. (a) Sensitivity analysis of the thermal transport parameters of the PEDOT:PSS thin-film structure as a function of modulation frequency for parameters reported in Table 3.1; (b) variation of the reduced chi-square (χ^2) values with the anisotropy coefficient (η) [9].

Table 3.1. Parameters assumed constant in the FDTR calculations [9].

Parameters	Assumed Values
Spot Size (μm)	2.42 (FDTR)
κ (glass) W/(m·K)	1.38
$k_1 = k_{Au}$ (W/m-K)	105 ± 9.9
$\alpha_1 = \alpha_{Au}$ (m^2/s)	1.23×10^{-5}
$d_1 = d_{Au}$ (nm)	20
d_2 (nm) (PEDOT:PSS)	480
d_{Ti} (nm)	20
d_{Al} (nm)	50
d_{Glass} (mm)	1
k (Ti) (W m^{-1} K^{-1})	16.8
k (Al) (W m^{-1} K^{-1})	200
$\alpha_1 = \alpha_{Glass}$ (m^2/s)	0.34×10^{-6}
ρC_v (Al) ($J \cdot cm^{-3} \cdot K^{-1}$)	0.98×10^{6}
ρC_v (Au) ($J \cdot m^{-3} \cdot K^{-1}$)	3.6×10^{6}

Table 3.2. Anisotropy coefficient (η) values obtained for different fitting conditions and corresponding R^2 values [9].

η	R^2
3	0.88
3.3	0.9
3.45	0.92
3.6	0.9367
3.67	0.9645
3.8	0.917
4.11	0.89
4.5	0.88

The anisotropy coefficient of the PEDOT:PSS samples was determined through reduced chi-square (χ^2) optimization of the fitting procedure. The optimized η values corresponding to the best cross-plane fitting results are summarized in Table 3.2. The observed correlations between the thermal transport parameters are consistent with previously reported studies. The extracted cross-plane thermal properties show good agreement with the optimized anisotropy coefficient of approximately η≈ 3.67 for the investigated sample. The optimized thermal transport parameters for both in-plane and cross-plane directions, obtained using Equation 3.15, are presented in Table 3.3.

Table 3.3. Optimized in-plane and cross-plane thermal transport properties of the PEDOT:PSS thin films obtained from the TR–PTR fitting procedure using Equation (3.15) [9].

Geometry	Optimized Pump Modulation Frequency Range (kHz)	Thermal Conductivity (W/m-K)	Thermal Diffusivity ($\times 10^{-7}$ m^2/s)	Thermal Boundary Resistance ($\times 10^{-9}$ m^2 KW^{-1})	χ^2
cross-plane	10-1240	0.182	1.48254	1.6245	94.914

3.3.5.3 Description of fitting procedure for Thermal Measurements

The fitting procedure solves an inverse heat-transfer problem in which the unknown thermophysical properties of Layer 2 (k_2, α_2, R_{32}), are estimated together with an amplitude scaling factor A and a phase offset ϕ. To ensure positivity of the physical parameters and improve numerical conditioning, the optimization is performed in logarithmic space using the parameter vector

$$\mathrm{p} = [\log_{10} k_2, \log_{10} \alpha_2, \log_{10} R_{32}, \log_{10} A, \phi] \qquad (3.20)$$

The optimization is performed using the Trust-Region Reflective (TRF) nonlinear least-squares algorithm implemented in the SciPy library. The residual vector minimized by the optimizer combines both amplitude and phase discrepancies between the measured and simulated PTR responses:

$$\mathrm{r(p)} = \begin{bmatrix} \dfrac{|\,\mathrm{y_{model}}\,| - \mathrm{A_{exp}}}{\mathrm{A_{exp}} + \epsilon} \\ w_\phi \cdot \Delta\phi_{\mathrm{wrapped}} \end{bmatrix} \qquad (3.21)$$

where $\mathrm{y_{model}} = A\exp(-i\phi)\sqrt{f} \cdot \mathrm{T_{surf}}(\omega)$ incorporates the f dependence characteristic of radiometric detection, $\Delta\phi$ is the wrapped phase difference (using arctan2), and $w\phi$ is the configurable phase weight (default 1.0). To improve robustness against local minima, the software employs a multi-start optimization strategy implemented in the fit_ptr_3d routine. Multiple

independent optimization runs are executed in parallel using the joblib framework. The first run uses physically motivated initial parameter estimates, while the remaining runs introduce controlled random perturbations to explore different regions of the parameter space. By default, 25 starting points are evaluated, although this number can be adjusted by the user. All optimization runs are constrained by physically meaningful bounds:

$$k_2 \in [0.02, 1]\ \mathrm{W\,m^{-1}\,K^{-1}}, \qquad (3.22)$$

$$\alpha_2 \in [10^{-9}, 10^{-4}]\ \mathrm{m^2\,s^{-1}}, \qquad (3.23)$$

$$R_{32} \in [10^{-9}, 10^{-6}]\ \mathrm{m^2\,K\,W^{-1}} \qquad (3.24)$$

The final solution is selected as the parameter set that yields the lowest objective function value among all optimization runs. The quality of the fit is evaluated using several complementary metrics. The coefficient of determination R^2 is calculated for the phase response, while a logarithmic coefficient of determination R^2_{amp} is computed in $\log_{10}$-space for the amplitude response to prevent high-amplitude low-frequency data points from dominating the evaluation. In addition, the normalized residual norm, res_norm. The complete fitting workflow is encapsulated within the PTRProcessor class and configured through the FittingProcessorBuilder pattern. The implementation combines vectorized numerical computations using NumPy, efficient caching of intermediate calculations, and parallel multi-start optimization, enabling practical execution times even when dozens of starting points are evaluated. The combination of a physically accurate transfer-matrix forward model with a robust multi-start least-squares optimization framework enables reliable extraction of thermal properties, including thermal conductivity, thermal diffusivity, anisotropy, and interfacial thermal resistance, from PTR measurements.

3.4 Wiedemann-Franz law (Correlation between thermal and Electrical Conductivity)

To investigate the relationship between electrical and thermal transport in PEDOT:PSS thin films, the Wiedemann-Franz law was used as a theoretical framework to relate electrical and thermal conductivities. This law states that in conductive materials, the ratio of the electronic contribution to thermal conductivity to the electrical conductivity is proportional to temperature. The Wiedemann-Franz relation is expressed as [16-20]:

$$k_e = L\sigma T \qquad (3.25)$$

Where k_e is the electronic thermal conductivity, σ is the electrical conductivity, T is the absolute temperature, and L is the Lorenz number (for conventional metals $L = 2.44 \times 10^{-8} W\Omega K^{-2}$). The Wiedemann-Franz law assumes that both heat and charge are transported by the same charge carriers. Although PEDOT:PSS is a polymeric conducting material and may deviate from ideal metallic behavior, the relation provides useful insight into the coupling between electrical and thermal transport processes [21, 22]. In this work, the Wiedemann-Franz framework was employed to compare experimentally measured electrical and thermal transport properties and to evaluate the contribution of electronic charge carriers to the overall thermal conductivity.

3.5 Cross-Plane Electrical Conductivity Measurements

The cross-plane electrical conductivity of the PEDOT:PSS thin films was measured using the experimental setup shown in Figure 3.14. The setup consisted of a Lake Shore Model 121 current source, a Keithley DAQ6510 data acquisition multimeter, and a probe station equipped with micromanipulators. During the measurements, a constant current was supplied by the Lake Shore current source, while the voltage drop across the sample was measured using the Keithley DAQ6510. The probe station ensured stable electrical contact with the sample throughout the measurements. A schematic illustration of the measurement principle is shown in Figure 3.15. In this configuration, the electrical current flows perpendicular to the film surface through both the PEDOT:PSS layer and the underlying GaAs:Si substrate. Consequently, the measured voltage corresponds to the combined electrical resistance of the multilayer structure.

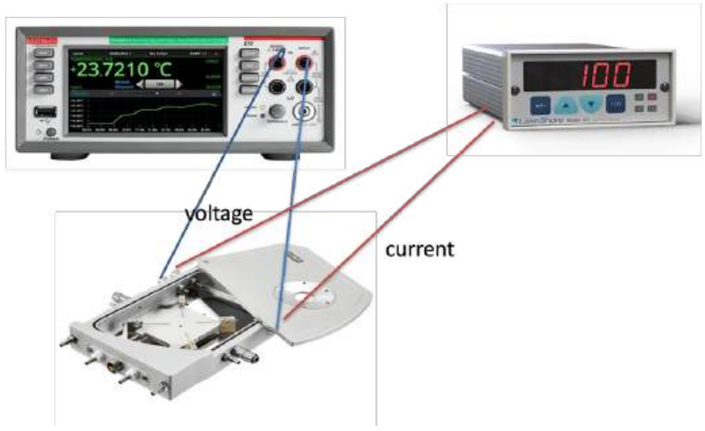

Figure 3.14. Experimental setup used for cross-plane electrical conductivity measurements, consisting of a Lake Shore Model 121 current source, Keithley DAQ6510 multimeter, and probe station.

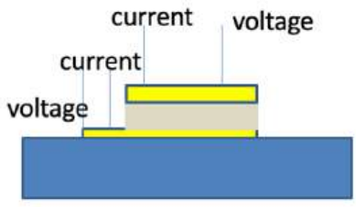

Figure 3.15. Schematic illustration of the cross-plane electrical conductivity measurement geometry for the PEDOT:PSS/GaAs:Si structure.

Assuming negligible contributions from the electrodes and contact resistances, the effective resistance of the sample can be expressed as:

$$R_{eff} = \frac{R_1 L_1 + R_2 L_2}{L_1 + L_2} \qquad (3.26)$$

where R_{eff} is the measured electrical resistance, R_1 and R_2 are the electrical resistances of the PEDOT:PSS film and the GaAs:Si substrate, respectively, while L_1 and L_2 represent their corresponding thicknesses. Using the measured total resistance and the substrate's known properties, the resistance of the PEDOT:PSS layer was determined. To verify the reliability of the measurement procedure, the electrical resistance of the GaAs:Si substrate was measured separately. The measured current–voltage characteristic is presented in Figure 3.16. A linear dependence

between current and voltage was observed, indicating ohmic behaviour of the substrate. From the slope of the fitted line, a resistance of 13±2 Ω was obtained.

Since GaAs:Si is expected to exhibit nearly isotropic electrical transport at room temperature, an independent in-plane resistance measurement was also performed using the electrical characterization system available at Ruhr University Bochum. The measured in-plane resistance was approximately 10 Ω, which is in reasonable agreement with the cross-plane measurement. The small deviation between the two values may be attributed to measurement uncertainty, slight anisotropy introduced by the doping process, and the omission of electrode and contact resistance effects in the simplified model. The cross-plane electrical conductivity of the PEDOT:PSS layer was subsequently calculated from the extracted film resistance using the measured film thickness and electrode contact area.

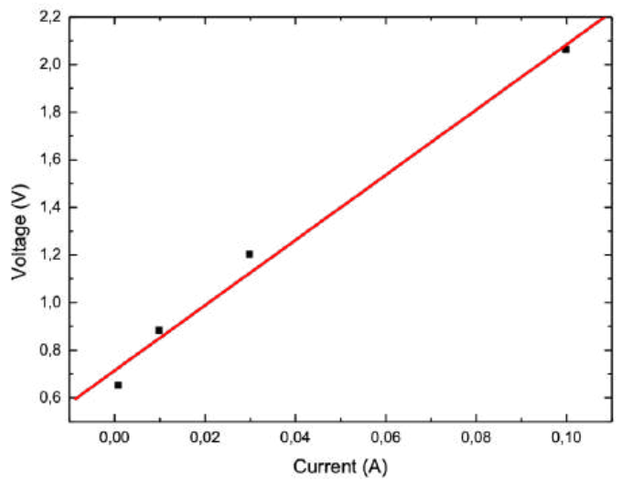

Figure 3.16. Current–voltage characteristic of the GaAs:Si substrate used to validate the measurement procedure. The extracted resistance was 13±2 Ω.

3.6 Conclusion

This chapter presented the experimental methods used to investigate the electrical and thermal transport properties of PEDOT:PSS thin films. In-plane electrical conductivity was determined using the four-probe Van der Pauw technique, while temperature-dependent measurements were performed using a closed-cycle cryostat to study thermally activated charge transport. Nanoscale cross-plane conductivity and local charge transport pathways were analyzed using C-AFM. Thermal transport properties were characterized using two non-contact photothermal techniques: PTR and FDTR. PTR measurements enabled the determination of thermal diffusivity and infrared absorption characteristics, whereas thermoreflectance measurements provided additional insight into heat diffusion dynamics through temperature-dependent reflectivity changes. These complementary electrical and thermal characterization methods provide a comprehensive framework for analyzing transport phenomena in PEDOT:PSS thin films. The techniques described in this chapter form the basis for the experimental results presented in the following chapters.

3.7 References

[1] D. A. Neamen, Semiconductor Physics and Devices, 4th ed. New York, NY, USA: McGraw-Hill, 2012.

[2] N. W. Ashcroft and N. D. Mermin, Solid State Physics. New York, NY, USA: Holt, Rinehart and Winston, 1976.

[3] S. M. Sze and K. K. Ng, Physics of Semiconductor Devices, 3rd ed. Hoboken, NJ, USA: Wiley, 2007.

[4] F. M. Smits, "Measurement of sheet resistivities with the four-point probe*," Bell Syst. Tech. J.*, **37**, 711–718, (1958).

[5] National Institute of Standards and Technology, "Hall Effect Measurements," Jul. 19, 2022. [Online]. Available: https://www.nist.gov/pml/nanoscale-device-characterization-division/popular-links/hall-effect. [Accessed: Jun. 4, 2026].

[6] C. Schulte-Braucks, "Einfluss von Licht und Gate-Spannung auf Dichte und Beweglichkeit von niederdimensionalen Halbleiter-Strukturen," M.S. thesis, Ruhr-Universität Bochum, Bochum, Germany, 2013.

[7] Park Systems, "Conductive AFM (C-AFM) Training Guide," ver. 1.0. [Online]. Available: https://www.parksystems.com. [Accessed: Jun. 4, 2026].

[8] A. J. Diaz, H. Noh, T. Meier, and S. D. Solares, "High-stress study of bioinspired multifunctional PEDOT:PSS/nanoclay nanocomposites using AFM, SEM and numerical simulation," *Beilstein J. Nanotechnol*., **8**, 2069–2082, (2017).

[9] A. Chatterjee, M. S. Swapna, A. Mikaeeli, M. Khalid, D. Korte, A. D. Wieck, and M. Pawlak, "Photothermal infrared radiometry and thermoreflectance—Unique strategy for thermal transport characterization of nanolayers," *Nanomaterials,* **14**, 1711, (2024).

[10] M. Pawlak, N. Jukam, T. Kruck, D. Dziczek, A. Ludwig, and A. D. Wieck, "Measurement of thermal transport properties of selected superlattice and thin films using frequency-domain photothermal infrared radiometry," *Measurement*, **166**, 108226, (2020).

[11] M. Pawlak, "Photothermal, photocarrier, and photoluminescence phenomena in semiconductors studied using spectrally resolved modulated infrared radiometry: Physics and applications," *J. Appl. Phys*., **126**,150902, (2019).

[12] Ł. Chrobak and M. Maliński, "On investigations of the optical absorption coefficient of gold and germanium implanted silicon with the use of the nondestructive contactless photothermal infrared radiometry," *J. Electron. Mater*., **48**,5110–5117, (2019).

[13] A. Chatterjee, N. Spitzer, T. Kruck, P. Song, A. Ludwig, A. D. Wieck, J. Ordonez-Miranda, and M. Pawlak, "Beam-offset thermoreflectance with Bayesian optimization to measure the anisotropic thermal properties of semiconductor superlattices," *arXiv preprint arXiv:*2602.18840, 2026.

[14] D. G. Cahill, "Analysis of heat flow in layered structures for time-domain thermoreflectance," Rev. Sci. *Instrum*., **75**, 5119–5122, (2004).

[15] J. Zhu, D. Tang, W. Wang, J. Liu, K. W. Holub, and R. Yang, "Ultrafast thermoreflectance techniques for measuring thermal conductivity of thin films," *J. Appl. Phys*., **83**, 3264–3269, (1998).

[16] M. Kong, "Thermal Conductivity and Advanced Optical Characterization of PEDOT:PSS Based Films," Ph.D. dissertation, 2022.

[17] K. Kondratenko, D. Guérin, X. Wallart, S. Lenfant, and D. Vuillaume, “Thermal and electrical cross-plane conductivity at the nanoscale in poly(3,4-ethylenedioxythiophene): trifluoromethanesulfonate thin films,” *Nanoscale*, **14**, 6075–6083, (2022).

[18] J. Guo, D. Wang, Z. Li, H. Zhang, J. Zhang, Z. Zhang, L. Sun, J. Sun, J. Zhou, C. Di, and J. Dou, “Unraveling intrinsic thermal conductivity in layered conductive MOF single crystals,” 2026.

[19] L. Liu, L. Liang, L. Deng, H. Wang, and G. Chen, “Is there a constant Lorentz number for organic thermoelectric materials?” *Appl. Mater. Today*, **27**, 101496, (2022).

[20] J. H. Song, J. Jeong, Y. Choi, S. Cho, I. Imae, and J. Kwak, “Recent advances in engineering electronic and thermal properties of PEDOT:PSS for efficient thermoelectric energy conversion,” *J. Mater. Chem*. C, **13**, 14144–14167, (2025).

[21] J. Liu, X. Wang, D. Li, N. E. Coates, R. A. Segalman, and D. G. Cahill, “Thermal conductivity and elastic constants of PEDOT:PSS with high electrical conductivity,” *Macromolecules*, **48**, 585–591, (2015).

[22] A. Weathers, Z. U. Khan, R. Brooke, D. Evans, M. T. Pettes, J. W. Andreasen, X. Crispin, and L. Shi, “Significant electronic thermal transport in the conducting polymer poly(3,4-ethylenedioxythiophene),” *Adv. Mater*., **27**, 2101–2106, (2015).

Chapter 4

Transport Properties in Poly(3,4-ethylenedioxythiophene) poly(4-styrenesulfonic acid) (PEDOT:PSS)

(Mott Variable-Range Hopping and Tunneling Models)

4.1. Introduction

Understanding charge transport mechanisms in conducting polymers is essential for interpreting their electrical behavior and optimizing their performance in organic electronic devices. Among these materials, PEDOT:PSS has emerged as one of the most widely used conductive polymers due to its favorable stability, transparency, and solution processability. However, unlike crystalline inorganic semiconductors, its electrical transport cannot be described using conventional band theory alone. Instead, the presence of structural disorder, phase segregation, and localized electronic states necessitates the use of alternative transport models. In this chapter, the mechanisms governing charge transport in PEDOT:PSS are examined through two principal theoretical approaches: the Mott variable-range hopping model and the fluctuation-induced tunneling model. To establish the physical basis of these models, charge transport in disordered conducting polymers is first discussed, followed by morphology-dependent transport considerations specific to PEDOT:PSS. Finally, these mechanisms are compared with transport behavior in disordered metallic systems such as ITO, which is relevant as a substrate material in this work.

4.2 Charge Transport in Conducting Polymers

Organic electronic materials, commonly referred to as plastic electronics, constitute a multidisciplinary class of systems based on carbon-derived semiconductors, including π-conjugated polymers and small organic molecules. In contrast to conventional inorganic semiconductors such as silicon or gallium arsenide, organic materials exhibit fundamentally different electronic behavior arising from their molecular structure and intrinsic disorder. One of the defining characteristics of organic semiconductors is the presence of structural and energetic disorder. Variations in chain conformation, intermolecular packing, and defect density disrupt long-range electronic delocalization. Furthermore, charge carriers in conjugated polymers are typically described as polarons or bipolarons due to strong coupling between electronic states and local lattice distortions. Combined with relatively low dielectric constants, these factors lead to large exciton binding energies and localized electronic states. As a consequence, charge transport in organic electronic materials is predominantly governed by thermally activated hopping processes rather than band-like conduction. Carrier mobility and electrical conductivity are therefore generally lower than those of crystalline inorganic semiconductors. Understanding the relationship between structural disorder and transport properties is thus central to the development of conducting polymer devices.

Conducting polymers are intrinsically disordered materials. They are composed of polymer chains with varying lengths and defects that are non-uniformly distributed along the backbone. As a result,

a range of conjugation lengths exists, that is, effective distances over which electrons can delocalize along the chains. π–π interactions between neighboring chains generate weak van der Waals forces, leading to varying degrees of chain stacking. Consequently, the material typically consists of crystalline domains, whose sizes may reach several tens of nanometers, embedded within amorphous regions [1,2,3]. In these disordered systems, charge transport occurs most rapidly along individual chains, more moderately between adjacent chains, and most slowly across lamellar planes [3,4]. Chain orientation may also be random along the x, y, or z axes, and transport properties are more favorable in the configuration represented in Figure 4.1 (a) than in Figure 4.1 (c). It is generally accepted that high carrier mobility depends strongly on the level of structural order and on the relative stacking of the chains. Therefore, optimizing transport properties in conducting polymers requires both high carrier mobility and efficient intra-and inter-chain charge transfer [5]. As emphasized by Anderson, the absence of crystal symmetry and long-range order leads to localization of charge-carrier wavefunctions, such that charge transport can occur only via quantum-mechanical hopping between localized sites.

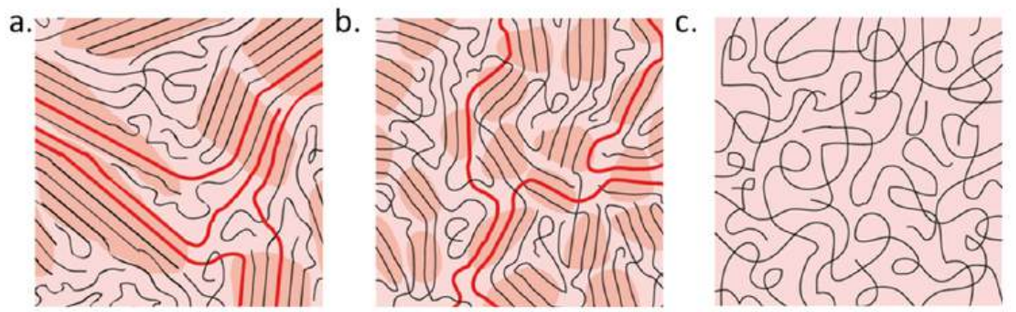

Figure 4. 1. Schematic illustration of polymer structures with different degrees of structural order: (a) highly ordered morphology, (b) partially disordered aggregates, and (c) fully disordered configuration. In systems with sufficient polymer density, extended chains (highlighted in red) can bridge ordered regions (darker areas) while largely preserving the conjugation length, thereby facilitating charge transport pathways [3].

These structural variations strongly influence charge transport pathways. In disordered polymer systems, transport is anisotropic in nature. Charge carriers move most efficiently along the conjugated polymer backbone, where orbital overlap is greatest. Transport between adjacent chains occurs at moderate rates through π–π stacking interactions, while conduction across lamellar stacking planes is comparatively slow (See Figure 4.2).

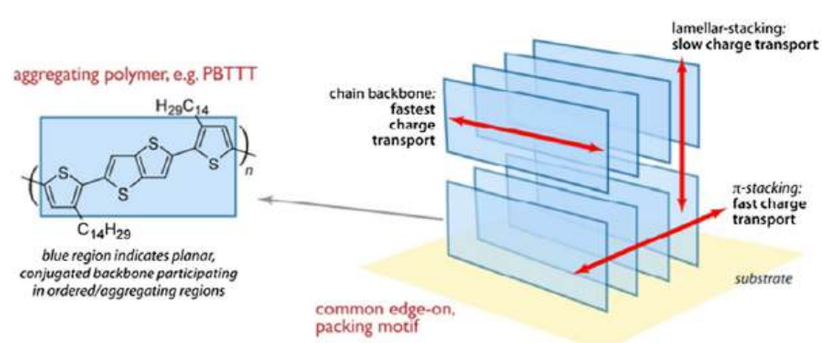

Figure 4.2. Schematic illustration of charge transport directions in conducting polymers with edge-on packing. Charge transport is fastest along the polymer backbone, moderate through π–π stacking between adjacent chains, and slowest across lamellar stacking [3].

Because polymer chains are randomly oriented along spatial axes, macroscopic conductivity represents an average over these directional mobilities. High carrier mobility is therefore closely linked to structural order and the degree of interchain stacking. Enhancing intra- and inter-chain coupling remains a key objective in optimizing transport properties in conducting polymers. From

a theoretical perspective, the impact of disorder on electronic transport is well described by Anderson localization [6]. The absence of long-range crystalline symmetry leads to the spatial localization of charge-carrier wavefunctions. Under such conditions, carriers cannot propagate through extended band states and must instead propagate via quantum-mechanical transitions between localized sites. This disorder-induced localization forms the physical basis for hopping and tunneling transport models, which are discussed in the following sections.

4.3 Temperature Dependence of Charge Transport

Charge transport mechanisms in conducting polymers are most evaluated through their temperature-dependent electrical properties. Several experimental approaches can be used to probe transport behavior, including measurements of electrical conductivity as a function of temperature from room temperature down to cryogenic regimes, temperature-dependent Seebeck coefficient analysis, magnetoresistance studies, and field-effect measurements. Among these techniques, temperature-dependent conductivity remains the most widely used, primarily due to its experimental accessibility and its effectiveness in identifying dominant transport regimes and activation processes [7,8]. The electrical conductivity of a material is expressed as:

$$\sigma = n_c e \mu \qquad (4.1)$$

Where n_c denotes the charge carrier density, e the elementary charge, and μ the carrier mobility. The temperature dependence of conductivity therefore reflects variations in both carrier concentration and mobility, which are governed by the underlying electronic structure and scattering processes. In metallic systems, band theory predicts the absence of an energy gap between the highest occupied and lowest unoccupied electronic states. At absolute zero, the highest occupied level corresponds to the Fermi level, and there is no sharp separation between filled and empty states. As the temperature increases, electrons can be thermally excited to higher energy states. However, this increased excitation does not lead to higher conductivity. Instead, enhanced thermal vibrations increase the frequency of electron-phonon collisions, thereby reducing carrier mobility and shortening the mean free path. Consequently, electrical conductivity decreases with increasing temperature (Figure 4.3 (d)).

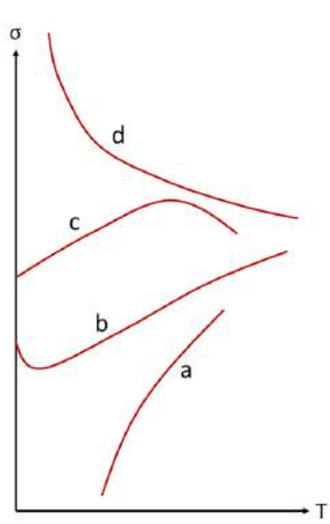

Figure 4.3. Temperature dependence of electrical conductivity for different transport regimes: (a) semiconductor behavior, (b-c) disordered or semiconducting metal behavior, and (d) metallic behavior [3].

This reduction in conductivity does not continue indefinitely. A lower limit exists, defined by the minimum metallic conductivity compatible with the shortest possible mean free path. This threshold is commonly referred to as the Mott-Ioffe-Regel limit. In contrast, classical semiconductors such as silicon exhibit a different temperature dependence (Figure 4.3 (a)). At absolute zero, the presence of a band gap between the valence and conduction bands prevents charge transport. As the temperature increases, electrons are thermally excited across the band gap into the conduction band, leading to an increase in carrier density. Because carrier concentrations remain relatively low compared to metals, scattering effects are less dominant, and conductivity increases with temperature. Conducting polymers do not conform strictly to either metallic or semiconductor transport behavior. Instead, their conductivity reflects thermally activated processes governed by disorder and carrier localization. Within hopping-based transport frameworks, the activation energy depends on both the spatial separation and the energetic barrier between localized states, as well as the dimensionality of the transport network. In this context, the parameter n describes the effective dimensionality of conduction. For $n = 3$ transport corresponds to three-dimensional hopping between localized sites, typically associated with polaronic or bipolaronic quasiparticles extending over several PEDOT monomer units [9]. As n decreases, preferred conduction pathways emerge, indicating increasing structural anisotropy or ordering within the material. However, interpretation of dimensionality requires caution. A one-dimensional exponent may also arise from alternative mechanisms. For example, electron-electron Coulomb interactions at low temperature can produce transport behavior resembling one-dimensional hopping. Similarly, tunneling-dominated transport between neighboring conductive domains may yield comparable temperature dependences [10-12]. It is therefore essential to correlate dimensionality analysis with morphological characterization and complementary measurements, such as magnetoresistance, to distinguish among one-dimensional hopping along aligned polymer chains, three-dimensional hopping among localized states, and tunneling between adjacent polaronic clusters.

4.4 Transport Properties in Conducting Polymers: PEDOT:PSS

Among the various conducting polymers investigated to date, PEDOT has attracted considerable attention in both academic research and industrial applications. This interest stems primarily from its relatively high electrical conductivity, excellent environmental stability, and potential optical transparency in the visible range. Compared with many other polythiophene derivatives, PEDOT exhibits superior electrochemical, thermal, and ambient stability of its electrical properties [13]. These characteristics have made PEDOT one of the most widely studied conducting polymers over the past two decades, as reflected in numerous review articles that address its synthesis, physical properties, strategies for enhancing conductivity, and technological applications [14-24]. A particularly important property of PEDOT is its high and stable electrical conductivity. Reported values have reached approximately 6259 S/cm in thin films and up to 8797 S/cm in single crystals [25–29]. These values are remarkable because they approach the conductivity of highly conductive metals such as silver and copper, differing by roughly one order of magnitude. While these results demonstrate the significant progress achieved in improving PEDOT conductivity, the wide range of reported values in the literature indicates that the mechanisms governing charge transport in PEDOT-based materials are not yet completely understood. In particular, the role of structural disorder and morphology in limiting charge transport remains an important subject of investigation. PEDOT is synthesized from ethylenedioxythiophene (EDOT) monomers. In its neutral form, PEDOT is unstable and readily oxidizes in air, and it is also poorly soluble in most common organic

solvents, which limits its direct processability. To overcome these limitations, PEDOT is typically combined with the polyelectrolyte poly(styrenesulfonate) (PSS), forming a water-dispersible complex known as PEDOT:PSS. In this composite material, PEDOT exists in an oxidized and positively charged state, while PSS acts as a negatively charged counter-ion. Each styrenesulfonate repeat unit contains a sulfonic acid (SO_3H) group that compensates the positive charge of the PEDOT backbone and stabilizes the dispersion. See Figure 4.4.

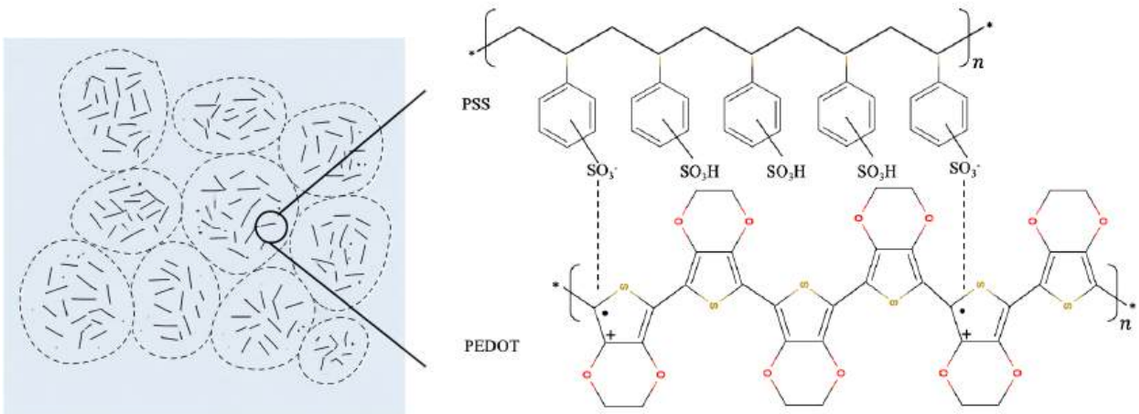

Figure 4.4. Illustration of PEDOT:PSS film morphology and chemical structure. Left: top-view representation of PEDOT:PSS particles forming the thin film, surrounded by a PSS-rich surface layer, with PEDOT chains depicted as short segments. Right: molecular structures of the PEDOT and PSS components present in the film.

PEDOT:PSS is typically synthesized through oxidative polymerization of EDOT in the presence of PSS, commonly using sodium peroxodisulfate as the oxidizing agent [25]. During this process, PEDOT is formed in a highly conducting cationic state. The degree of polymerization of PEDOT is relatively limited, and the material is generally considered to consist of oligomeric segments containing up to approximately twenty repeating units. In contrast, PSS has a much higher molecular weight and serves both as a charge-balancing counter-ion and as a dispersing matrix that stabilizes PEDOT chains in aqueous media.

The resulting PEDOT:PSS dispersions form gel-like colloidal particles that can be readily processed into thin, transparent, and electrically conductive films. Commercial formulations, such as Baytron P, are widely used and can be deposited onto hydrophilic substrates through techniques such as spin coating or dip coating. The properties of the resulting films depend on several parameters, including the solid content of the dispersion, the doping level, particle size, and the presence of additives. Typically, PEDOT:PSS films exhibit a work function of approximately 4.8 eV. Because of the sulfonate groups present in PSS, these aqueous dispersions are acidic, with pH values generally ranging between 1.5 and 2.5 at room temperature. Understanding the relationship between the structural organization of PEDOT:PSS and its electrical transport properties is therefore essential for improving its performance in electronic devices. In particular, the presence of structural disorder and phase segregation within the PEDOT:PSS matrix plays a central role in determining the mechanisms governing charge transport, which will be discussed in the following sections.

4.5 Charge Transport Models in PEDOT:PSS

The electrical transport properties of conducting polymers are strongly influenced by structural disorder and the resulting localization of electronic states. As discussed in the previous sections, the absence of long-range crystalline order prevents carriers from moving through extended band states. Instead, charge transport occurs through thermally activated processes between localized sites. Several theoretical models have been proposed to describe these mechanisms in disordered polymer systems. Among them, the variable-range hopping (VRH) model and the fluctuation-induced tunneling model are widely used to explain the temperature-dependent conductivity observed in materials such as PEDOT:PSS. In addition, when the level of order increases or when carrier densities become sufficiently high, transport behavior may resemble that of disordered metals, which provides a useful framework for understanding the conductivity of substrates such as ITO.

4.5.1 Mott's Variable Range Hopping (VRH) Model

When an electric field is applied across a material, either parallel or perpendicular to the film plane, charge carriers drift toward the electrodes, enabling measurement of conductivity or resistivity. Despite relatively high room-temperature conductivity, conducting polymers do not behave as conventional metals. Experimentally, their conductivity generally does not increase upon cooling. This behavior arises because electronic transport in these polymers is dominated by disorder, which promotes carrier localization, particularly at low temperatures. For most conducting polymers, including PEDOT:PSS, localization persists across all practically accessible temperatures. The temperature dependence of conductivity therefore provides critical insight into the underlying transport mechanism. To describe electron conduction in amorphous systems, Sir Nevill Francis Mott introduced the VRH model, which has proven highly applicable to conducting polymers [30].

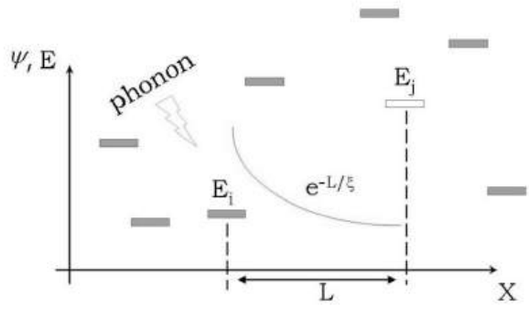

Figure 4.5. Charge carrier hopping between localized states. An electron moves from a site with energy E_i to an empty site with energy E_j via phonon-assisted activation. The factor $e^{-L/\xi}$ represents tunneling decay, where L is the hopping distance and ξ the localization length. The optimal hopping distance decreases with increasing temperature, characteristic of VRH transport [30].

In the VRH framework, charge carriers move between localized electronic states that differ in energy. Consider two localized sites separated by a distance *L*, in Figure 4.5 with energies *Ei* and *Ej* such that *ΔEij = Ej – Ei>0.* An electron can do transition between these sites through phonon absorption. Two factors govern the hopping probability: (i) the tunneling factor *exp*(-L/ξ), where ξ is the localization length and L is the hopping distance. (ii) the thermal activation (Boltzmann) factor *exp(-ΔE/kBT).* Following Mott, the hopping probability is expressed as [30]:

$$P_{ij} \propto exp\left(\frac{-2L}{\xi} - \frac{\Delta E_{ij}}{K_B T}\right) \qquad (4.2)$$

A key element of VRH theory is the relationship between hopping distance and energy difference via the density of states at the Fermi level:

$$L^n \Delta E N(E_F) \sim 1 \qquad (4.3)$$

where n denotes system dimensionality. This condition implies that an accessible state must exist within a volume L^n and energy interval ΔE to enable percolative transport. At low temperatures, thermal activation becomes limited. To minimize ΔE, carriers hop longer distances to energetically closer states rather than to nearest neighbors. Optimizing the hopping probability yields the conductivity expression:

$$\sigma_{VRH}(T) = \sigma_0 exp\left[-\left(\frac{T_0}{T}\right)^{\frac{1}{n+1}}\right] \qquad (4.4)$$

The characteristic overall conductivity $T_0 (= \beta / N(E_F)\xi^3 K_B)$ depends on both the localization length ξ and the density of states at the Fermi level $N(E_F)$. In conducting polymers such as PEDOT:PSS, charge carriers are typically associated with quasiparticles such as polarons or bipolarons that extend over several monomer units. For $n = 3$, the model corresponds to three-dimensional hopping between localized sites. Lower values of n may indicate anisotropic transport pathways or structural ordering within the polymer matrix. However, interpreting the dimensionality parameter requires caution. A value $n = 1$ of may also arise from electron-electron Coulomb interactions at low temperatures or from alternative mechanisms such as tunneling between conductive domains [30].

4.5.2 Fluctuation-Induced Tunneling Model

Although the VRH model successfully describes transport in strongly disordered polymers, it does not fully account for the relatively high conductivities observed in some conducting polymer systems. For example, highly doped materials such as polyacetylene, polyaniline, and PEDOT can exhibit conductivities exceeding 10 S/cm, suggesting the presence of additional transport mechanisms [31-35]. To address this limitation, Sheng proposed the fluctuation-induced tunneling model, which was originally developed to describe charge transport in granular metals embedded within insulating matrices. In this model, the material is viewed as a network of conducting regions separated by thin insulating barriers. Figure 4.6 shows the difference between the hopping and tunneling mechanisms.

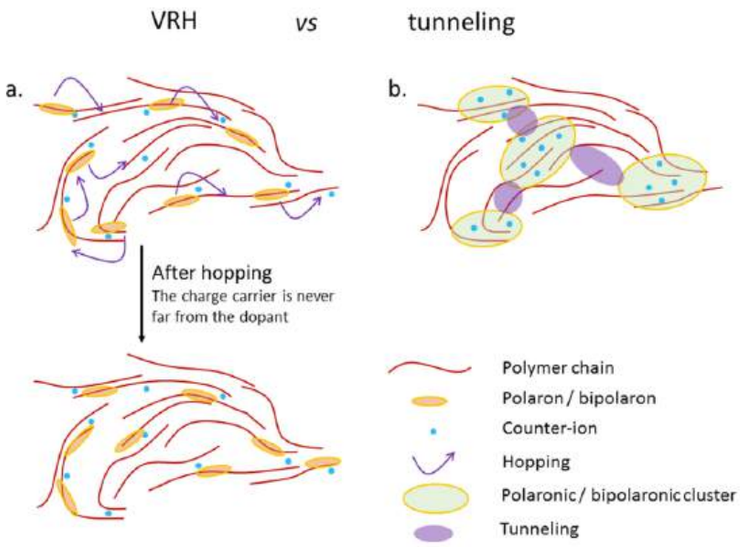

Figure 4.6. Comparison of charge transport mechanisms in conducting polymers: (a) variable-range hopping (VRH) between localized states and (b) tunneling between conductive polaronic clusters. Structural disorder leads to localization of charge carriers and determines the dominant transport pathway [3].

In contrast to the VRH mechanism, where carriers hop between localized states, the fluctuation-induced tunneling model assumes that charge transport occurs between neighboring conductive segments through thermally assisted tunneling. Thermal fluctuations can modify the potential barrier between adjacent segments, allowing electrons to tunnel from one region to another. The conductivity in this model is described by [3]:

$$\sigma_{Sheng}(T) = \sigma_0 exp\left(-\frac{T_1}{T + T_2}\right) \qquad (4.5)$$

where σ_0 is a constant prefactor, while T_1 and T_2 are characteristic temperatures related to the height and width of the tunneling barriers. In 1994, Zuppiroli and co-workers further developed the concept of fluctuation-induced tunneling by proposing a structural arrangement of charge carriers capable of supporting this transport mechanism between highly conductive regions [36]. Through theoretical calculations and measurements of temperature-dependent conductivity, they demonstrated that charge transport in conducting polymers cannot be explained solely by hopping between individual polarons or bipolarons along polymer chains. Instead, the material can contain polaronic clusters distributed throughout the polymer matrix. Within this framework, charge transfer occurs between highly doped clusters separated by regions of lower conductivity, in a manner consistent with the mechanism originally proposed by Sheng. At very low temperatures (T = 0 K), charge carriers remain localized near the dopant ions that generate them. As the temperature increases, transport becomes possible through thermally activated processes that involve both the formation of excited states, corresponding to the creation of an additional electron in one cluster and a hole in another, and charge transfer between clusters. This transfer can occur through tunneling processes, as illustrated in Figure 4.6. The resulting transport behavior is well described by the fluctuation-induced tunneling model given in Eq. (4.4). It should be noted that the term “tunneling” in this context does not strictly refer to quantum tunneling through a vacuum barrier; rather, it describes charge transfer between neighboring conductive clusters within the polymer matrix.

4.5.3 Transport in Disordered Metals and ITO

As synthesis and processing techniques for conducting polymers have improved, more ordered films have been produced, and some materials exhibit transport properties approaching metallic behavior. In such cases, the conductivity may remain finite at very low temperatures and show only weak temperature dependence. Similar behavior has been observed in amorphous alloys and highly disordered metals, where the electrical conductivity can deviate significantly from that of crystalline metals. These systems are often described within the framework of the metal-insulator transition, in which the electronic states evolve from localized to extended as the degree of disorder decreases. For disordered metals, the temperature dependence of conductivity can be expressed as [37,38]:

$$\sigma(T) = \sigma_0 + mT^{1/2} + BT^{p/2} \qquad (4.6)$$

Where σ_0 represents the residual conductivity at zero temperature. The second term accounts for electron-electron interaction effects, while the third term represents corrections associated with localization phenomena. In certain anisotropic systems, charge transport may instead resemble that of quasi-one-dimensional metals. In such cases the conductivity can be described by:

$$\sigma(T) = \sigma_m \exp\left(-\frac{T_m}{T}\right) \qquad (4.7)$$

where σ_m is a constant parameter and T_m corresponds to the energy associated with phonon-induced backscattering processes. These models are particularly relevant when considering ITO substrates, which are commonly used as transparent conductive electrodes in organic electronic devices. Because PEDOT:PSS films are often deposited on ITO surfaces, understanding the transport behavior of this substrate provides a useful reference for interpreting experimental conductivity measurements.

4.5.4 Numerical simulations and parameter sensitivity analysis

To further investigate the physical significance of the transport parameters extracted from the experimental conductivity measurements, numerical simulations were performed using the theoretical models discussed in the previous sections. The simulations were carried out by systematically varying the fitting parameters associated with the VRH, fluctuation-induced tunneling, and disorder-induced metallic transport models. This parameter sensitivity analysis provides additional insight into the influence of localization, tunneling barriers, and disorder-related metallic corrections on the electrical conductivity of PEDOT:PSS thin films deposited on glass and ITO substrates.

4.5.4.1 VRH Model Numerical Simulation of PEDOT:PSS Thin Films on Glass Substrates

To further investigate the influence of transport parameters on the electrical behavior of PEDOT:PSS films deposited on glass substrates, numerical simulations based on the variable-range hopping (VRH) model were performed. Figure 4.7 shows the effect of varying the characteristic temperature (T_0) on the electrical conductivity. The simulations show that the conductivity

decreases with increasing (T_0), indicating enhanced carrier localization and reduced hopping probability between localized states. Figure 4.7 presents the influence of the dimensionality parameter (n) on the conductivity behavior. As (n) decreases, the conductivity increases, suggesting the formation of more favorable charge transport pathways within the polymer matrix. In all cases, the conductivity curves become relatively similar at higher temperatures, indicating weaker temperature dependence above 100 K. Figure 4.7.shows umerical simulations of the VRH model for PEDOT:PSS films deposited on glass substrates with different values of T_0, using σ_0 = 45 S/cm and n = 0.5. Figure 4.8 shows numerical simulations of the VRH model for PEDOT:PSS films deposited on glass substrates with different values of the dimensionality parameter (n), using σ_0 = 45 S/cm and T_0 = 50 K.

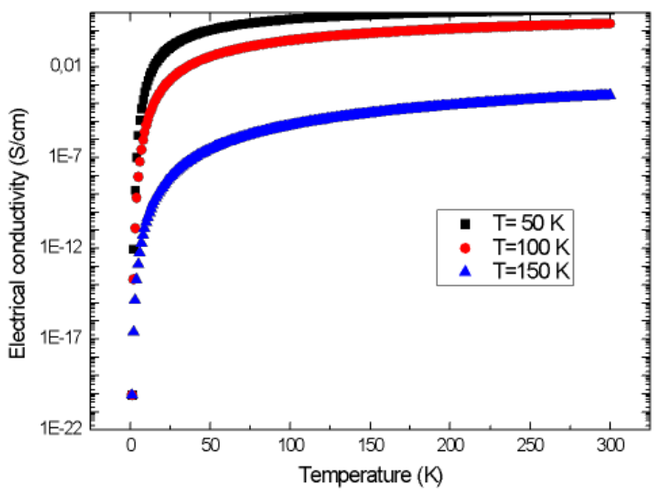

Figure 4.7. Numerical simulations of the variable-range hopping (VRH) model for PEDOT:PSS films deposited on glass substrates with different values of T_0, using σ_0 = 45 S/cm and n = 0.5.

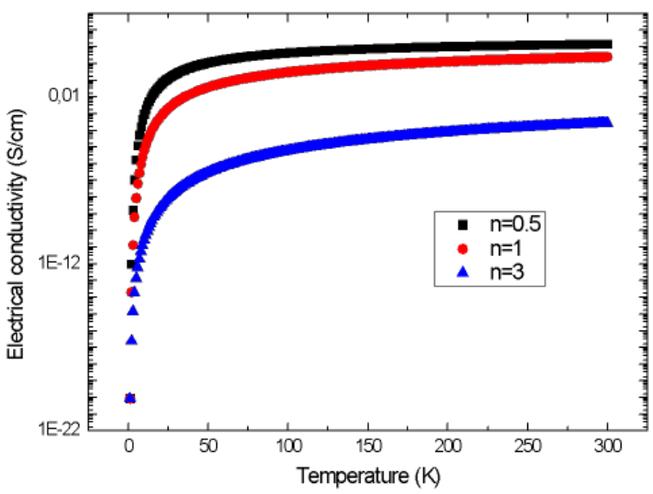

Figure 4.8. Numerical simulations of the VRH model for PEDOT:PSS film deposited on glass substrates with different values of the dimensionality parameter (n), using σ_0 = 45 S/cm and T_0 = 50 K.

4.5.4.2 Tunneling Model Numerical Simulation of PEDOT:PSS Thin Films on Glass Substrates

To further investigate the fluctuation-induced tunneling transport mechanism in PEDOT:PSS films deposited on glass substrates, numerical simulations were performed by varying the tunneling parameters T_1 and T_2. Figure 4.9 shows the effect of varying the parameter T_1 on the electrical conductivity. The simulations demonstrate that the conductivity decreases with increasing T_1. This

behavior indicates that larger tunneling barriers reduce the probability of charge transfer between neighboring conductive domains, particularly at low temperatures where thermal activation is limited.

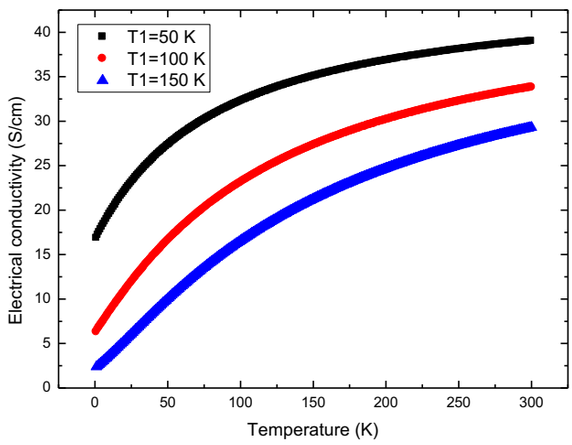

Figure 4.9. Numerical simulations of the fluctuation-induced tunneling model for PEDOT:PSS film deposited on glass substrates with different values of T_1, using σ_0 = 45 S/cm and T_2 = 50 K.

Figure 4.10 presents numerical simulations of the fluctuation-induced tunneling model with different values of T_2. The results show that the electrical conductivity increases with increasing T_2. This behavior suggests that increasing T_2 reduces the effective temperature dependence of the tunneling barrier, thereby facilitating charge transport between conductive regions within the polymer matrix.

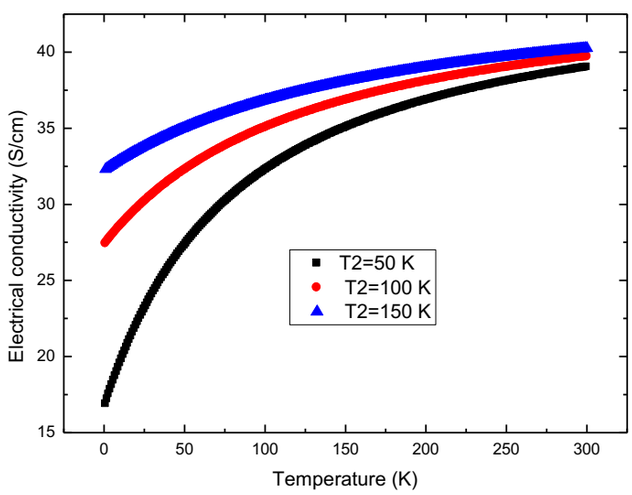

Figure 4.10. Numerical simulations of the fluctuation-induced tunneling model for PEDOT:PSS film deposited on glass substrates with different values of T_2, using σ_0= 45 S/cm and T_1= 50 K.

4.5.4.3 Disordered Metallic Transport Model Numerical Simulation of PEDOT:PSS Thin Films on ITO Substrates

To analyze the transport behavior of PEDOT:PSS film deposited on ITO substrates, numerical simulations based on the disorder-induced metallic transport model were performed. Figure 4.11 illustrates the effect of varying the parameter m on the electrical conductivity. The simulations show that metallic-like behavior appears more rapidly for lower values of m. These results indicate

that the onset of metallic transport is not determined solely by the absolute conductivity value but is strongly influenced by the transport parameter (m), which governs the temperature dependence of the conductivity.

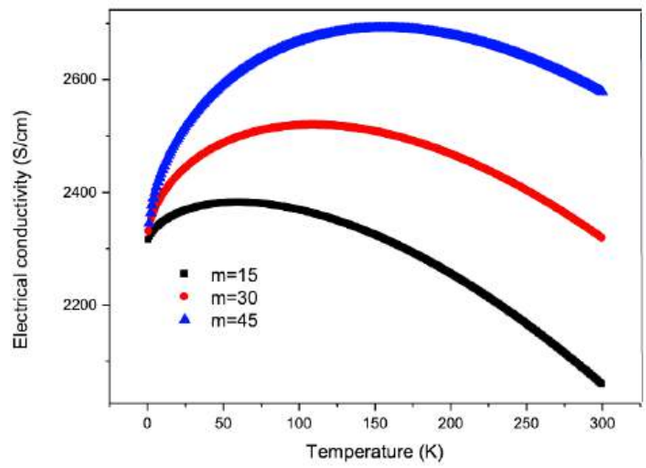

Figure 4.11. Numerical simulations of the disorder-induced metallic transport model for PEDOT:PSS film deposited on ITO substrates with different values of (m), using (σ_0 = 2300) S/cm, (p = 3.3), and (B = -0.04).

Figure 4.12 shows the influence of the parameter (B) on the conductivity behavior of PEDOT:PSS film deposited on ITO substrates. The simulations demonstrate that the temperature dependence of conductivity becomes stronger for lower values of (B). In particular, the conductivity decreases more rapidly with temperature, indicating that the parameter (B) plays an important role in describing disorder-related corrections to metallic transport.

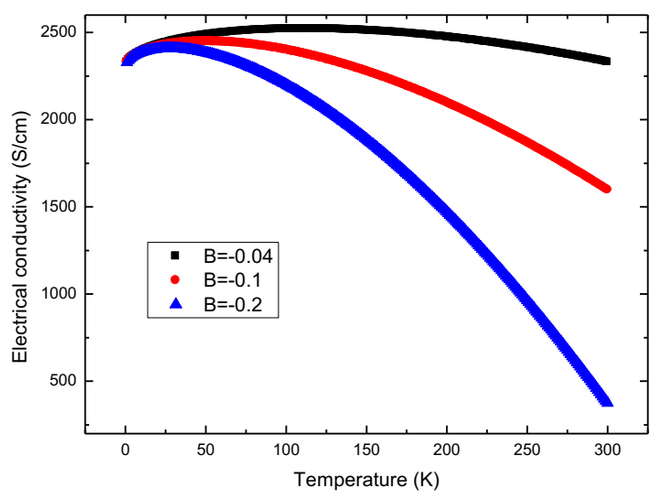

Figure 4.12. Numerical simulations of the disorder-induced metallic transport model for PEDOT:PSS film deposited on ITO substrates with different values of (B), using σ_0= 2300) S/cm, (p = 3.3), and (m = 30).

Figure 4.13 presents numerical simulations of the disorder-induced metallic transport model with different values of the parameter (p). The results show that the steepness of the conductivity decrease strongly depends on the value of (p). Larger values of (p) produce a stronger temperature dependence and more pronounced metallic-like behavior.

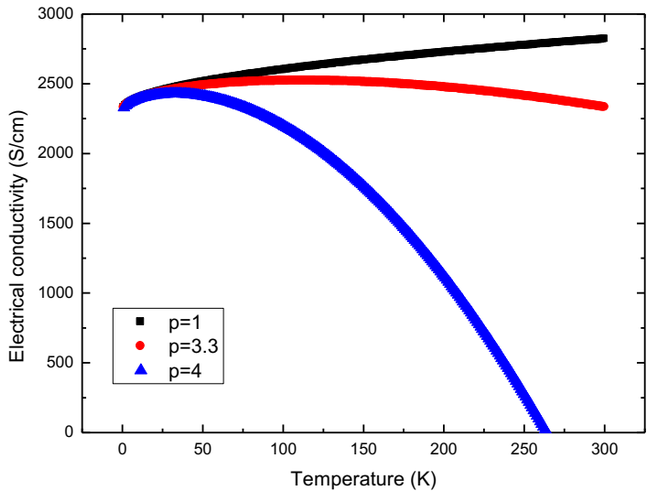

Figure 4.13. Numerical simulations of the disorder-induced metallic transport model for PEDOT:PSS film deposited on ITO substrates with different values of (p).

4.6 Conclusion

This chapter examined the fundamental mechanisms governing charge transport in the conducting polymer PEDOT:PSS. Due to the intrinsic structural disorder and heterogeneous morphology of conducting polymers, electronic transport in these materials cannot be adequately described by conventional band theory. Instead, charge carriers are localized and move through thermally activated processes between localized states. The discussion first addressed charge transport in disordered conducting polymers and highlighted the role of molecular structure, chain stacking, and anisotropic transport pathways in determining electrical behavior. The temperature dependence of conductivity was then presented as a key experimental parameter for identifying transport regimes. Two principal theoretical models were considered to describe charge transport in PEDOT:PSS. The Mott variable-range hopping (VRH) model accounts for thermally activated hopping of charge carriers between localized states in highly disordered systems. In contrast, the fluctuation-induced tunneling model describes transport between conductive regions separated by less conductive barriers, which becomes relevant in materials exhibiting higher conductivity or partial structural ordering. Transport behavior in disordered metallic systems was briefly discussed to provide a reference framework for the indium tin oxide (ITO) substrates used in this study. Together, these models provide a theoretical basis for interpreting the electrical transport behavior of PEDOT:PSS films and form the foundation for the analysis of experimental results presented in the following chapters.

4.7 References

[1] A. Elschner, S. Kirchmeyer, W. Lövenich, U. Merker, and K. Reuter, PEDOT: Principles and Applications of an Intrinsically Conductive Polymer. Boca Raton, FL, USA: CRC Press, 2011.

[2] N. Tessler, Y. Preezant, N. Rappaport, and Y. Roichman, “Charge transport in disordered organic materials and its relevance to thin-film devices: A tutorial review,” *Adv. Mater*., **21**, 2741–2761, (2009).

[3] R. Noriega, J. Rivnay, K. Vandewal, F. P. V. Koch, N. Stingelin, and P. Smith, “A general relationship between disorder, aggregation and charge transport in conjugated polymers,” *Nat. Mater*., **12**, 1038–1044, (2013).

[4] S. N. Patel and M. L. Chabinyc, “Anisotropies and the thermoelectric properties of semiconducting polymers,” *J. Appl. Polym. Sci*., **134**, 44403, (2017).

[5] V. Coropceanu, J. Cornil, D. A. da Silva Filho, Y. Olivier, R. Silbey, and J.-L. Brédas, “Charge transport in organic semiconductors,” *Chem. Rev*., **107**, 926–952, (2007).

[6] P. W. Anderson, “Absence of diffusion in certain random lattices,” *Phys. Rev*., **109**, 1492–1505, (1958).

[7] W. Böhm, T. Fritz, and K. Leo, “Charge transport in thin organic semiconducting films: Seebeck and field-effect studies,” *Phys. Status Solidi A*, **160**, 81–87, (1997).

[8] A. B. Kaiser, “Electronic transport properties of conducting polymers and carbon nanotubes,” *Rep. Prog. Phys*., **64**, 1–49, (2001).

[9] S. Ihnatsenka, X. Crispin, and I. V. Zozoulenko, “Understanding hopping transport and thermoelectric properties of conducting polymers,” *Phys. Rev. B*, 92, 035201, (2015).

[10] A. L. Efros and B. I. Shklovskii, “Coulomb gap and low temperature conductivity of disordered systems,” *J. Phys. C: Solid State Phys*., **8**, L49–L51, (1975).

[11] A. L. Efros and B. I. Shklovskii, “Influence of electron–electron interaction on hopping conduction of disordered systems,” *J. Non-Cryst. Solids*, **97**, 31–38, (1987).

[12] P. Sheng, B. Abeles, and Y. Arie, “Hopping conductivity in granular metals,” *Phys. Rev. Lett*., **31**, 44–47, (1973).

[13] W. Wei, H. Wang, and Y. H. Hu, “A review on PEDOT-based counter electrodes for dye-sensitized solar cells,” *Int. J. Energy Res*., **38**, 1099–1111, (2014).

[14] F. Jonas and J. T. Morrison, “3,4-Polyethylenedioxythiophene (PEDT): Conductive coatings, technical applications and properties,” *Synth. Met*., **85**, 1397–1398, (1997).

[15] L. Groenendaal, F. Jonas, D. Freitag, H. Pielartzik, and J. R. Reynolds, “Poly(3,4-ethylenedioxythiophene) and its derivatives: Past, present, and future,” *Adv. Mater*., **12**, 481–494, (2000).

[16] Y. Wen and J. Xu, “Scientific importance of water-processable PEDOT:PSS and preparation, challenge and new application in sensors of its film electrode: A review,” *J. Polym. Sci. Part A: Polym. Chem*., **55**, 1121–1150, (2017).

[17] C. Chen, “PEDOT-based counter electrodes for dye-sensitized solar cells: Rigid, flexible and indoor light applications,” *Mater. Chem. Front*., **8**, 3317–3335, (2024).

[18] J. Ouyang, “Secondary doping methods to significantly enhance the conductivity of PEDOT:PSS for its application as transparent electrode of optoelectronic devices,” *Displays*, **34**, 423–436, (2013).

[19] Y. Li, Y. Du, Y. Dou, K. Cai, and J. Xu, “PEDOT-based thermoelectric nanocomposites: A mini-review,” *Synth. Met*., **226**, 119–128, (2017).

[20] M. Nikolou and G. G. Malliaras, “Applications of PEDOT:PSS transistors in chemical and biological sensors,” *Chem. Rec*., **8**, 13–22, (2008).

[21] Y. Hui, C. Bian, S. Xia, J. Tong, and J. Wang, “Synthesis and electrochemical sensing application of PEDOT-based materials: A review,” *Anal. Chim. Acta*, **1022**, 1–19, (2018).

[22] J. Ouyang, “Recent advances of intrinsically conductive polymers,” *Acta Phys.-Chim. Sin.*, **34**, 1211–1220, (2018).

[23] G. Greczynski, T. Kugler, M. Keil, W. Osikowicz, M. Fahlman, and W. R. Salaneck, “Photoelectron spectroscopy of thin films of PEDOT:PSS conjugated polymer blend*,” J. Electron Spectrosc. Relat. Phenom.*, **121**, 1–17, (2001).

[24] S. Kirchmeyer and K. Reuter, “Scientific importance, properties and growing applications of poly(3,4-ethylenedioxythiophene),” *J. Mater. Chem.*, **15**, 2077–2088, (2005).

[25] F. Jonas, G. Heywang, and W. Schmidtberg, “Feststoffelektrolyte und diese enthaltende Elektrolytkondensatoren,” German Patent DE 3814730 A1, (1988).

[26] G. Heywang, F. Jonas, J. Heinze, and M. Dietrich, “Neue Polythiophene, Verfahren zu ihrer Herstellung und ihre Verwendung,” German Patent DE 3843412 A1, 1988.

[27] M. N. Gueye, A. Carella, N. Massonnet, E. Yvenou, S. Brenet, and J. Faure-Vincent, “Structure and dopant engineering in PEDOT thin films,” *Chem. Mater.*, **28**, 3462–3468, (2016).

[28] B. Cho, K. S. Park, J. Baek, H. S. Oh, Y.-E. K. Lee, and M. M. Sung, “Single-crystal poly(3,4-ethylenedioxythiophene) nanowires with ultrahigh conductivity,” *Nano Lett.*, **14**, 3321–3327, (2014).

[29] X. Wang, X. Zhang, L. Sun, D. Lee, S. Lee, and M. Wang, “High electrical conductivity and carrier mobility in oCVD PEDOT thin films,” *Sci. Adv.*, 4, (2018).

[30] A. M. Nardes, “On the conductivity of PEDOT:PSS thin films,” Ph.D. dissertation, Technische Universiteit Eindhoven, Eindhoven, The Netherlands, 2007.

[31] R. Menon, C. O. Yoon, D. Moses, A. J. Heeger, and Y. Cao, “Transport in polyaniline near the metal–insulator transition,” *Phys. Rev. B*, **48**, 17685–17694, (1993).

[32] T. Ishiguro, H. Kaneko, Y. Nogami, H. Ishimoto, H. Nishiyama, and J. Tsukamoto, “Logarithmic temperature dependence of resistivity,” *Phys. Rev. Lett.*, **69**, 660–663, (1992).

[33] K. Lee, S. Cho, S. H. Park, A. J. Heeger, C.-W. Lee, and S.-H. Lee, “Metallic transport in polyaniline,” *Nature*, **441**, 65–68, (2006).

[34] N. Massonnet, A. Carella, A. de Geyer, J. Faure-Vincent, and J.-P. Simonato, “Metallic behaviour of acid doped highly conductive polymers,” *Chem. Sci.*, **6**, 412–417, (2015).

[35] D. Farka, H. Coskun, J. Gasiorowski, C. Cobet, K. Hingerl, and L. M. Uiberlacker, “Anderson localization and the Mott–Ioffe–Regel limit in PEDOT,” *Adv. Electron. Mater.*, **3**, 1700050, (2017).

[36] L. Zuppiroli, M. N. Bussac, S. Paschen, O. Chauvet, and L. Forró, “Hopping in disordered conducting polymers,” *Phys. Rev. B*, **50**, 5196–5203, (1994).

[37] S. Kivelson and A. J. Heeger, “Intrinsic conductivity of conducting polymers,” *Synth. Met.*, **22**, 371–384, (1988).

[38] M. Ahlskog, R. Menon, A. J. Heeger, T. Noguchi, and T. Ohnishi, “Electronic transport in poly(p-phenylenevinylene),” *Phys. Rev. B*, **53**, 15529–15537, (1996).

Chapter 5

Influence of Substrate and Thickness on the Electrical Transport Properties of PEDOT:PSS Thin Films

5.1 Introduction

As discussed in Chapter 4, charge transport in PEDOT:PSS is commonly described using models based on Mott variable-range hopping (VRH) and tunneling mechanisms. These models reflect the heterogeneous nature of the material, where conductive PEDOT-rich domains are embedded within an insulating PSS matrix, leading to carrier transport through localized states or via tunneling between conducting regions. However, the relative contribution of these mechanisms is highly sensitive to external and structural parameters. In thin-film configurations, factors such as substrate type, film thickness, and temperature play a crucial role in determining the electrical transport properties. The substrate can influence film morphology, interfacial charge transfer, and energy level alignment, while film thickness affects the connectivity of conductive pathways and the effective transport distance. Additionally, temperature-dependent measurements provide insight into the dominant conduction mechanisms by revealing the thermal activation behaviour of charge carriers.

The aim of this chapter is to systematically investigate the influence of substrate, film thickness, and temperature on the electrical conductivity of PEDOT:PSS thin films. Thin films were deposited on different substrates, including glass, ITO-coated glass, and GaAs:Si, with controlled variation in thickness. Electrical conductivity was measured over a broad temperature range using a closed-cycle cryostat system. Attention is given to the reproducibility of the measurements and to the analysis of charge transport mechanisms through model fitting. A particular originality of this work lies in the investigation of the commercial PEDOT:PSS formulation (FHC Solar), which is a ready-to-use polymer system that does not require the addition of secondary dopants to achieve high conductivity. While previous studies have reported different transport mechanisms depending on processing conditions and material modifications, the present study demonstrates that the tunneling model consistently provides the best description of charge transport in F HC Solar PEDOT:PSS films, irrespective of substrate type or thin-film thickness. This finding highlights the intrinsic transport characteristics of this specific polymer system and provides new insight into the universality of tunneling-dominated conduction in commercially optimized PEDOT:PSS formulations. Furthermore, this chapter evaluates the applicability of tunneling and hopping-based models under varying experimental conditions, with the objective of identifying the dominant transport mechanism in PEDOT:PSS thin films. The results provide a comprehensive understanding of how structural and external factors govern charge transport, offering insights relevant for optimizing the performance of PEDOT:PSS-based electronic and energy devices.

5.2 Reproducibility of Electrical Conductivity Measurements

To ensure the reliability of the electrical measurements, the reproducibility of sheet resistance and electrical conductivity was evaluated for PEDOT:PSS (F HC Solar) thin films deposited under identical conditions. Three samples were prepared using LbL deposition process on glass substrates ($5 \times 5\ mm^2$) with the same nominal thickness. All samples were measured under identical conditions with an applied current of 100 μA. The resulting sheet resistance and electrical

conductivity values are summarized in Table 5.1. Only minor variations were observed between samples, indicating good uniformity in film fabrication and measurement consistency. The relative standard deviation of the electrical conductivity was found to be below ~3%, further confirming the high reproducibility of the measurements. These results demonstrate that the fabrication and characterization procedures are reliable, allowing subsequent variations in conductivity to be attributed to controlled parameters such as substrate, thickness, and temperature.

Table 5.1. Checking reproducibility of sheet resistance and electrical conductivity for LbL deposited samples on glass substrates (5 × 5 mm^2).

Sample	Current (μA)	Thickness (nm)	R_sheet Mean (Ω)	Conductivity (S/cm)
1	100	160	145.69	429.55
2	100	160	149,24	418,76
3	100	160	145,11	430,69

5.3 Charge Transport Model Analysis

To investigate the charge transport behavior in PEDOT:PSS thin films deposited on glass and GaAs:Si substrates, two theoretical models were employed to fit the temperature-dependent electrical conductivity: the variable-rang hopping (VRH) model and the tunneling model. The hopping model describes thermally activated charge transport between localized states and is expressed as:

$$\sigma_{VRH}\,(T) = \sigma_0 \exp\left[-\left(\frac{T_0}{T}\right)^{\frac{1}{n+1}}\right] \qquad (5.1)$$

where σ_0 is a pre-exponential factor related to the overall conductivity, T_0 is a characteristic temperature associated with the degree of localization and activation energy, and n represents the dimensionality of the transport process. In contrast, the tunneling model describes charge transport via carrier tunneling between conducting regions separated by potential barriers. This behavior is given by:

$$\sigma_{Sheng}\,(T) = \sigma_0 \exp\left(-\frac{T_1}{T + T_2}\right) \qquad (5.2)$$

where σ_0 is a constant, and T_1 and T_2 are characteristic temperatures related to the tunneling process. Specifically, T_1 is associated with the barrier height and width, reflecting the energy required for tunneling, while T_2 accounts for temperature-assisted tunneling effects and reduces the temperature dependence at higher temperatures.

5.4 Results

5.4.1 Charge Transport Model Analysis: Tunneling vs Variable Range Hopping

Figure 5.1 presents the temperature-dependent electrical conductivity for sample 2 (PEDOT:PSS (FHC Solar), thickness 160 nm) deposited on a glass substrate (5 × 5 mm^2) and measured at an applied current of 900 μA. The experimental data were fitted using both the tunneling model and the VRH model. As observed, the electrical conductivity increases with increasing temperature,

indicating thermally assisted charge transport. The tunneling model provides an excellent agreement with the experimental data, yielding a coefficient of determination of $R^2 = 0.9998$. In contrast, the VRH model shows a noticeably poorer fit, with $R^2 = 0.9606$ particularly deviating at lower temperatures where it fails to accurately describe the transport behavior. Furthermore, the hopping exponent obtained from the VRH fitting was found to be $n = 0.65$. In conventional hopping transport models, characteristic exponents are associated with specific transport dimensionalities, such as three-dimensional Mott VRH (1/4), two-dimensional VRH (1/3), or Efros–Shklovskii hopping (1/2). The obtained value corresponds to $1/n \approx 1.65$, which does not match any standard hopping regime reported in the literature. This inconsistency indicates that the charge transport mechanism in PEDOT:PSS (FHC Solar) cannot be reliably described within the framework of conventional hopping conduction. As can be seen, the tunneling model fits the experimental data better than the VRH model, especially at very low temperatures and at temperatures above room temperature. In addition, the parameters obtained from the VRH fit are much less precise, suggesting that this model does not fully describe the charge transport mechanism, even though it gives a relatively high R^2 value of 0.9606. As a result, the VRH model fails to accurately reproduce the experimental conductivity behaviour, particularly at lower temperatures, leading to the poorer fitting agreement observed compared to the tunneling model. The superior agreement of the tunneling model indicates that charge transport in PEDOT:PSS thin films is dominated by carrier tunneling between localized conducting regions. Structurally, PEDOT:PSS consists of conductive PEDOT-rich domains dispersed within an insulating PSS matrix. These domains host charge carriers in the form of polarons and bipolarons. Due to the presence of insulating barriers between these domains, charge carriers are unable to move via band-like transport and instead propagate through tunneling between neighboring conductive regions.

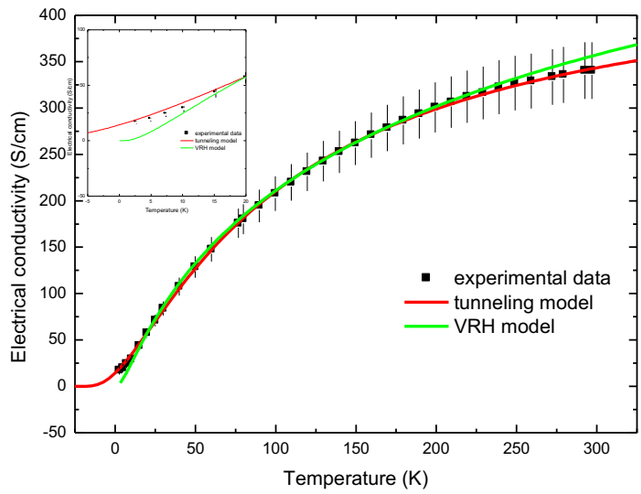

Figure 5.1. Electrical conductivity as a function of temperature for PEDOT:PSS (FHC Solar) sample 2, consisting of a 160 nm thick film deposited on a glass substrate (5 × 5 mm²) and measured at an applied current of 900 μA. The experimental data are compared with the tunneling and variable range hopping (VRH) transport models.

The tunneling process is governed by the parameters (T_1) and (T_2), which are associated with the characteristics of the potential barriers between conducting domains in the PEDOT:PSS films. Specifically, (T_1) reflects the effective barrier height and width, while (T_2) describes the contribution of temperature-assisted tunneling and determines the temperature dependence of the electrical conductivity. The values of (T_1) and (T_2) extracted from the fluctuation-induced tunneling

model for PEDOT:PSS (F HC Solar) thin films deposited on glass and doped GaAs:Si substrates are presented in Figure 5.2. A comparison of the two substrates shows that the (T_1) parameter remains nearly unchanged within the experimental uncertainty, indicating that the effective tunneling barrier characteristics are largely independent of the substrate. This suggests that the average barrier height and width between conducting regions in the PEDOT:PSS films are similar for films deposited on glass and GaAs:Si. In contrast, a noticeable difference is observed in the (T_2) parameter. Since (T_2) is associated with temperature-assisted tunneling processes, its variation indicates that the substrate influences the temperature dependence of charge transport. The differences in (T_2) may arise from substrate-induced modifications of the film morphology, polymer chain arrangement, or interfacial interactions, which affect the thermally activated component of charge transport without significantly altering the effective tunneling barrier itself. Furthermore, an analysis of these parameters as a function of film thickness reveals that neither (T_1) nor (T_2) exhibits a linear dependence on thickness. Instead, both parameters show a non-monotonic variation with increasing film thickness, indicating that the transport properties cannot be described by a simple thickness-scaling effect. This behavior suggests that charge transport is governed by complex morphological and structural changes within the PEDOT:PSS films, such as variations in domain connectivity, phase segregation, and inter-domain spacing, which evolve with film thickness and influence the tunneling process.

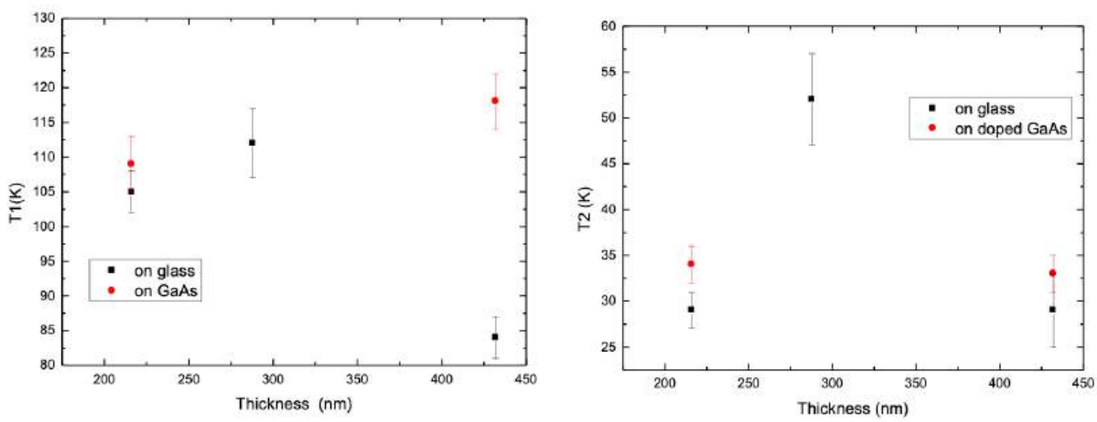

Figure 5.2. The thickness dependence of T_1 and T_2 for PEDOT:PSS (F HC Solar) thin films coated on glass substrate.

5.4.2 Thickness and Temperature dependence of the Electrical Conductivity

To further validate the dominance of the tunneling transport mechanism, additional temperature-dependent electrical conductivity measurements were performed on PEDOT:PSS (FHC Solar) thin films with varying thicknesses and deposited on different substrates. Figure 5.3 (a-d) presents representative results for films prepared on 5 × 5 mm^2 substrates. Figures 5.3 (a) and (b) correspond to samples deposited on glass substrates with thicknesses of 320 nm and 480 nm, respectively, while Figures 5.3 (c) and (d) show samples deposited on GaAs:Si substrates with thicknesses of 240 nm and 480 nm. In all cases, the electrical conductivity increases with increasing temperature, confirming the thermally assisted nature of charge transport in these films. The observed increase in electrical conductivity with temperature can be attributed to multiple factors. First, PEDOT:PSS behaves as a p-type semiconductor, and therefore its transport properties differ from those of metallic systems. In contrast to metals, where increasing temperature typically leads to enhanced scattering and reduced conductivity, the semiconducting nature of PEDOT:PSS results in improved charge transport at higher temperatures. This is because thermal energy increases the mobility of

charge carriers and promotes their excitation into conductive states, thereby enhancing overall conductivity. In addition, thermal effects may influence the microstructure of the material. As temperature increases, residual moisture within the film can be gradually removed, leading to structural rearrangements within the PSS-rich regions. This process can reduce insulating barriers between conductive PEDOT domains, facilitating more efficient charge transport. However, such effects are expected to become significant primarily at elevated temperatures, where moisture removal becomes more pronounced. While this thermally activated behaviour is well established for pristine PEDOT:PSS, its manifestation in modified or treated systems may vary. Changes in the electronic structure, such as alterations in energy levels or the effective band gap, could further influence the temperature dependence of conductivity by modifying the energy required for charge carrier transport. The experimental data were fitted using the tunneling model, which provides excellent agreement across all samples. The consistency of the fitting results across different thicknesses and substrate types demonstrates that the tunneling model accurately describes the charge transport behaviour in PEDOT:PSS thin films under a wide range of conditions. Despite variations in film thickness and substrate properties, no significant deviation from tunneling-dominated transport is observed. These findings indicate that, for PEDOT:PSS (FHC Solar), the charge transport mechanism is inherently governed by carrier tunneling between conductive PEDOT-rich domains. The robustness of this mechanism suggests that structural modifications such as thickness variation or substrate selection influence the magnitude of conductivity but do not alter the fundamental transport process. The results presented in Figure 5.3 provide strong evidence that tunneling is the dominant charge transport mechanism in PEDOT:PSS thin films, independent of substrate type and film thickness within the investigated range. The experimental uncertainty increased slightly with increasing temperature. However, these uncertainties remained small compared to the overall conductivity variation and did not affect the quality of the tunneling-model fit. Table 5.2 summarizes the fitting parameters obtained using the tunneling model for PEDOT:PSS (FHC Solar) thin films with different thicknesses and deposited on different substrates. The consistently high fitting quality demonstrates that the tunneling model accurately describes the temperature-dependent electrical conductivity for all investigated samples.

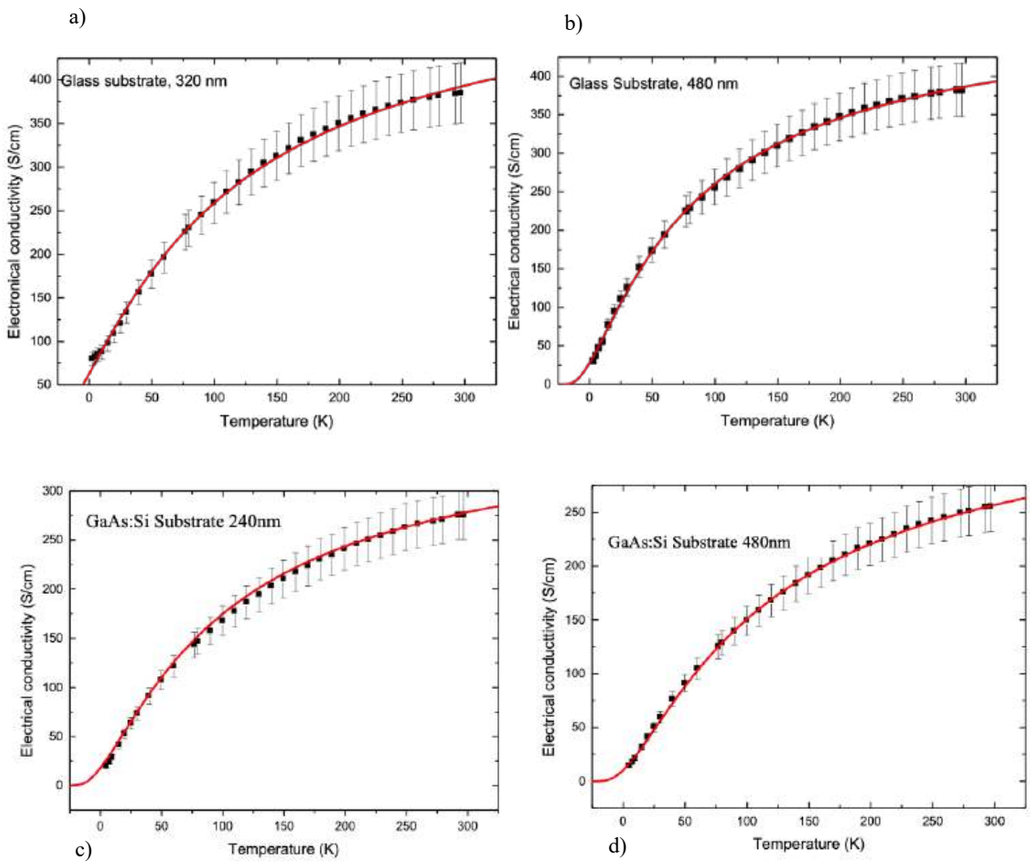

Figure 5.3. Temperature-dependent electrical conductivity of PEDOT:PSS (FHC Solar) thin films with different thicknesses and substrates: (a) glass substrate, 320 nm; (b) glass substrate, 480 nm; (c) GaAs:Si substrate, 240 nm; and (d) GaAs:Si substrate, 480 nm. The solid lines represent fits to the tunneling model. In all cases, the electrical conductivity increases with increasing temperature, and the tunneling model provides excellent agreement with the experimental data, suggesting tunneling-dominated charge transport independent of substrate type and film thickness within the investigated range.

Table 5.2. Fitting parameters obtained using the tunneling model applied to the temperature-dependent electrical conductivity of PEDOT:PSS (FHC Solar) thin films deposited on different substrates and with varying thicknesses.

Sample	Substrate	Thickness (nm)	σ_0 (S/cm)	T_1(K)	T_2 (K)	R^2
(a)	Glass	320	487.51	112.26	52.00	0.9986
(b)	Glass	480	449.30	84.23	29.35	0.9994
(c)	GaAs:Si	240	346.48	109.99	34.40	0.9995
(d)	GaAs:Si	480	328.14	117.00	33.00	0.9997

The fitting parameters obtained from the tunneling model are summarized in Table 5.2. In all cases, excellent agreement between the experimental data and the model was achieved, as evidenced by the high R^2 values (~0.999). The consistency of the fitting quality across all samples demonstrates that the tunneling model accurately describes the temperature-dependent electrical conductivity of PEDOT:PSS (FHC Solar) thin films, independent of substrate type and film thickness. Although variations in substrate and thickness influence the magnitude of the electrical conductivity, the fundamental transport mechanism remains unchanged. The σ_0 values are generally higher for films deposited on glass substrates compared to GaAs:Si substrates, suggesting that substrate-dependent effects such as film morphology, interfacial interactions, or conductive domain connectivity can affect the overall conductivity of the films. In addition, slight variations in σ_0 with thickness

indicate that the connectivity between PEDOT-rich conductive domains may be influenced by film thickness. The obtained T_1 values remain within a relatively narrow range for all investigated samples, indicating that the effective tunneling barriers governing charge transport are largely unaffected by changes in substrate or film thickness. Similarly, only minor variations are observed in the T_2 parameter, which may be associated with structural disorder, residual moisture, or variations in the insulating PSS-rich regions. The results presented in Table 5.2 strongly support the conclusion that charge transport in PEDOT:PSS (FHC Solar) is intrinsically dominated by carrier tunneling between conductive PEDOT-rich domains. While substrate selection and film thickness influence the absolute conductivity values, they do not alter the underlying transport mechanism within the investigated range.

5.4.3 Thickness Dependence of Surface Roughness and Sheet Resistance

To further investigate the influence of film thickness on the electrical and structural properties of PEDOT:PSS (FHC Solar) thin films, sheet resistance measurements were performed for samples deposited on both glass and GaAs:Si substrates with thicknesses of 240 nm, 320 nm, and 480 nm. In addition, surface roughness analysis was carried out for films deposited on glass substrates. The extracted values are summarized in Table 5.3. For both glass and GaAs:Si substrates, the sheet resistance decreases systematically with increasing film thickness. This trend is attributed to improved connectivity between conductive PEDOT-rich domains, which enhances charge transport pathways and reduces the overall resistance of the films. For the glass substrates, the root-mean-square (RMS) surface roughness (S_q) and mean roughness (S_a) are observed to decrease with increasing film thickness. Thinner films exhibit higher roughness, which can be associated with incomplete surface coverage and structural inhomogeneities. As the thickness increases, the films become more uniform and continuous, resulting in smoother surfaces and reduced roughness values. Surface roughness measurements were not performed for the GaAs:Si samples; therefore, no direct comparison of morphological evolution between the two substrate types can be made. However, the consistent decrease in sheet resistance with increasing thickness across both substrates indicates that thickness plays a dominant role in improving electrical performance, regardless of the substrate. The reduction in surface roughness observed for the glass substrates suggests that improved film uniformity contributes to enhanced electrical conduction. A smoother morphology is expected to promote better interdomain connectivity, facilitating more efficient charge transport between PEDOT-rich regions. Importantly, these results remain consistent with the transport analysis presented in section 5.4.2. While film thickness influences the magnitude of sheet resistance and surface morphology, it does not alter the fundamental charge transport mechanism. The tunneling process continues to govern charge transport in PEDOT:PSS thin films, with thickness primarily affecting the efficiency of carrier transport rather than the mechanism itself. Representative AFM surface images for the glass substrates (a) 240 nm, (b) 320 nm and (c) 480 nm are shown in Figure 5.4, confirming the trend of decreasing roughness with increasing film thickness.

Table 5.3. Sheet resistance of PEDOT:PSS (FHC Solar) thin films deposited on glass and GaAs:Si substrates as a function of film thickness, along with RMS surface roughness values for films deposited on glass substrates.

Thickness (nm)	R_s (Glass) (Ω)	R_s (GaAs:Si) (Ω)	S_q (nm) (Glass)	S_a (nm) (Glass)
240	144	160	4.4	3.1
320	90	147	3.8	2.8
480	60	90	2.6	2

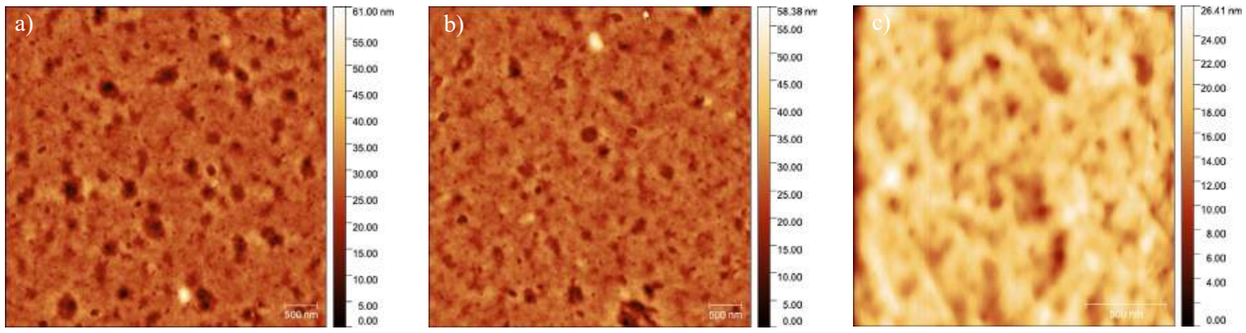

Figure 5.4. AFM surface topography images of PEDOT:PSS (FHC Solar) thin films deposited on glass substrates with thicknesses of (a) 240 nm, (b) 320 nm, and (c) 480 nm, illustrating the decrease in surface roughness with increasing film thickness.

5.4.4 Cross-Plane Electrical Characterization of PEDOT Thin Films

To further investigate the charge transport properties of PEDOT (FHC Solar), cross-plane electrical measurements were performed on the 480 nm thick film deposited on the GaAs substrate using the setup described in Chapter 3. The measured conductivity values are summarized in Table 5.4. The results show that the cross-plane electrical conductivity at room temperature is lower than the corresponding in-plane conductivity. This difference indicates that charge transport is more efficient parallel to the film surface than across its thickness. The lower cross-plane conductivity can be attributed to the microstructure of PEDOT, where conductive PEDOT-rich domains form preferentially interconnected pathways in the in-plane direction. In contrast, charge carriers moving in the cross-plane direction must traverse a larger number of domain boundaries and less conductive PSS-rich regions, resulting in higher transport resistance. Figure 5.5 shows the room-temperature current–voltage (I–V) characteristics of the 480 nm PEDOT:PSS film deposited on the GaAs:Si substrate measured in the cross-plane configuration. The I–V curve exhibits a linear relationship between current and voltage, indicating ohmic behaviour within the investigated voltage range. This linear response suggests the absence of significant injection barriers at the contacts and confirms that charge transport through the film remains governed by its bulk electrical properties.

Table 5.4. Cross-plane electrical conductivity of the 480 nm PEDOT (FHC Solar) thin film deposited on a GaAs substrate measured at different temperatures.

Temperature (K)	Reff (Ω)	R_s (GaAs:Si) (Ω)	R_s (PEDOT:PSS) (Ω)	PEDOT:PSS (S/cm)
0	124±19	12±2	7852±1000	0.25±0.023
25	115±17	11±2	7221±1500	0.27±0.023
50	100±15	11±2	6240±1300	0.32±0.023

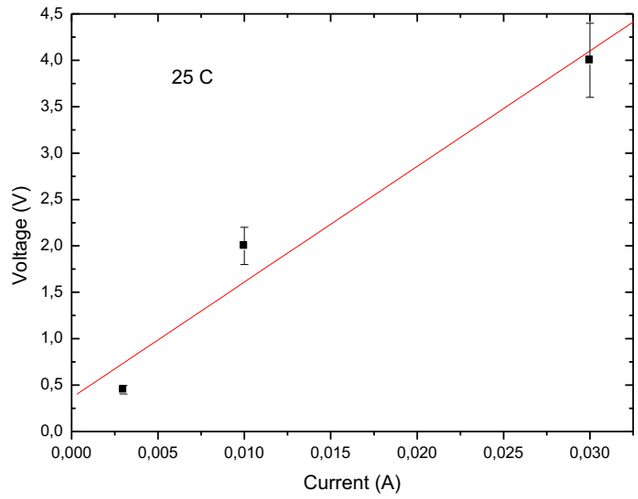

Figure 5.5. Room-temperature cross-plane current–voltage (I–V) characteristics of the 480 nm PEDOT:PSS (FHC Solar) thin film deposited on a GaAs:Si substrate, showing a linear ohmic response.

5.5 Electrical Transport in PEDOT:PSS Thin Films on ITO-Coated Glass Substrates

Figure 5.6 (a) shows the temperature dependence of sheet resistance for a PEDOT:PSS (FHC Solar) thin film with a thickness of 240 nm deposited on a 5 × 5 mm^2 ITO-coated glass substrate. In contrast to the samples deposited on insulating substrates, the sheet resistance increases with increasing temperature. Consequently, the electrical conductivity decreases with increasing temperature, indicating a semi-metallic transport behaviour. This behaviour originates from the underlying ITO layer, which exhibits metallic or semi-metallic characteristics and dominates the overall electrical response of the system. This enhancement is attributed to the high intrinsic conductivity of ITO, as well as possible improvements in charge transfer and structural ordering of PEDOT chains at the interface with the conductive substrate. The temperature-dependent effective electrical conductivity of the PEDOT:PSS/ITO system, representing the combined contribution of both layers, is shown in Figure 5.6 (b). To isolate the contribution of the PEDOT:PSS layer, the electrical conductivity of the bare ITO substrate was measured separately under identical conditions. Based on this, the conductivity data were normalized by subtracting the contribution of the ITO layer from the effective conductivity. The resulting normalized electrical conductivity is presented in Figure 5.6 (c). Compared to the effective conductivity shown in Figure 5.6 (b), the normalized data provide a clearer representation of the transport behaviour associated with the PEDOT:PSS layer. However, despite this correction, the temperature dependence still exhibits a decreasing trend with increasing temperature, indicating that the semi-metallic behaviour introduced by the ITO substrate is not eliminated. A comparison between Figures 5.6 (b) and 5.6 (c) demonstrates that the ITO layer plays a dominant role not only in enhancing the magnitude of the electrical conductivity but also in determining its temperature dependence. Finally, the intrinsic conductivity of the PEDOT:PSS layer, determined using the two-layer model described by Eq. (5.5), is presented in Figure 5.6 (d). While normalization reduces the direct contribution of the ITO layer, the overall transport behaviour remains influenced by the conductive substrate, suggesting strong coupling between the PEDOT:PSS film and the underlying ITO. Due to this semi-metallic behaviour, the temperature dependence of conductivity cannot be accurately described using hopping or tunneling models, which are typically applicable to disordered insulating systems.

Instead, the transport behaviour is better interpreted within the framework of disordered metallic systems. In such systems, the conductivity can be expressed as:

$$\sigma(T) = \sigma_0 + mT^{1/2} + BT^{p/2} \qquad (5.3)$$

where σ_0 represents the residual conductivity at low temperature, the $T^{1/2}$ term accounts for electron-electron interaction effects, and the final term describes corrections associated with localization phenomena.

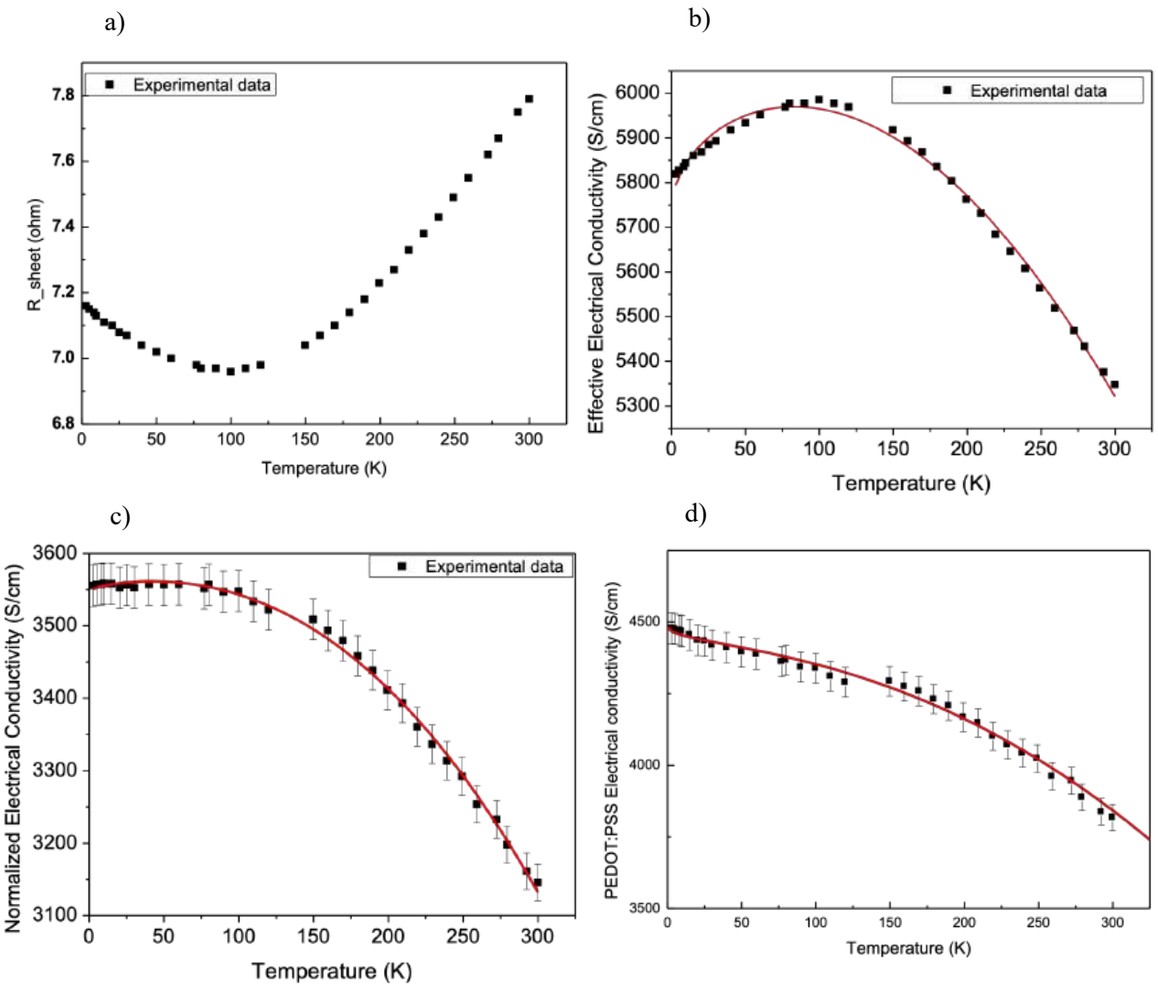

Figure 5.6. (a) Temperature dependence of sheet resistance for PEDOT:PSS (FHC Solar) thin film (240 nm) deposited on ITO-coated glass substrate (5 × 5 mm^2). (b) Effective electrical conductivity as a function of temperature, reflecting the combined contribution of PEDOT:PSS and the ITO layer. (c) Extracted (normalized) electrical conductivity of the PEDOT:PSS thin film after removing the contribution of the ITO substrate using the two-layer model. The decrease in conductivity with increasing temperature indicates semi-metallic behaviour dominated by the ITO layer.

The fitting parameters obtained from the disordered metallic transport model are summarized in Table 5.5. In both the effective and normalized conductivity data, the model provides good agreement with the experimental results, confirming that the transport behaviour is characteristic of a semi-metallic or disordered metallic system rather than thermally activated hopping or tunneling transport. Although normalization significantly reduces the magnitude of the conductivity by partially removing the contribution of the ITO layer, the temperature dependence remains qualitatively unchanged. In both cases, the conductivity decreases with increasing temperature, indicating that the metallic contribution of the conductive substrate continues to dominate the transport behaviour. The persistence of semi-metallic behaviour after normalization suggests that the interaction between the PEDOT:PSS film and the ITO substrate extend beyond a

simple additive conductivity contribution. The conductive substrate likely modifies the interfacial electronic structure, charge carrier distribution, or ordering of PEDOT chains within the film, resulting in strong coupling between the two layers. Consequently, the electrical transport properties of PEDOT:PSS deposited on ITO-coated glass cannot be accurately described using hopping or tunneling models typically associated with disordered insulating systems. Instead, the observed behaviour is more consistent with quantum correction effects commonly observed in disordered metallic conductors.

Table 5.5. Fitting parameters obtained using the disordered metallic transport model applied to the effective and normalized electrical conductivity of PEDOT:PSS (FHC Solar) thin films deposited on ITO-coated glass substrates.

Condition	$\boldsymbol{\sigma_0}$ **(S/cm)**	$\boldsymbol{m}$	$\boldsymbol{B}$	$\boldsymbol{p}$	$\mathbf{R^2}$
Before normalization	5738.6	33.2	-0.011	3.98	0.994
After normalization	2189.3	32.36	-0.045	3.87	0.972
PEDOT:PSS Thin film	4482.3	-8.88	-0.0013	3.91	3.87

As shown in Table 5.5, normalization significantly reduces the residual conductivity σ_0, confirming that the ITO layer contributes strongly to the overall conductivity magnitude. However, the fitting parameters remain consistent with semi-metallic transport behaviour even after normalization. In particular, the conductivity continues to decrease with increasing temperature, indicating that the influence of the conductive ITO substrate is not completely removed. The lower R^2 value obtained after normalization further suggests that the transport behaviour of the PEDOT:PSS/ITO system cannot be fully separated into independent contributions from the two layers, supporting the presence of strong interfacial coupling between PEDOT:PSS and the ITO substrate.

5.5.1 Interfacial Effects of PEDOT:PSS on ITO and Their Influence on Electrical Transport

ITO is widely used as a transparent conductive electrode in organic electronic devices such as organic photovoltaics (OPVs) and organic light-emitting diodes (OLEDs). In these systems, PEDOT:PSS is typically deposited on top of the ITO layer, where it functions as a hole transport and injection layer. The incorporation of PEDOT:PSS plays a crucial role in modifying the interfacial electronic structure and improving charge transport across the electrode interface. Figure 5.7 illustrates representative device architectures for organic solar cells with different electrode

configurations, including ITO-only and ITO/PEDOT:PSS-based structures [1]. In such multilayer systems, the interface between ITO and PEDOT:PSS critically determines the efficiency of charge injection and extraction.

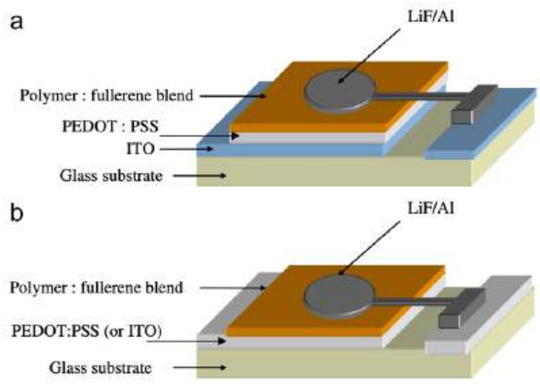

Figure 5.7. Representative device architectures for organic solar cells with different electrode configurations, including ITO-only and ITO/PEDOT:PSS-based structures [1].

A key factor governing the interfacial behaviour is the difference in work function between ITO and PEDOT:PSS. The work function represents the minimum energy required to remove an electron from the material to the vacuum level and plays a central role in determining energy level alignment at interfaces. Untreated ITO typically has a work function of approximately 4.7 eV, whereas PEDOT:PSS exhibits a higher work function of approximately 5.0 eV [2]. When PEDOT:PSS is deposited on ITO, this difference in work function leads to a modification of the interfacial energy alignment. Specifically, the higher work function of PEDOT:PSS effectively reduces the energy barrier for hole injection from the electrode into the adjacent organic layer. As a result, holes can be injected more efficiently, leading to improved charge transport and reduced operating voltage in devices such as OLEDs. Even small changes in the injection barrier can significantly affect device performance, as charge injection efficiency is highly sensitive to interfacial energetics. In addition to modifying the energy alignment, the PEDOT:PSS layer improves the physical and chemical quality of the interface. It forms a smoother and more uniform coating on the ITO surface, reducing surface roughness and minimizing localized defects. This leads to a more homogeneous electric field distribution and reduces charge trapping at the interface. Furthermore, PEDOT:PSS acts as a buffer layer that prevents direct contact between the ITO electrode and the active organic material, thereby suppressing degradation processes and enhancing device stability and lifetime [1, 2]. The combined effect of improved energy level alignment and enhanced interface quality results in more efficient charge injection and transport. This is consistent with previous studies showing that PEDOT:PSS-coated ITO electrodes exhibit improved electrical, optical, and mechanical properties, including reduced resistance, improved adhesion, and enhanced

structural stability [3, 4]. These interfacial effects are directly reflected in the experimental results obtained in this study. PEDOT:PSS thin films deposited on ITO-coated glass substrates exhibit significantly higher effective electrical conductivity compared to films deposited on insulating substrates. However, the temperature dependence of conductivity shows an opposite trend, with conductivity decreasing as temperature increases. This behaviour indicates a semi-metallic transport mechanism, which arises from the dominant contribution of the ITO layer. To isolate the intrinsic contribution of the PEDOT:PSS film, a two-layer model was used to extract the normalized conductivity by accounting for the conductivity of the underlying ITO layer.

5.5.2 Electrical conductivity of PEDOT:PSS thin films on ITO-coated substrates

However, it is important to note that the measured electrical conductivity in this configuration represents an effective conductivity (σ_{eff}) arising from the combined contribution of the PEDOT:PSS thin film and the underlying ITO layer. Therefore, a correction is required to extract the intrinsic conductivity of the PEDOT:PSS layer. The effective conductivity can be expressed as [5]:

$$\sigma_{eff} = \frac{\sigma_1 L_1 + \sigma_2 L_2}{L_1 + L_2} \qquad (5.4)$$

Where σ_1 (Intrinsic conductivity of the PEDOT:PSS layer) and L_1 are the conductivity and thickness of the PEDOT:PSS layer, and σ_2 and L_2 corresponded to the ITO layer. Rearranging eq. (5.4) allows the conductivity of the PEDOT:PSS thin films to be determined:

$$\sigma_1 = \frac{\sigma_{eff}(L_1 + L_2) - \sigma_2 L_2}{L_1} \qquad (5.5)$$

In this study, the PEDOT:PSS thin film was $L_1 = 240$ nm, while the ITO thickness was $L_2 = 150$ nm. The sheet resistance of the bare ITO substrate was measured to be 17 (Ω). Interestingly, the thinner PEDOT:PSS film (160 nm) exhibits a higher electrical conductivity compared to the thicker film (240 nm). Intrinsic conductivity of the PEDOT:PSS layer (σ_1) values were obtained using Eq. (5.5), considering the ITO sheet resistance of 17 Ω and a thickness of 150 nm. This indicates that the enhanced conductivity is not solely due to the contribution of the ITO substrate but is strongly influenced by interfacial effects. In thinner films, the influence of the PEDOT:PSS/ITO interface is more pronounced. The improved energy alignment, combined with

enhanced structural ordering of polymer chains near the interface, facilitates more efficient charge transport. As the film thickness increases, the relative contribution of the interface decreases, and the transport properties become increasingly dominated by the intrinsic morphology and disorder within the PEDOT:PSS layer. These results demonstrate that the PEDOT:PSS/ITO interface plays a critical role in determining the electrical transport properties of the system. The interplay between interfacial energetics, morphology, and substrate contribution must therefore be carefully considered when analysing charge transport in multilayer thin-film structures.

5.6 Effect of Additives on the Electrical Conductivity of PEDOT:PSS (3.4% Aqueous Dispersion)

In addition to the PEDOT:PSS (FHC Solar) system discussed in the previous sections, a commercially available PEDOT:PSS aqueous dispersion (3.4 wt% in water) was investigated to study its intrinsic electrical transport properties and the effect of metal salt incorporation. Copper (II) chloride ($CuCl_2$) was introduced as a potential dopant with the aim of enhancing electrical conductivity. The electrical properties of pristine PEDOT:PSS (3.4%) thin films were characterized using Hall measurements in the van der Pauw configuration. The sheet resistance was measured and used to determine the electrical conductivity, considering the film thickness. Temperature-dependent measurements were carried out using a closed-cycle cryostat over the range of 8 K to 300 K. To analyse the temperature dependence of electrical conductivity, the VRH and the Schaefer-Siebert-Roth (SSR) models were employed. In the Mott model, charge transport occurs via thermally activated hopping between localized states, and the electrical conductivity is given by Eq. 5.1. In contrast, the Schaefer-Siebert-Roth (SSR) model accounts for both localization length and conjugation length within the polymer chains. In this framework, doping modifies the polymer backbone by introducing charge carriers such as polarons and bipolarons, thereby affecting the conjugation length. The conductivity is expressed as:

$$\sigma = \sigma_0 exp\left[-\left(\frac{T}{T_0}\right)^{-\gamma}\right] \; where \; \frac{1}{4} < \gamma < \frac{1}{2} \qquad (5.6)$$

Where γ is related to the density of states near the Fermi level, and σ_0 and T_0 depend on the localization characteristics of the system. Figure 5.8 shows the temperature dependence of the electrical conductivity for PEDOT:PSS (3.4%) in the temperature range of 8 K to 200 K. The conductivity increases with increasing temperature, indicating thermally activated transport behavior typical of disordered conductive polymers. Both models provide a reasonable fit to the

experimental data; however, the SSR model demonstrates superior agreement, likely due to its consideration of both localization and conjugation effects within the polymer structure.

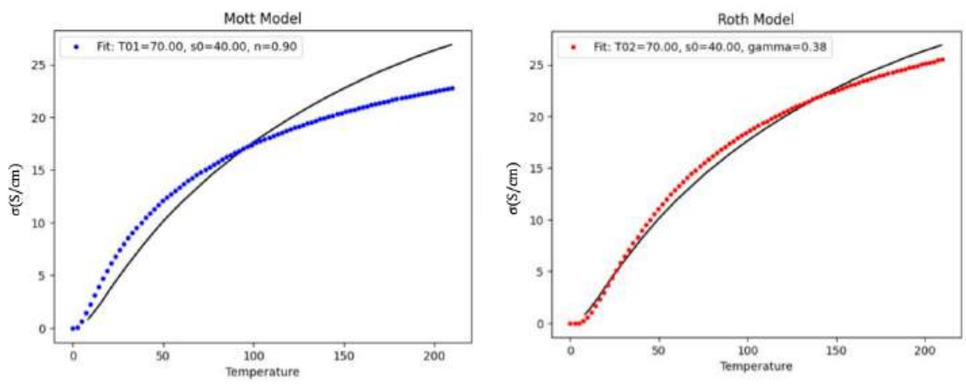

Figure 5.8. Temperature dependence of the electrical conductivity of PEDOT:PSS (3.4% aqueous dispersion) measured in the range of 8 K to 200 K. The experimental data are fitted using the Mott variable-range hopping (VRH) model and the Schaefer-Siebert-Roth (SSR) model, showing thermally activated transport behavior with improved agreement for the SSR model.

To investigate the effect of metal incorporation, $CuCl_2$ was added to the PEDOT:PSS solution. Contrary to expectations, the introduction of copper did not enhance the electrical conductivity. Instead, a reduction in current flow and overall conductivity was observed in the Cu-doped samples compared to pristine PEDOT:PSS. Several factors may contribute to this behavior. The addition of $CuCl_2$ resulted in poor homogeneity of the solution, likely due to limited solubility, polarity mismatch, or chemical incompatibility between the components. This may lead to phase separation or aggregation within the film, disrupting the conductive pathways. Furthermore, film processing challenges, such as degradation during cleaving or interaction with conductive silver paste, may have compromised the structural and electrical integrity of the doped films. These results highlight that the incorporation of metal salts into PEDOT:PSS does not necessarily lead to improved electrical performance. Instead, the effectiveness of doping strongly depends on the compatibility of the additive with the polymer matrix and its influence on film morphology and charge transport pathways.

5.7 Conclusion

This chapter systematically investigated the effects of substrate type, film thickness, temperature, and additive incorporation on the electrical transport properties of PEDOT:PSS thin films. Temperature-dependent conductivity measurements and transport model analysis showed that the tunneling model describes the experimental data significantly better than the variable-range hopping (VRH) model, indicating that charge transport is mainly governed by carrier tunneling

between conductive PEDOT-rich domains separated by insulating PSS regions. Reproducibility tests demonstrated good film uniformity and measurement reliability, with conductivity variations below 3%. For films deposited on glass and GaAs:Si substrates, conductivity increased with temperature, confirming thermally assisted transport behaviour. Increasing film thickness reduced sheet resistance and improved surface uniformity, as confirmed by AFM analysis, although the dominant transport mechanism remained unchanged.

In contrast, PEDOT:PSS films deposited on ITO-coated glass exhibited decreasing conductivity with increasing temperature, indicating semi-metallic behaviour strongly influenced by the conductive ITO layer and the PEDOT:PSS/ITO interface. The interaction with the ITO surface can modify the morphology and electronic structure of PEDOT:PSS near the interface. In particular, the conductive PEDOT chains may become more ordered and better aligned, while partial segregation of the insulating PSS phase away from the interface can enhance the connectivity between PEDOT-rich regions. These effects facilitate charge transport and reduce interfacial resistance, especially in thinner films where the substrate influence is stronger. As a result, thinner PEDOT:PSS films on ITO exhibited enhanced conductivity compared to thicker films. The results demonstrate that the electrical transport properties of PEDOT:PSS thin films are strongly influenced by morphology, substrate interactions, and interfacial effects, while tunneling remains the dominant transport mechanism on insulating substrates. These findings provide valuable insight for optimizing PEDOT:PSS materials in flexible electronics, thermoelectric devices, and organic optoelectronics.

5.8 References

[1] F. C. Krebs, J. Alstrup, H. Spanggaard, K. Larsen, and E. Kold, "Role of ITO and PEDOT:PSS in stability/degradation of polymer:fullerene bulk heterojunction solar cells," *Sol. Energy Mater. Sol. Cells*, **83**, 293–300, (2004).

[2] J. S. Kim, P. K. H. Ho, C. E. Murphy, and R. H. Friend, "Effect of annealing on the electrical properties and morphology of a conducting polymer used as an anode in organic light-emitting devices," *Macromolecules*, **37**, 2861–2867, (2004).

[3] R. A. Green, N. H. Lovell, G. G. Wallace, and L. A. Poole-Warren, "Characteristics of transparent, PEDOT:PSS-coated indium-tin-oxide (ITO) microelectrodes," *Electrochem. Commun*., **10**, 501–504, (2008).

[4] C.-H. Hsu, Y.-C. Chen, W.-H. Lin, and C.-P. Hsu, "Improving the performance of ITO thin films by coating PEDOT:PSS," J. Nanomater., **2014**, 1–7, (2014).

[5] Y.-Y. Chen and J.-Y. Juang, "Finite element analysis and equivalent parallel-resistance model for conductive multilayer thin films*," Meas. Sci. Technol*., **27**, (2016).

Chapter 6

Electron Contribution to Heat Propagation in PEDOT:PSS Thin Films

6.1 Introduction

Heat propagation in PEDOT:PSS thin films are governed by complex transport mechanisms involving both phonon-mediated and charge-carrier-assisted heat transport. In addition, the anisotropic morphology of PEDOT:PSS films can lead to significant differences between in-plane and cross-plane thermal transport. Understanding the relationship between electrical conductivity and thermal conductivity is therefore important for evaluating the contribution of electrons to heat propagation in conductive polymer systems. This chapter investigates the temperature-dependent thermal transport properties of PEDOT:PSS thin films using PTR method. The experimental results are analyzed through frequency-dependent PTR amplitude and phase responses, providing insights into the thermal conductivity, thermal anisotropy, thermal diffusivity, and thermal boundary resistance of PEDOT:PSS thin films deposited on glass substrates. Attention is given to the correlation between thermal anisotropy and electrical conductivity

6.2 Motivation for Correlating Thermal and Electrical Transport in PEDOT:PSS Thin Films

Organic thermoelectric materials have attracted considerable attention in recent years because of their potential applications in flexible and wearable electronic devices, where waste heat can be directly converted into electrical energy. Compared with conventional inorganic thermoelectric materials such as Bi_2Te_3 and PbTe, conductive polymers offer several advantages including low density, mechanical flexibility, low-cost solution processing, and intrinsically low thermal conductivity. Among conductive polymers, PEDOT:PSS is considered one of the most promising candidates for thermoelectric applications due to its relatively high electrical conductivity, good environmental stability, and favorable mechanical properties. The efficiency of thermoelectric materials is commonly evaluated using the dimensionless figure of merit [1-5]:

$$ZT = \frac{S^2 \sigma T}{k} \qquad (6.1)$$

Where S is the Seebeck coefficient, σ is the electrical conductivity, k is the thermal conductivity, and T is the absolute temperature. High thermoelectric performance requires simultaneously maximizing electrical conductivity and Seebeck coefficient while minimizing thermal conductivity. However, these transport parameters are strongly interdependent. Increasing carrier concentration generally improves electrical conductivity but may also increase thermal conductivity and reduce the Seebeck coefficient. Consequently, understanding the correlation between electrical and thermal transport properties is essential for optimizing the thermoelectric performance of conductive polymers.

In conductive polymer systems, thermal transport originates from both lattice vibrations and electronic charge carriers. The total thermal conductivity can therefore be expressed as [2]:

$$k = k_e + k_l \qquad (6.2)$$

Where k_e and k_l represent the electronic and lattice contributions to thermal conductivity, respectively. In most polymers, lattice thermal conductivity is intrinsically low because of structural disorder, amorphous morphology, and weak intermolecular interactions between polymer chains. As a result, polymers typically exhibit thermal conductivity values below 0.5 $Wm^{-1}K^{-1}$. However, heavily doped conductive polymers such as PEDOT:PSS may exhibit enhanced thermal conductivity due to increased electron-assisted heat transport associated with high electrical conductivity. The electronic contribution to thermal conductivity is commonly described using the Wiedemann-Franz law [2]:

$$k_e = L\sigma T \qquad (6.3)$$

where L is the Lorenz number. For conventional metallic systems, the Lorenz number is generally equal to the Sommerfeld value, $L_0 = 2.44\times10^{-8}$ $W\Omega K^{-2}$. The Lorenz number describes the relationship between charge transport and electron-mediated heat transport. Although the Wiedemann–Franz law is well established for metals and many inorganic materials, its validity for conductive polymers remains uncertain because electrical transport in these materials is strongly influenced by structural disorder, hopping transport, localized charge carriers, and anisotropic morphology. Consequently, the effective Lorenz number in PEDOT:PSS may deviate significantly from the classical Sommerfeld value. Previous studies have demonstrated a correlation between electrical conductivity and thermal conductivity in PEDOT:PSS-based materials. Figure 6.1(a) presents the dependence of thermal conductivity on electrical conductivity for PEDOT:PSS systems reported in the literature using different Lorenz number values. The results indicate that

thermal conductivity increases approximately linearly with increasing electrical conductivity, suggesting an increasing electronic contribution to heat transport in highly conductive PEDOT:PSS films. The dashed lines correspond to different Lorenz number values relative to the Sommerfeld value, including $0.57L_0$, L_0 , and $2.35L_0$. These variations indicate that conductive polymers may exhibit substantial deviations from conventional metallic transport behavior. Figure 6.1(b) shows the calculated electronic contribution to thermal conductivity as a function of electrical conductivity based on the Wiedemann-Franz relation. The shaded region corresponds to the electrical conductivity range commonly observed for highly conductive PEDOT:PSS films. Within this conductivity range, the electronic thermal conductivity becomes comparable to the lattice thermal conductivity, indicating that electron-mediated heat transport may contribute significantly to the total thermal conductivity of conductive polymer systems [6-9].

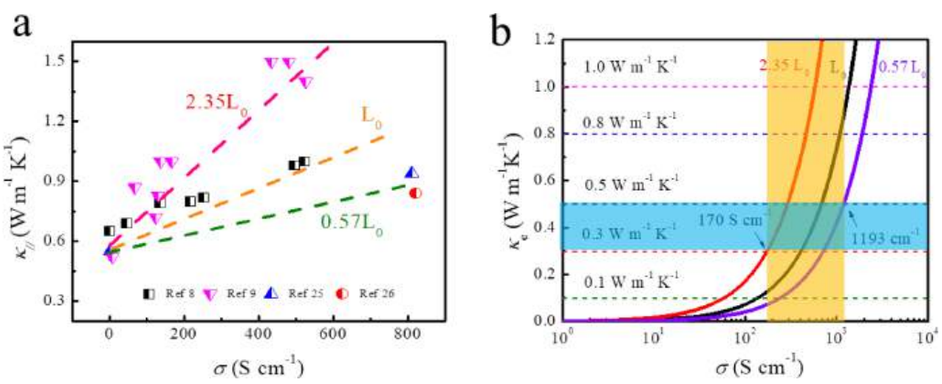

Figure 6.1. (a) Relationship between thermal conductivity and electrical conductivity for PEDOT:PSS-based materials reported in the literature for different Lorenz number values. (b) Electronic thermal conductivity as a function of electrical conductivity calculated using the Wiedemann-Franz law for different Lorenz numbers [9].

The room-temperature thermoelectric properties reported for PEDOT:PSS-based materials after various doping treatments and microstructural modifications are summarized in Table 6.1. Previous studies have primarily focused on improving the electrical conductivity and Seebeck coefficient of PEDOT:PSS through solvent treatment, secondary doping, and structural engineering approaches. As shown in Table 6.1, highly conductive PEDOT:PSS films can exhibit electrical conductivity values exceeding 10^3 S cm^{-1}, while maintaining relatively low thermal conductivity compared with conventional inorganic thermoelectric materials. These characteristics demonstrate the strong potential of PEDOT:PSS for flexible thermoelectric applications. Despite the increasing interest in PEDOT:PSS thermoelectric materials, relatively limited experimental information is available regarding their thermal transport properties. In particular, most reported studies provide only a single thermal conductivity value and do not distinguish between in-plane and cross-plane heat

transport. However, PEDOT:PSS thin films possess a highly anisotropic microstructure in which conductive PEDOT-rich domains preferentially align parallel to the film surface. Consequently, thermal transport is expected to differ significantly between the in-plane and cross-plane directions. Furthermore, only a limited number of studies have investigated the correlation between electrical conductivity and anisotropic thermal conductivity in PEDOT:PSS thin films. As a result, the electronic contribution to thermal transport and the applicability of the Wiedemann–Franz relation in conductive polymers remain insufficiently understood. Since the Lorenz number is directly related to the coupling between electrical and thermal transport, accurate determination of both in-plane and cross-plane thermal conductivity is necessary for evaluating electron-assisted heat conduction in conductive polymer systems.

Table 6.1. Summary of room-temperature thermoelectric properties of PEDOT:PSS-based materials after different doping treatments, compositing approaches, and microstructural modifications [9].

Methods	Treatment	σ (S cm^{-1})	S (μV K^{-1})	PF (μW m^{-1} K^{-2})	κ (W m^{-1} K^{-1})	ZT	Refs.
Doping Engineering	N_2 induced treatment with HNO_3	1293	27	94.3	-	-	[12]
	80% DMF and 20% water	1055	22.3	52	0.29 ($\kappa_\perp$)	0.05	[13]
	vapor treatment with H_2SO_4	1167	12.1	17	-	-	[14]
	1 M DMF solution of $ZnCl_2$	1400	26.1	98.2	-	0.12	[15]
	Treated with EG, PEG and FA	1900	20.6	80.6	-	-	[16]
	Treated with TSA and hydrazine	1310	49.3	318.4	0.3 ($\kappa_\perp$)	0.31	[17]
	Treated with H_2SO_4 and NaOH	2170	39.2	334	-	-	[18]
	BSA and hydrazine	1119	42.6	201.3	-	-	[19]
Compositing with inorganic filler	MoS_2	1250	19.5	45.6	0.27 ($\kappa_\perp$)	-	[20]
	SWCNT	1300	59	-	-	-	[21]
	SWCNT	1602	33.4	182.7	-	-	[22]
	SWCNT	1062	20	-	-	-	[23]
Microstructure control	Wet-spun and drawing	−2000	−15	40−50	-	-	[6]
	Stretching and solvent treatment	1155	18.1	37.2	-	-	[24]

The originality of the present work lies in the combined investigation of anisotropic thermal transport and electrical transport in PEDOT:PSS thin films. In this study, PTR is employed to measure all thermal transport parameters. The simultaneous evaluation of directional thermal transport properties enables a more comprehensive understanding of heat propagation mechanisms in PEDOT:PSS thin film. This approach enables evaluation of the electronic contribution to thermal conductivity and estimation of the effective Lorenz number in PEDOT:PSS thin films. Therefore, this work contributes to the limited experimental literature on anisotropic thermal transport in conductive polymers and provides important information for the development and optimization of organic thermoelectric materials and devices.

6.3 PTR measurements Results

6.3.1. Amplitude and Phase Results from Experimental Data

To facilitate comparison between the investigated samples, all experimental signals were normalized to the glass substrate reference. Following this normalization procedure, the substrate exhibited an amplitude ratio of 1 and a phase difference of 0°, which served as the baseline for evaluating the response of the coated samples. Figure 6.2 presents the normalized amplitude ratio

(a) and phase (b) response measured for the PEDOT:PSS-coated glass substrate with a film thickness of 480 nm at room temperature. The results show the variation of both amplitude and phase as a function of frequency, highlighting the effect of the PEDOT:PSS layer on the measured signal relative to the bare substrate.

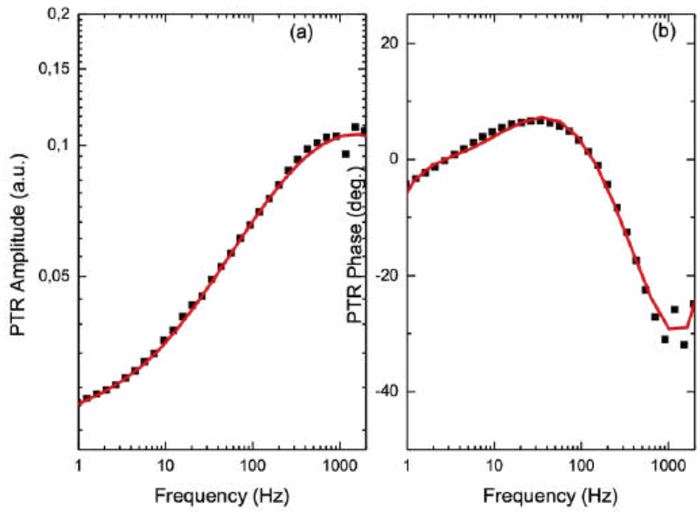

Figure 6.2. Normalized amplitude ratio and phase response of the PEDOT:PSS-coated glass substrate (thickness: 480 nm) measured at room temperature.

6.3.2. Temperature Dependence of Cross-Plane and In-Plane Thermal Conductivity

The in-plane and cross-plane thermal conductivities of the PEDOT:PSS thin film were extracted from the fitting of the experimental amplitude and phase data to the thermal transport model described in Chapter 4. The fitting procedure was performed at each measurement temperature, enabling the temperature dependence of the thermal conductivity components to be evaluated over the range from −50 °C to 50 °C. The fitted thermal conductivity values are summarized in Table 6.3. The table presents the in-plane thermal conductivity ($K_{\parallel}$), cross-plane thermal conductivity ($K_{\perp}$), and the corresponding thermal anisotropy ratio for the PEDOT:PSS film with a thickness of 480 nm deposited on a glass substrate. These values characterize heat transport through the film thickness and provide insight into the out-of-plane thermal transport mechanism. To quantify the directional dependence of heat transport, the thermal anisotropy ratio was calculated as $K_{\parallel}/K_{\perp}$. The variation of the thermal anisotropy ratio with temperature is shown in Figure 6.3.

Table 6.2. Fitted thermal transport parameters of the PEDOT:PSS film (480 nm) on a glass substrate over the temperature range from −50 °C to 50 °C.

Temperature (°C)	in-plane thermal conductivity (W/mK)	cross-plane Thermal Conductivity (W/m-K)	Thermal Diffusivity ($\times 10^{-7}$ m^2/s)	Thermal Boundary Resistance ($\times 10^{-9}$ m^2 KW^{-1})	Thermal Anisotropy $K_{\parallel}/K_{\perp}$	R^2
-50	0.35	0.17	2.66e-06	1.00e-06	2.06	0.9507
-25	0.66	0.23	2.41e-06	6.92e-07	2.87	0.952
0	0.99	0.26	2.80e-06	6.03e-07	3.81	0.959
25	1.1	0.3	1.6e-06	6.03e-07	3.67	0.958
50	1.82	0.38	1.89e-06	3.47e-07	4.79	0.957

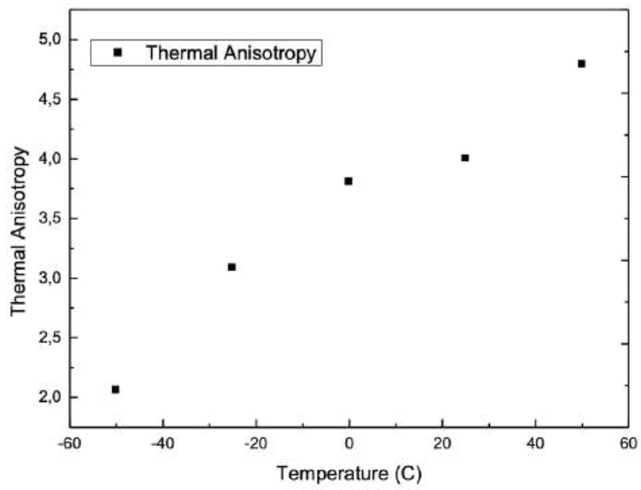

Figure 6.3. Thermal anisotropy ratio ($K_{\parallel}/K_{\perp}$) of the 480 nm PEDOT:PSS film on a glass substrate as a function of temperature.

The thermal anisotropy of the PEDOT:PSS thin films increase with increasing temperature, as evidenced by the rise of the anisotropy coefficient $K_{\parallel}/K_{\perp}$ from approximately 2.06 to 4.79. This behaviour indicates that heat transport becomes increasingly more efficient in the in-plane direction compared to the cross-plane direction at elevated temperatures. The stronger temperature dependence of the in-plane thermal conductivity suggests that the mechanisms governing heat transport are morphology-dependent within the polymer film. The observed increase in thermal anisotropy might be related to the anisotropic microstructure of PEDOT:PSS, where PEDOT-rich domains are preferentially aligned parallel to the substrate during film formation. As the temperature increases, phonon transport along these pathways may become more effective, resulting in a larger increase in $K_{\parallel}$ than in $K_{\perp}$. In addition, the increase in anisotropy might be explained by temperature-induced changes in the film morphology. Increasing temperature may promote polymer chain rearrangement, improved chain packing, and enhanced connectivity

between PEDOT-rich domains, which could facilitate heat transport within the film plane. In contrast, cross-plane heat transport may remain limited by structural disorder, weak interchain interactions, and interfaces between PEDOT-rich and PSS-rich regions. As a result, the difference between the in-plane and cross-plane thermal conductivities becomes more pronounced, leading to the observed increase in thermal anisotropy with temperature.

6.3.3. Correlation Between Thermal and Electrical Transport

To further investigate the contribution of charge carriers to heat transport in PEDOT:PSS thin films, the relationship between thermal conductivity and electrical conductivity was analyzed using the Wiedemann–Franz law given in Equation (6.3). The correlation between thermal conductivity and electrical conductivity for the cross-plane and in-plane directions is presented in Figures 6.4 and 6.5, respectively. Figures 6.4 and 6.5 show that thermal conductivity increases with increasing electrical conductivity in both transport directions. The approximately linear relationships observed in both cases suggest a strong coupling between thermal and electrical transport processes in PEDOT:PSS. This behaviour indicates that charge carriers contribute to heat transport and that the electronic contribution to thermal conductivity becomes increasingly important as electrical conductivity increases. The slope of the in-plane relationship is significantly larger than that of the cross-plane relationship, indicating that electron-assisted heat transport is more pronounced along the film plane. This observation is consistent with the anisotropic morphology of PEDOT:PSS, where conductive PEDOT-rich domains are preferentially aligned parallel to the substrate surface. Such alignment facilitates charge transport and heat propagation in the in-plane direction, while cross-plane transport remains limited by interfaces and structural disorder within the film.

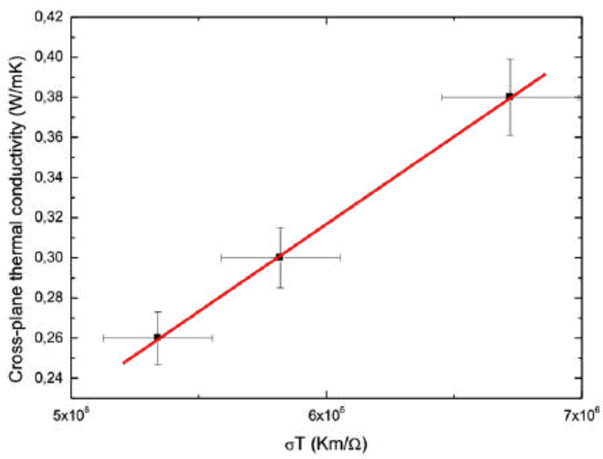

Figure 6.4. Relationship between cross-plane thermal conductivity and electrical conductivity of the 480 nm PEDOT:PSS thin film based on the Wiedemann-Franz law (Equation 6.3). The linear fit was used to determine the effective cross-plane Lorenz number.

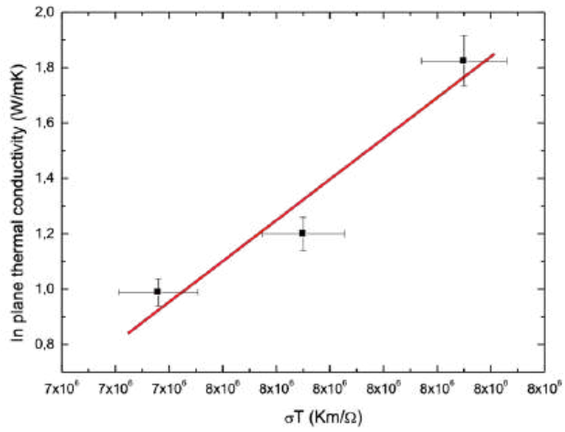

Figure 6.5. Relationship between In-plane thermal conductivity and electrical conductivity of the 480 nm PEDOT:PSS thin film based on the Wiedemann-Franz law (Equation 6.3). The linear fit was used to determine the effective cross-plane Lorenz number.

Table 6.3. Calculated Lorenz numbers for the PEDOT:PSS thin film (480 nm) on a glass substrate.

Direction	Lorenz number, L (W Ω K^{-2})	L_o (W Ω K^{-2})	L/L_o
Cross-plane	8.72×10^{-8}	2.44×10^{-8}	3.57
In-plane	1.48×10^{-6}	2.44×10^{-8}	60.57

The Lorenz numbers calculated from the experimental data are summarized in Table 6.3. For both transport directions, the obtained values exceed the Sommerfeld Lorenz number $L_o = 2.44 \times 10^{-8}$ W Ω K^{-2}. The cross-plane Lorenz number is approximately $3.57L_o$, whereas the in-plane Lorenz number reaches approximately $60.57\ L_o$. The large difference between the in-plane and cross-plane Lorenz numbers indicates a strong anisotropy not only in thermal conductivity but also in the coupling between thermal and electrical transport. The significantly higher in-plane Lorenz number suggests that electron-assisted heat transport is considerably more effective along the film plane than across the film thickness. This behaviour is consistent with the preferential alignment of PEDOT-rich conductive domains parallel to the substrate surface, which facilitates both charge transport and heat propagation in the in-plane direction. The observed Lorenz number anisotropy provides further evidence that thermal and electrical transport in PEDOT:PSS are strongly correlated and governed by the anisotropic microstructure of the film. The deviation of the measured Lorenz numbers from the classical Sommerfeld value also suggests that the transport mechanisms in PEDOT:PSS differ from those of conventional metallic systems and may involve additional contributions associated with disorder, carrier localization, and anisotropic charge transport pathway.

6.4. Conclusion

In this chapter, the thermal transport properties of PEDOT:PSS thin films were investigated using PTR technique. The results showed that both in-plane and cross-plane thermal conductivities increased with temperature, with a stronger increase observed in the in-plane direction. Consequently, the thermal anisotropy ratio increased with temperature, which may indicate increasingly efficient heat transport along the film plane. A correlation was also observed between thermal anisotropy and electrical conductivity. This behaviour may suggest a contribution of charge carriers to heat transport and a possible coupling between thermal and electrical transport processes in PEDOT:PSS. The observed anisotropic thermal transport might be related to the preferential alignment of PEDOT-rich domains within the film. The results suggest that both structural anisotropy and electronic transport may influence heat propagation in PEDOT:PSS thin films. These findings contribute to a better understanding of thermal transport mechanisms in conductive polymers and may support the development of PEDOT:PSS-based thermoelectric device.

6.5. References

[1] Z. Fan and J. Ouyang, "Thermoelectric properties of PEDOT:PSS," *Adv. Electron. Mater*., **5**, 1800769, (2019).

[2] D. Scheunemann and M. Kemerink, "Non-Wiedemann–Franz behavior of the thermal conductivity of organic semiconductors," *Phys. Rev. B*, **103**, 075206, (2021).

[3] P. S. Floris, N. Zahabi, I. Zozoulenko, and R. Rurali, "Anisotropic lattice thermal conductivity in highly ordered PEDOT fibers," *Macromol. Mater. Eng*., **309**, 2400092, (2024).

[4] J. Zhou, D. H. Anjum, L. Chen, X. Xu, I. Aguilar Ventura, L. Jiang, and G. Lubineau, "Temperature-dependent microstructure of PEDOT/PSS films: Insights from morphological, mechanical and electrical analyses," *J. Mater. Chem. C*, **2**, 9903–9910, (2014).

[5] P. S. Floris, C. Melis, and R. Rurali, "Interplay between doping, morphology, and lattice thermal conductivity in PEDOT:PSS," Adv. Funct. Mater., **33**, 2215125, (2023).

[6] D. Kim, "PEDOT:PSS-based high-performance thermoelectrics," *Macromol. Res*., **32**, 1187–1198, (2024).

[7] M. Zhang, X. Cao, M. Wen, C. Chen, Q. Wen, Q. Fu, and H. Deng, "Highly electrical conductive PEDOT:PSS/SWCNT flexible thermoelectric films fabricated by a high-velocity non-solvent turbulent secondary doping approach," *ACS Appl. Mater. Interfaces*, **15**, 10947–10957, (2023).

[8] A. Weathers, Z. U. Khan, R. Brooke, D. Evans, M. T. Pettes, J. W. Andreasen, X. Crispin, and L. Shi, “Significant electronic thermal transport in the conducting polymer poly(3,4-ethylenedioxythiophene),” *Adv. Mater*., **27**, 2101–2106, (2015).

[9] L. Liu, L. Liang, L. Deng, H. Wang, and G. Chen, “Is there a constant Lorentz number for organic thermoelectric materials?,” *Appl. Mater. Today*, **27**, 101496, (2022).

[10] A. Chatterjee, M. N. S. Swapna, A. Mikaeeli, M. Khalid, D. Korte, A. D. Wieck, and M. Pawlak, “Photothermal infrared radiometry and thermoreflectance: Unique strategy for thermal transport characterization of nanolayers,” *Nanomaterials*, **14**, 1711, (2024).

Chapter 7

Electrical Anisotropy in PEDOT:PSS Thin Films

7.1 Introduction

This chapter investigates the electrical anisotropy of PEDOT:PSS thin films fabricated under a laterally applied electric field during the spin-coating process. The primary aim is to understand how the applied field influences the structural organization of the polymer and its directional charge-transport properties. The resulting films exhibit clear anisotropic behavior, with enhanced conductivity (i.e., reduced resistance) in the direction perpendicular to the applied electric field; the underlying origin of this effect is discussed in the following sections. The chapter first outlines the concept of anisotropic transport in PEDOT:PSS and distinguishes electrical anisotropy from thermal conductivity anisotropy. It then considers the influence of the electric field on polymer morphology and charge transport. The experimental setup, sample preparation, and substrate optimization are subsequently described. Finally, results from macroscopic electrical measurements and C-AFM are presented to correlate field-induced structural changes with in-plane and cross-plane transport behavior.

7.2 Surface Anisotropy in PEDOT:PSS Thin Films

Since the late 1980s, poly(3,4-ethylenedioxythiophene) (PEDOT) has emerged as one of the most stable and versatile conducting polymers. Its steadily increasing electrical conductivity, combined with excellent environmental stability and optical transparency, has attracted considerable attention in both academia and industry. In its most widely used form, poly(3,4-ethylenedioxythiophene):poly(styrene sulfonate) (PEDOT:PSS), the polymer serves as a benchmark material for diverse applications, including thermoelectric devices, photovoltaic cells, solid-state lighting, electrochemical sensors, transparent electrodes, and bioelectronic interfaces [1-3]. Despite the extensive research and broad use of PEDOT:PSS, the large variability in reported conductivity values highlights the strong influence of microstructural disorder and morphological anisotropy on charge transport. The design of PEDOT:PSS films with optimal performance therefore requires a precise understanding of how structural ordering, phase separation, and processing conditions govern their anisotropic electrical behavior [4].

In most studies, electrical conductivity of polymer films is assumed to be isotropic, and measurements are commonly performed laterally along the film surface. However, due to the intrinsic chain anisotropy of conjugated polymers, the kinetics of film formation, and the complex phase-segregated morphology of PEDOT:PSS, the resulting thin films frequently exhibit anisotropic transport properties. The interplay between molecular alignment and film morphology gives rise to direction-dependent conductivity, typically with much higher in-plane conductivity compared to the out-of-plane direction [5]. Understanding this anisotropy is crucial because both in-plane and cross-plane charge transport strongly affect device operation in multilayer polymeric structures such as solar cells, electrochromic displays, and supercapacitors. In the present work, this anisotropic behavior is considered in terms of surface (in-plane) anisotropy, where the conductivity within the plane of the film varies depending on direction. An external electric field was applied during spin coating to impose a preferential alignment axis within the PEDOT:PSS layer. The resulting films were examined along two orthogonal in-plane directions: one parallel and one perpendicular to the applied field. This configuration enables a direct evaluation of how electric-field-induced chain orientation influences lateral charge transport and how surface anisotropy develops in PEDOT:PSS thin films.

7.3 Difference Between Electrical Anisotropy and Thermal conductivity Anisotropy

Electrical anisotropy and thermal conductivity anisotropy both describe directional dependencies in transport processes, yet the mechanisms governing them differ fundamentally, particularly in disordered semiconducting polymers such as PEDOT:PSS. Electrical conductivity in PEDOT:PSS is dominated by charge transport through PEDOT-rich domains embedded within an insulating PSS matrix. Charge carriers move primarily via thermally activated hopping and tunnelling between localized states, and the efficiency of this transport depends strongly on the spatial arrangement and connectivity of the PEDOT pathways. Any processing step that influences the microstructure, such as the application of a lateral electric field during deposition, can alter the conformation and local orientation of the polymer chains. As a result, the in-plane electrical conductivity may become directionally dependent because the percolation pathways for charge carriers are selectively enhanced or hindered in certain directions. In PEDOT:PSS, even subtle morphological rearrangements induced by an external electric field can lead to pronounced electrical anisotropy because charge transport is extremely sensitive to chain ordering, domain alignment, and the distribution of insulating PSS regions [7]. In contrast, thermal conductivity anisotropy in PEDOT:PSS arises from entirely different transport mechanisms. Heat in conducting polymers is carried predominantly by phonons rather than by mobile charge carriers [6,7]. The thermal conductivity therefore depends on the vibrational properties of the polymer backbone, the stiffness

of the molecular structure, and the scattering of phonons at interfaces or domain boundaries. Although PEDOT:PSS can exhibit relatively high electrical conductivity; especially when processed with high-boiling-point solvents such as dimethyl sulfoxide (DMSO), its thermal conductivity remains low because phonon transport is strongly hindered by the intrinsic disorder of the polymer network [6]. The material lacks the long-range crystallinity necessary for well-defined phonon propagation, which limits the degree to which thermal transport can become directionally dependent. Consequently, even when electrical conductivity becomes highly anisotropic, the thermal conductivity generally remains nearly isotropic [6,7]. This distinction becomes especially clear when considering the theoretical framework for thermoelectric materials. The efficiency of a thermoelectric material is described by the figure of merit ZT:

$$ZT = \frac{\sigma S^2 T}{\Lambda_e + \Lambda_{ph}} = \frac{S^2}{L}\left(\frac{\Lambda_e}{\Lambda_e + \Lambda_{ph}}\right) \qquad (7.1)$$

Where σ is the electrical conductivity, S is the Seebeck coefficient, T is the absolute temperature, Λ_e is the electronic component of the thermal conductivity, $\Lambda_{ph}$is the phonon contribution to the thermal conductivity, and L is the Lorenz number $L = \Lambda_e/(\sigma T)$, which links the electronic contribution to the thermal conductivity Λ_e with the electrical conductivity σ. All other things being equal, a small value of Lorenz number enhances ZT. In metals and heavily doped semiconductors, the electronic thermal conductivity is proportional to the electrical conductivity, and the Lorenz number closely follows the Sommerfeld value as predicted by the Wiedemann-Franz law. In PEDOT:PSS, however, this proportionality breaks down. The electronic contribution to thermal conductivity is very small compared to the phonon contribution, and the Lorenz number can deviate significantly from classical values because the charge carriers are strongly localized and the bandwidth is narrow [8]. As a result, even large variations in electrical conductivity, such as those caused by field-induced chain reorientation, do not translate into comparable variations in thermal conductivity.

7.4 Effect of Electric Field on the Anisotropic Electrical Conductivity of PEDOT:PSS Thin Films

Recent advances in organic optoelectronic devices based on conducting conjugated polymers have highlighted their potential for low-cost fabrication using solution-processable methods. The electronic properties of conjugated polymers are governed by the delocalization of π-electrons along and between the polymer backbones, which depend strongly on molecular stacking, chain alignment, and the degree of crystallinity. The self-assembly of polymer chains, including their

stacking order, interdomain connectivity, and orientation of crystalline regions, plays a crucial role in defining charge transport efficiency in these materials [9, 10]. To improve charge carrier mobility in polymeric semiconductors, various strategies have been explored, such as doping with organic molecules, inorganic nanoparticles, or through field-induced molecular alignment. Among these, the application of an external electric field during or after film formation has proven to be an effective means of controlling molecular orientation and thereby enhancing charge transport. Several studies have reported that high electric fields can induce dipolar alignment of polymer chains, leading to improved charge mobility and enhanced device performance in polymer solar cells and light-emitting diodes [11-14]. This effect has been attributed to the reorganization of conjugated backbones and polar side chains under the influence of the field, which promotes interchain charge transport and modifies the dielectric and electronic properties of the polymer network. PEDOT:PSS (poly(3,4-ethylenedioxythiophene):poly(styrene sulfonate)) is one of the most studied conducting polymers due to its high optical transparency, environmental stability, and excellent aqueous processability [15]. Structurally, PEDOT:PSS forms a phase-separated system composed of conductive PEDOT-rich domains embedded in an insulating PSS matrix. Charge transport in PEDOT:PSS films occur predominantly through hopping between localized states in PEDOT-rich regions. The application of an electric field enhances the hopping probability by reducing the effective potential barriers between adjacent conductive sites, resulting in field-assisted variable-range hopping (VRH) behavior. The relationship between conductivity, electric field, and temperature can be described by [16, 17]:

$$\sigma(E,T) = \sigma_0(T)exp[\gamma(E)] \qquad (7.2)$$

Where $\sigma_0(T)$ is the zero-field conductivity and $\gamma(E)$ represents a field-dependent enhancement factor related to tunneling probability and hopping distance. Under moderate fields, carrier motion follows a thermally activated hopping process, whereas at higher field strengths, non-ohmic conduction arises due to field-assisted tunneling across PSS barriers [18,19]. The impact of the applied field is typically more pronounced in the in-plane direction, since lateral PSS barriers are thinner and less continuous than the vertically oriented lamellae, resulting in stronger modulation of lateral charge transport [20].

Beyond charge-hopping effects, an electric field can induce significant morphological and conformational changes within the PEDOT:PSS matrix. The PEDOT:PSS complex exhibits inherent polarity due to electrostatic interactions between the positively charged PEDOT segments and the negatively charged sulfonate groups of PSS. When subjected to a sufficiently strong electric field, particularly during spin coating, these dipoles experience torque, which drives partial alignment of polymer backbones and reconfiguration of local domains [21, 22]. This reorientation

is often accompanied by a conformational transition of PEDOT chains from a coiled benzoid structure to a more linear quinoid configuration. The linear conformation enhances π–π stacking and charge delocalization along the polymer backbone, thereby increasing conductivity [23,24].

Experimental evidence supports that field-assisted deposition or post-treatment of PEDOT:PSS films can substantially alter film morphology and anisotropic transport characteristics. During spin coating under an applied electric field, redistribution of the insulating PSS phase and preferential alignment of PEDOT backbones can occur, resulting in enhanced connectivity of conductive pathways. It has been reported that the field can also reduce the accumulation of excess PSS near the film surface, further facilitating charge transport [25]. Similarly, electric-field-assisted spray deposition leads to the formation of elongated PEDOT grains and a more interconnected network, both of which contribute to enhanced in-plane conductivity [26].

In the present study, application of an electric field *during the spin-coating process* produced a measurable anisotropy in the in-plane electrical conductivity of PEDOT:PSS thin films. The resistivity along the direction of the applied field was found to be higher than that measured perpendicular to it. This anisotropy suggests that the electric field induces selective reorientation of PEDOT and PSS dipoles, which modifies the percolation pathways for charge transport. Conductive PEDOT domains tend to form elongated structures aligned along the field direction, while insulating PSS regions become oriented across these domains, hindering charge motion along the field but facilitating transport in the perpendicular direction. The electric field acts both as an electronic and structural modifier in PEDOT:PSS thin films. By promoting dipolar reorientation, conformational ordering, and redistribution of polymer phases, the field effectively tunes the anisotropy of electrical conductivity. This phenomenon provides not only a fundamental understanding of field-induced transport mechanisms but also a practical pathway for optimizing the performance of PEDOT:PSS-based devices such as organic solar cells, light-emitting diodes, and memory elements.

7.5 Comparison with Previous Studies and Originality of the Present Work

Electrical anisotropy in PEDOT:PSS has been widely reported, but the meaning and magnitude of the anisotropy strongly depend on the measurement geometry and intended application. In many studies, anisotropy refers to the difference between in-plane and out-of-plane conductivity, where PEDOT:PSS usually conducts much better along the film plane than through the film thickness. Nardes et al. reported strong intrinsic anisotropic hopping conduction in spin-coated PEDOT:PSS films, mainly arising from the layered PEDOT-rich/PSS-rich morphology 27, 28]. Na et al. also showed that solvent-induced morphology changes can strongly affect anisotropic conductivity in PEDOT:PSS films [29]. In these cases, the reported anisotropy is mostly related to vertical versus lateral transport, not to directional anisotropy within the plane of the film. A summary of

representative reported anisotropy magnitudes is given in Table 7.1. It is important to note that these values should not be compared only by magnitude, because different works measure different types of anisotropy.

Table 7.1. Comparison of anisotropy magnitudes reported in PEDOT:PSS-based systems and the present work.

Study	**Material/method**	**Type of anisotropy**	**Reported magnitude**	**Main difference from present work**
Nardes et al. [1,2]	Spin-coated PEDOT:PSS thin films	In-plane vs out-of-plane	typically, 2-3 orders of magnitude	Intrinsic vertical anisotropy; in-plane transport remained essentially isotropic
Na et al. [3]	Solvent-modified PEDOT:PSS films	In-plane vs out-of-plane	pristine films around 2 orders; solvent-treated films up to 3-4 orders	Morphology/solvent-induced vertical anisotropy, not lateral-field-induced in-plane anisotropy
van de Ruit et al. [30]	PEDOT:PSS films with varied thickness and PEDOT:PSS ratio	In-plane vs out-of-plane	2-4 orders of magnitude	Thickness/composition-dependent intrinsic anisotropy
Wang et al. [31]	Cellulose-PEDOT:PSS composites	In-plane vs out-of-plane	CNF-PEDOT:PSS: roughly 2 orders; pulp-PEDOT:PSS: less than 1 order	Thick composite films, no electric field
Gaál et al. [32]	GO/PEDOT:PSS multilayer films	In-plane vs out-of-plane	approximately 5 orders of magnitude	Multilayer self-assembled composite structure
Fujii et al. [33]	PEDOT:PSS nanosheet/lamellar assemblies	In-plane vs out-of-plane	almost 10^5	Template/lamellar assembly, not electric-field-induced in-plane anisotropy
Kim et al. [34]	PEDOT:PSS/PVA aligned hydrogels	Directional conductivity in hydrogel	$\sigma_{\parallel}/\sigma_{\perp}\approx 60.8$	Hydrogel composite, directional freezing/alignment
Chen et al. [35]	Wet-wound PEDOT:PSS thermoelectric films	In-plane anisotropy	In-plane anisotropy	Mechanical wet-winding alignment
Mahajan et al. [36]	PEDOT:PSS thin films treated by electric field	Directional in-plane anisotropy	modest, mainly percentage-level changes; anisotropy close to unity/factor ~1-2	modest, mainly percentage-level changes; anisotropy close to unity/factor ~1-2
Present work	PEDOT:PSS thin films under lateral electric field during spin coating	Directional in-plane anisotropy	$R_{\parallel}/R_{\perp}$ up to ~27	Electric field applied during liquid-state solidification

The most directly comparable study is that of Mahajan et al. [36], who investigated electric-field-induced dipolar reorientation in PEDOT:PSS thin films. They observed the same qualitative trend as in the present work: conductivity increased perpendicular to the applied electric field and decreased parallel to the field direction. However, in their case the electric field was applied after film formation, when the polymer morphology was already largely solidified. Therefore, the reported anisotropy remained relatively modest, mainly corresponding to small percentage-level conductivity variations or anisotropy factors close to unity. In contrast, in the present work the lateral electric field is applied continuously during spin coating and solvent evaporation, when the PEDOT:PSS complexes are still mobile. This enables stronger field-assisted reorganization before the polymer morphology becomes fixed. Other studies have achieved very large anisotropy values, but usually through different mechanisms and geometries. For example, Gaál et al. reported approximately five orders of magnitude anisotropy in graphene oxide/PEDOT:PSS multilayers, and Kim et al. reported $\sigma_{||}/\sigma_{\perp} \approx 60.8$ in aligned PEDOT:PSS/PVA hydrogels [32, 34]. These works demonstrate that strong anisotropic transport in PEDOT:PSS-based materials is scientifically important, but their anisotropy originates from multilayer stacking, hydrogel alignment, or mechanically directed morphology rather than from lateral electric-field-assisted solidification of a thin film. It should also be emphasized that a higher anisotropy is not universally "better" in every device. The desirable anisotropy depends on the intended application and on the required direction of charge transport. For transparent electrodes, solar-cell electrodes, OLEDs, and uniform heaters, nearly isotropic in-plane conductivity may be preferred because current should spread uniformly. In contrast, high anisotropy can be advantageous for devices requiring preferential current flow, directionally engineered conductive pathways, anisotropic sensors, thermoelectric structures, or neuromorphic/electronic elements where transport should be enhanced in one direction and suppressed in another. Therefore, the originality of the present work lies not simply in observing anisotropy in PEDOT:PSS, but in the specific method used to induce and investigate it. In contrast to previous studies, where anisotropy was mainly intrinsic, mechanically induced, or generated by electric-field treatment after film formation, the present work applies a continuous lateral electric field directly during spin coating and throughout the complete solvent-evaporation and solidification process. Under these conditions, the PEDOT:PSS complexes remain in a partially liquid and highly mobile state, allowing field-assisted dipolar and morphological reorganization to occur dynamically before the polymer network becomes frozen in the solid film. This distinguishes the present work fundamentally from post-treatment approaches, where the polymer morphology is already largely fixed. Furthermore, the present study demonstrates exceptionally strong directional in-plane anisotropy, with resistance anisotropy ratios $R_{||}/R_{\perp}$ reaching values up to approximately 27, which is substantially larger than the modest in-plane anisotropy previously

reported for electrically treated PEDOT:PSS thin films. Another important originality of the present work is the simultaneous real-time monitoring of electrical current during spin coating and polymer solidification. Unlike conventional studies, where films are characterized only after preparation, the present approach enables direct observation of the transient electrical evolution of the polymer during film formation, providing insight into ionic transport, solvent evaporation, dipolar mobility, and the transition from ionic to electronic conduction. Finally, the combination of macroscopic Van der Pauw anisotropy measurements with nanoscale conductive AFM analysis enables direct correlation between directional transport behavior and local conductive pathways within the PEDOT:PSS network. To the best of our knowledge, this combination of lateral electric-field-assisted spin coating, real-time electrical monitoring during solidification, and giant directional in-plane anisotropy in PEDOT:PSS thin films has not been extensively reported previously.

7.6 Experimental Setup and Preparation of PEDOT:PSS Thin Films Under Lateral Applied Electric Field

PEDOT:PSS (F HC Solar, Ossila; CAS 155090-83-8) was used as the conducting polymer in this study. F HC Solar is a water-based PEDOT:PSS formulation (Table 7.2) optimized for optoelectronic applications and characterized by high intrinsic conductivity together with excellent wetting behavior on common device substrates. These properties make it particularly suitable for investigating electric-field-induced modifications of thin-film morphology and directional in-plane electrical transport. In order to investigate the influence of a continuously applied lateral electric field during film formation, a custom-designed and custom-built spin-coating system was developed specifically for this work. Unlike conventional spin-coating systems, where thin films are deposited in the absence of an applied electric field and electrical characterization is performed only after fabrication, the present setup enables simultaneous in situ application of a lateral electric field and real-time electrical monitoring throughout the entire spin-coating and solidification process. To the best of our knowledge, this configuration has not been extensively reported previously for PEDOT:PSS thin-film processing and represents one of the key original aspects of the present work.

The system consisted of a Teflon rotating chuck incorporating two integrated electrical contacts to generate a controlled lateral electric field across the substrate during rotation. Figure 7.1 presents a photograph of the complete experimental setup, while Schematic 7.1 illustrates the electrical configuration, rolling-contact assembly, and field orientation relative to the substrate. One electrical contact was connected to the grounded steel rotation axis of the spinner, whereas the second contact was connected to a cylindrical stainless-steel electrode located beneath the Teflon stage. In order to ensure stable and reproducible electrical contact during high-speed rotation, a

rolling-contact mechanism based on miniature ball bearings was implemented. This design effectively replaced conventional sliding-contact approaches, thereby minimizing frictional wear, reducing electrical noise, and improving long-term contact stability during continuous operation. A DC voltage of 30 V was applied laterally across the substrate using a regulated power supply, corresponding to an average electric-field strength of approximately 3 V mm^{-1}. Importantly, the electric field remained continuously active from the moment the PEDOT:PSS droplet contacted the substrate until complete film solidification was achieved. This enabled direct field-assisted manipulation of the evolving PEDOT:PSS morphology while the polymer chains and ionic complexes remained mobile during solvent evaporation. A further unique capability of the setup was the integration of real-time current monitoring during film formation. The electrical circuit included a milliammeter connected in series with a Bluetooth-enabled OW18B data logger operating at a sampling rate of approximately 1 sample s^{-1}. This configuration enabled continuous in situ monitoring of the transient current flowing through the film during spin coating, solvent evaporation, and solidification. Consequently, the setup allowed direct observation of the electrical evolution of the PEDOT:PSS film during formation, including the transition from ionic conduction in the wet polymer state to predominantly electronic transport in the solidified film. For film deposition, the PEDOT:PSS solution was dispensed between two parallel indium contacts soldered onto the glass substrate. The substrate was rotated at 3500 rpm for 30 s to ensure homogeneous spreading and thin-film formation. Following deposition under continuous electrical bias, the films were annealed on a hot plate at 110 °C for 15 min in order to remove residual solvent and stabilize the final morphology. The selected electric-field strength was estimated to be sufficient to induce dipolar and morphological reorganization within the PEDOT:PSS network while maintaining negligible Joule heating (<0.1 W cm^{-2}). The resulting thin films were smooth, homogeneous, and suitable for subsequent Hall-effect, Van der Pauw, and conductive AFM characterization.

Table 7.2. Material specifications of the PEDOT:PSS formulation used in this study (F HC Solar, Ossila; CAS 155090-83-8).

Solvent	Composition	Solid content	Work function	Resistivity	Conductivity	Particle size distribution	Viscosity	PH value
Water	PEDOT:PSS	1.0 – 1.5 wt.%	4.8 – 5.0 eV	< 0.002Ω.cm	>500 S/cm	N/A	8 – 70 mPa.s	1.0 -2.0

Figure 7.1. Photographs of the custom-built electric-field-assisted spin-coating setup. (Left) Teflon rotation chuck with embedded electrode contacts. (Center) Rolling contact mechanism with miniature ball bearings integrated into the spinner base. (Right) Complete spin-coating workstation with DC power supply and current-measurement circuit.

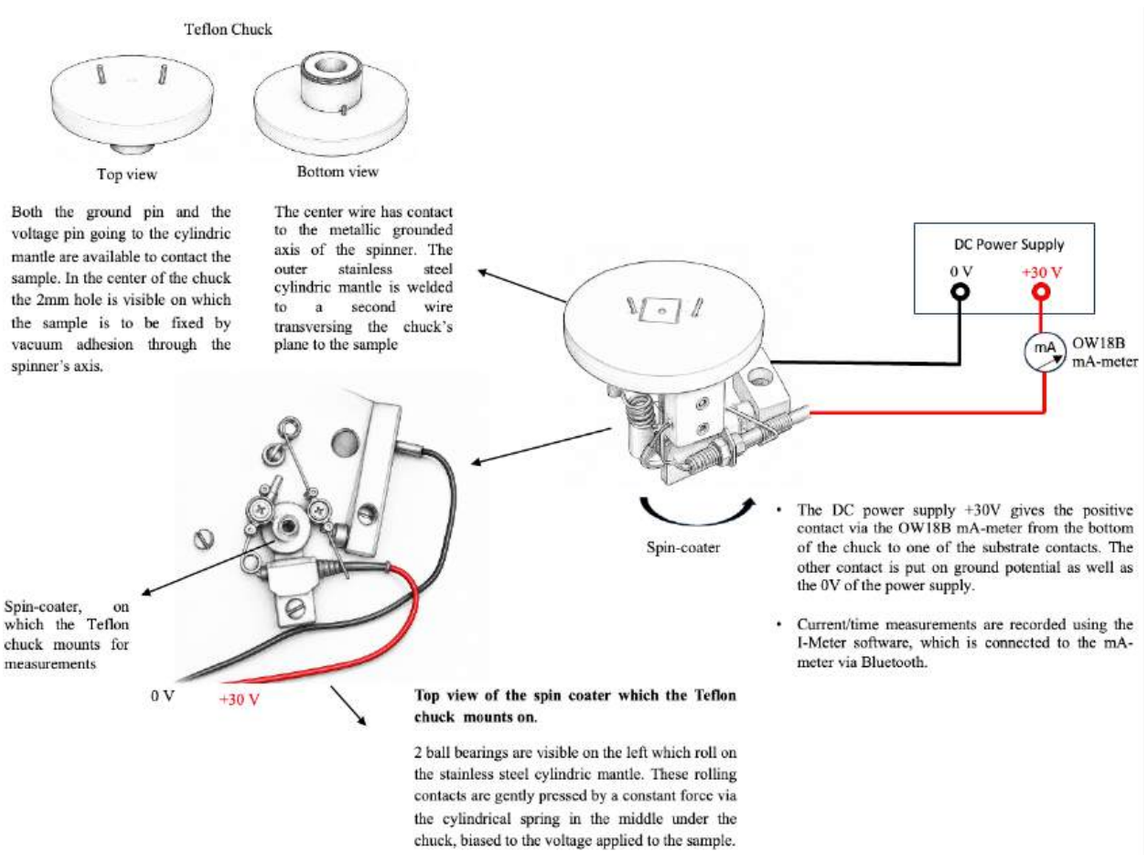

Schematic 7.1. Schematic illustration of the custom electric-field-assisted spin-coating setup used for PEDOT:PSS thin-film deposition

7.7 Sample Preparation for Electric-Field-Assisted PEDOT:PSS Thin Films

Square glass substrates (10 ×10 mm^2) were used for the preparation of PEDOT:PSS thin films under an applied lateral electric field. Prior to deposition, the substrates were cleaned sequentially with acetone and isopropanol using a spin coater operated at 3500 rpm for 30 s in each solvent, followed by drying under compressed air. Two parallel Indium contacts were then formed on opposite sides of each substrate using a Weller WECP-20 soldering station set to 350 °C. These Indium electrodes served as lateral contact pads for applying the external electric field during spin coating. Fine Cu-wires (Tin coated) were soldered to the center of each indium contacts to establish electrical connection between the substrate and the external circuit through the rolling-contact mechanism integrated into the modified spin coater. This arrangement, shown in Figure 7.2 (a) and Figure 7.2 (b), enabled continuous electrical biasing of the substrate during high-speed rotation and ensured uniform field distribution across the film throughout deposition. For film fabrication, the PEDOT:PSS solution was dispensed onto the rotating substrate while a constant lateral bias of 10 V was applied between the indium electrodes. The substrate was spun at 3500 rpm for 30 s, ensuring uniform spreading and thinning of the solution. Based on manufacturer data for PEDOT:PSS F HC Solar, this spin speed corresponds to an expected film thickness of approximately 80-100 nm, as shown in Figure 7.3. After deposition, the samples were annealed at 110 °C for 15 minutes on a hot plate to remove residual solvent and improve film homogeneity. Once cooled, the parallel Indium contacts were carefully removed to prepare the samples for Hall-effect measurements. The Indium was mechanically detached by gentle scratching to avoid damaging the PEDOT:PSS film. For electrical characterization in the Van der Pauw configuration, four ohmic contacts were formed at the corners of the PEDOT:PSS film using high-conductivity silver paste. The sample was then mounted onto a chip carrier, and each contact was soldered to the carrier terminals using Copper (Tin coated) wires, as shown in Figure 7.2 (c). This configuration enabled precise determination of sheet resistance and facilitated analysis of the in-plane anisotropic electrical behavior of the field-treated PEDOT:PSS films.

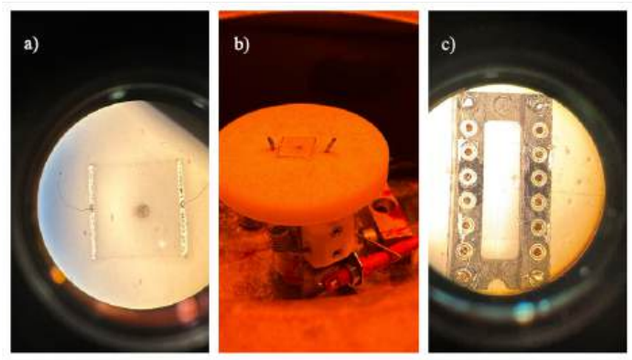

Figure 7.2. Sequential preparation steps for PEDOT:PSS thin films under lateral electric-field-assisted spin coating: (a) glass substrate (10 × 10 mm^2) with parallel indium contacts and attached Copper wires, prepared for biased deposition; (b) substrate mounted on the custom Teflon chuck inside the spin coater during field-assisted deposition; (c) final PEDOT:PSS film mounted on a chip carrier with silver-paste corner contacts for Van der Pauw electrical characterization.

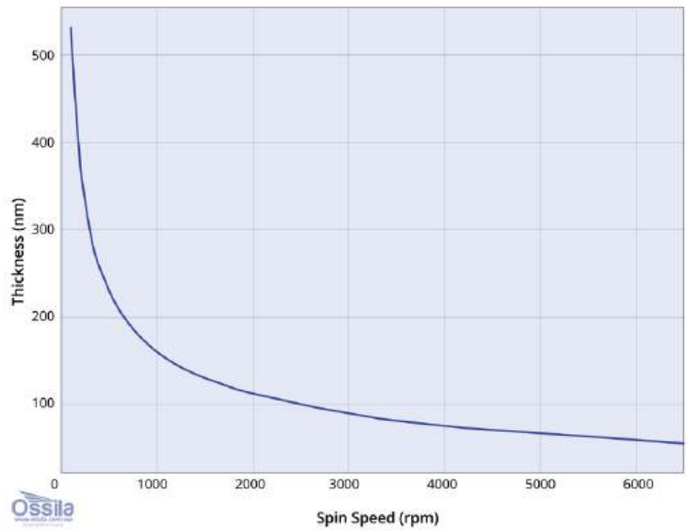

Figure 7.3. Thickness of PEDOT:PSS F HC Solar films as a function of spin speed, based on manufacturer data (Ossila). At the spin speed used in this study (3500 rpm), the corresponding film thickness is approximately 80-100 nm.

7.8 Substrate Geometry and Dimensional Optimization

To ensure consistent and reliable evaluation of anisotropic electrical properties, two substrate geometries were employed in this study: square (10 × 10 mm^2) and rectangular (10 × 8 mm^2) glass substrates. The selection and refinement of these dimensions were motivated by the need to maintain well-defined geometry after removal of the Indium contacts used during electric-field-assisted spin coating. For the square substrates, two parallel Indium contacts were soldered along

the opposing 10 mm edges prior to PEDOT:PSS deposition. Following spin coating and thermal annealing, the Indium contacts were carefully removed to prepare the samples for Hall and Van der Pauw measurements. As this cleaning step mechanically removed approximately 1 mm of film from each contacted edge, the final effective film area was reduced to about 10 × 8 mm^2. To achieve higher geometric precision and reproducibility across all samples, a second series of rectangular substrates (10 × 8 mm^2) was prepared, with the Indium contacts positioned along the 10 mm edges. After deposition and removal of the Indium, the final film area was consistently 8 × 8 mm². This pre-adjusted geometry ensured that all samples used for in-plane anisotropy measurements possessed identical dimensions, thereby eliminating geometric artifacts that could otherwise influence the comparison between resistances measured parallel and perpendicular to the applied electric field. This optimization of substrate design and contact positioning was essential to guarantee measurement accuracy and reproducibility in the study of electric-field-induced anisotropy in PEDOT:PSS thin films.

7. 9 Results

7.9.1 In-Plane Electrical Anisotropy of Electric-Field-Assisted PEDOT:PSS Thin Films

To evaluate the in-plane electrical anisotropy induced by the lateral electric field during spin coating, the four-contact Van der Pauw technique was applied to each PEDOT:PSS thin film. Figure 7.4 (a) illustrates the direction of the electric field imposed during film formation, applied laterally between two parallel Indium contacts. After the Indium contacts were removed, four ohmic contacts were deposited at the corners of the film Figure 7.4 (b), establishing the standard Van der Pauw geometry for resistivity measurements.

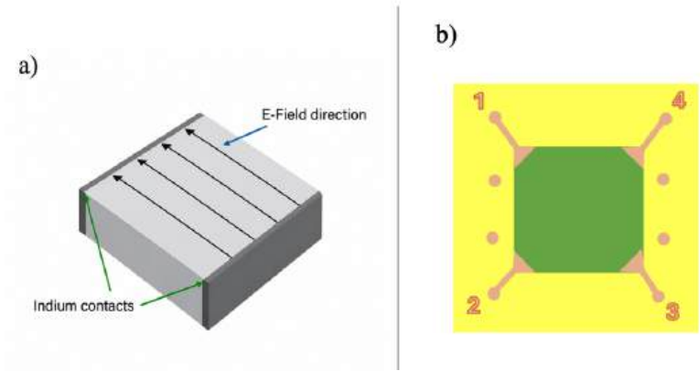

Figure 7.4. (a) Schematic of the lateral electric field applied between two parallel indium contacts during spin coating. (b) Van der Pauw configuration used after removing the Indium contacts, with four corner contacts for measuring in-plane directional resistances.

In this configuration, the contact pairs (1-2) and (3-4) lie along the direction perpendicular to the applied electric field, whereas the pairs (1-4) and (2-3) lie parallel to the field. The corresponding resistances were therefore assigned as:

$$R_{\perp} = R_{\mathrm{S1,2\ M4,3}}, \qquad R_{\parallel} = R_{\mathrm{S1,4\ M2,3}},$$

where the notation $R_{\mathrm{Sx,y\ Mz,w}}$ denotes that current is sourced between contacts *x*-*y* (S = source) and the voltage drop is measured between contacts *z*-*w* (M = measure). Using this directional contact scheme, both $R_{\perp}$ and $R_{\parallel}$ were measured for each film, and the electrical anisotropy was quantified by the ratio:

$$\frac{R_{\parallel}}{R_{\perp}}.$$

The results obtained from the Van der Pauw measurements (summarized in Tables 7.3 and 7.4 for the square and rectangular samples, respectively and the corresponding plotted datasets are shown in Figure 7.5 (a, b) clearly demonstrate that PEDOT:PSS thin films prepared under a lateral electric field exhibit a pronounced directional dependence in their in-plane resistance. For all samples, irrespective of geometry (10 × 8 mm^2 or 8 × 8 mm^2 final dimensions), the resistance measured parallel to the applied electric field, $R_{\parallel}$, was consistently higher than the resistance measured perpendicular to the field, $R_{\perp}$. The anisotropy ratio $R_{\parallel}/R_{\perp}$ ranged from ~1.7 to ~23.7 for square substrates and from ~3.5 to ~27.3 for rectangular substrates, demonstrating that the field-induced anisotropy is both strong and reproducible across different substrate geometries.

Although all PEDOT:PSS films were prepared under nominally identical conditions and had comparable thicknesses, the anisotropy ratio varied significantly from sample to sample. This variation is expected because the final electrical anisotropy is governed not only by the macroscopic processing parameters, such as film thickness, applied field, and substrate geometry, but also by the microscopic percolation network formed during solvent evaporation. PEDOT:PSS film formation is a dynamic liquid-to-solid process, and small local variations in wetting, solvent evaporation rate, residual solvent distribution, contact edge effects, and PEDOT-rich/PSS-rich domain organization can lead to different degrees of dipolar alignment and domain connectivity. Since charge transport in PEDOT:PSS is highly sensitive to the connectivity of PEDOT-rich conducting pathways and the distribution of PSS-rich insulating barriers, even small microstructural differences can produce large changes in the measured anisotropy ratio. Therefore, the variation in $R_{||}/R_{\perp}$ does not contradict the reproducibility of the effect. On the contrary, the important observation is that all samples consistently show $R_{||} > R_{\perp}$, confirming that the lateral

electric field systematically induces anisotropic in-plane transport. The particularly high ratios observed in some samples, such as square sample 7 and rectangular sample 2, may indicate a more strongly disrupted parallel transport pathway or a more effective perpendicular PEDOT-rich percolation path. Conversely, lower ratios, such as square sample 5, may correspond to a weaker degree of field-induced ordering or a more isotropic local morphology. Thus, the ratio reflects the local balance between field-induced alignment and the stochastic nature of polymer self-organization during drying.

Table 7.3. In-plane electrical anisotropy of PEDOT:PSS thin films (≈80 nm) deposited on square 10 × 10 mm^2 substrates under a lateral electric field of 3 V mm⁻¹. Perpendicular ($R_\perp$) and parallel ($R_{||}$) resistances extracted from Van der Pauw measurements are listed together with the anisotropy ratio ($R_{||}/R_\perp$) and the corresponding fitting error.

Sample	$R_\perp$ (Ω)	$R_{||}$ (Ω)	Ratio	Rs_error
1	23,41	72,72	3,11	0.01019
2	39,14	333,26	8.51	0.0249
3	55,58	197,71	3.56	0.00552
4	17,89	179,82	10.05	0.03212
5	42,84	73,31	1.71	0.00741
6	45,79	325,48	7.10	0.04616
7	9,68	229,73	23.72	0.06498

Table 7.4. In-plane electrical anisotropy of PEDOT:PSS thin films (≈80 nm) deposited on rectangular 10 × 8 mm^2 substrates under a lateral electric field of 3 V mm⁻¹. Perpendicular ($R_\perp$) and parallel ($R_{||}$) resistances extracted from Van der Pauw measurements are listed together with the anisotropy ratio ($R_{||}/R_\perp$) and the corresponding fitting error.

Sample	$R_\perp$ (Ω)	$R_{||}$ (Ω)	Ratio	Rs_error
1	25,91	152,7	5,89	0,07821
2	8,59	234,79	27,33	0,11552
3	25,94	90,96	3,5	0,01141

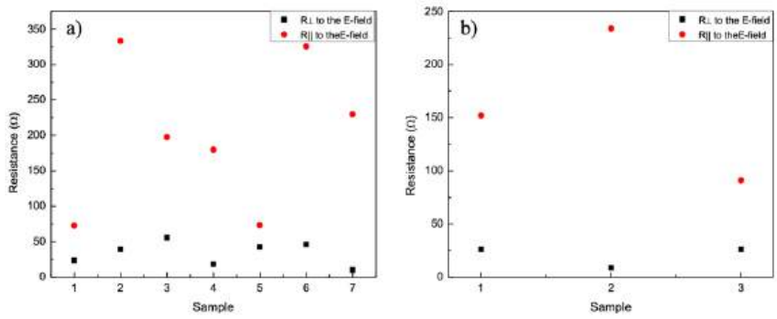

Figure 7.5. In-plane resistance anisotropy in PEDOT:PSS thin films prepared under a lateral electric field. (a) Resistances measured perpendicular ($R_{\perp}$) and parallel ($R_{||}$) to the applied electric field for square samples (10 × 10 mm^2, ~80 nm thick), corresponding to the data in Table 7.2. (b) Equivalent measurements for rectangular samples (final film area 10 × 8 mm^2), corresponding to the data in Table 7.3. In all cases, ($R_{||}$) is significantly larger than $R_{\perp}$, demonstrating a robust and reproducible field-induced anisotropy in the in-plane conductivity.

7.9.2 Interpretation of Field-Induced In-Plane Electrical Anisotropy

The systematic increase in resistance along the direction parallel to the applied electric field together with the decrease in resistance in the perpendicular direction strongly indicates that the electric field actively modifies the microstructure of the PEDOT:PSS network during film solidification. The experimentally observed in-plane electrical anisotropy can be interpreted in terms of electric-field-induced dipolar reorganization of the PEDOT:PSS complexes and the resulting anisotropic restructuring of the conducting percolation network. Previous studies on electrically treated PEDOT:PSS thin films have proposed that the positively charged PEDOT segments and negatively charged sulfonate groups of PSS form intrinsic dipoles along the PEDOT:PSS complexes. In the absence of an external electric field, these dipoles are randomly oriented throughout the polymer film, resulting in nearly isotropic in-plane conductivity. Under the influence of an external electric field, however, partial dipolar alignment can occur, leading to anisotropic electrical transport. Figure 7.6, schematically illustrates the random orientation of PEDOT:PSS dipoles before electric-field treatment and their partial alignment under an applied electric field, as proposed in previous literature. In earlier studies from other groups, the electric field was applied to already formed PEDOT:PSS films for relatively long treatment times of several hours in order to induce dipolar reorientation [36]. The trick in the current work ist that the orientation takes place already in the liquid phase of the PEDOT:PSS. In this way, already the very weak electric field of only about 30 V/cm leads to the anisotropy after drying out. Usually, electric fields in semiconductors or insulators like in MOSFETs are in contrast of the order of 1 - 7 × 106 V/cm, i.e. 5 orders of magnitude larger! It would be interesting to check the maximum electric field strength liquid PEDOT:PSS can support without electric breakdown.

Some other interesting aspect is the dry-out dynamics of liquid PEDOT:PSS films: Due to residual (leakage) currents and the applied voltage, there is a thermal Joule-impact on the drying layer by temperature increase. While the relatively weak electric field of 30 V/cm can probably not tear apart molecular filaments, this heat accelerates drying out and stops almost upon total dry-out due to a stop of ion movement. These aspects belong to the outlook of this thesis, worth to be investigated further.

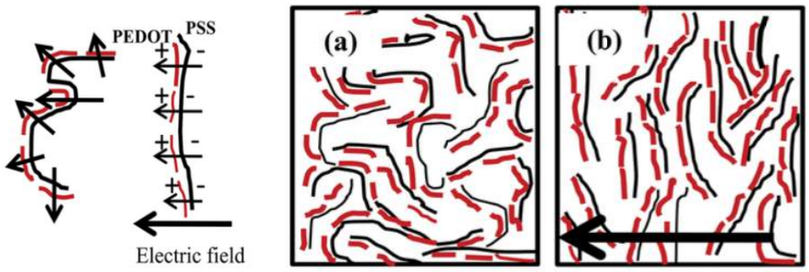

Figure 7.6. Schematic representation of the random orientation of PEDOT:PSS dipoles before electric-field treatment and their partial alignment under an applied electric field [36].

In the present work, however, the lateral electric field was applied directly during spin coating and film solidification. Under these conditions, the polymer remains in a viscous and partially mobile state because of the residual solvent present during film formation. Consequently, the PEDOT:PSS dipoles can respond more readily to the applied electric field, allowing anisotropic reorganization to occur within a much shorter time and at relatively low applied voltages. As solvent evaporation proceeds, the electrically induced morphology becomes progressively frozen into the solid film.

The strong and systematic in-plane anisotropy observed in all PEDOT:PSS thin films can therefore be attributed to the dipolar nature of the PEDOT:PSS complexes and their partial reorientation during solidification under the applied lateral electric field. When a lateral electric field of approximately 3 V mm^{-1} is applied during spin coating, the dipoles experience an electric-field-induced torque that promotes directional rearrangement of the PEDOT-rich and PSS-rich regions. The PSS-rich insulating domains are proposed to preferentially align along the electric-field direction, forming elongated insulating barriers, while the conductive PEDOT-rich pathways become more interconnected in the perpendicular direction. This morphological evolution results in a highly anisotropic percolation network within the film plane. A schematic representation of the proposed morphology together with the four-probe measurement geometry is shown in Figure 7.7. In the present configuration, the contacts 1-2 and 4-3 correspond to the direction perpendicular to the applied electric field, whereas the contacts 1-4 and 2-3 correspond to the direction parallel to the electric field. Charge transport perpendicular to the electric field intersects a larger number of

interconnected PEDOT-rich pathways and encounters fewer insulating PSS barriers. Since charge transport in PEDOT:PSS is more efficient along interconnected PEDOT-rich domains, the perpendicular direction exhibits lower resistance and enhanced conductivity. In contrast, charge carriers moving parallel to the electric field encounter a larger number of aligned PSS-rich insulating barriers, resulting in increased scattering, reduced pathway connectivity, and higher measured resistance. The experimentally observed relationship

$$R_{||} > R_{\perp} \Rightarrow \sigma_{\perp} > \sigma_{\parallel} \qquad (7.3)$$

is therefore a direct manifestation of the anisotropic restructuring of the PEDOT:PSS percolation network induced by the applied electric field during film solidification. Although all samples consistently exhibited anisotropic transport behavior, the magnitude of the anisotropy ratio varied between approximately 2% and 27%. This variation likely originates from the partially stochastic nature of polymer self-organization during solvent evaporation. Even under nominally identical preparation conditions, local differences in solvent evaporation dynamics, PEDOT-rich domain connectivity, and the degree of partial dipolar alignment can produce variations in the final anisotropic morphology. Nevertheless, the consistent observation of enhanced conductivity perpendicular to the applied electric field in all samples strongly supports the reproducibility of the field-induced anisotropic transport mechanism.

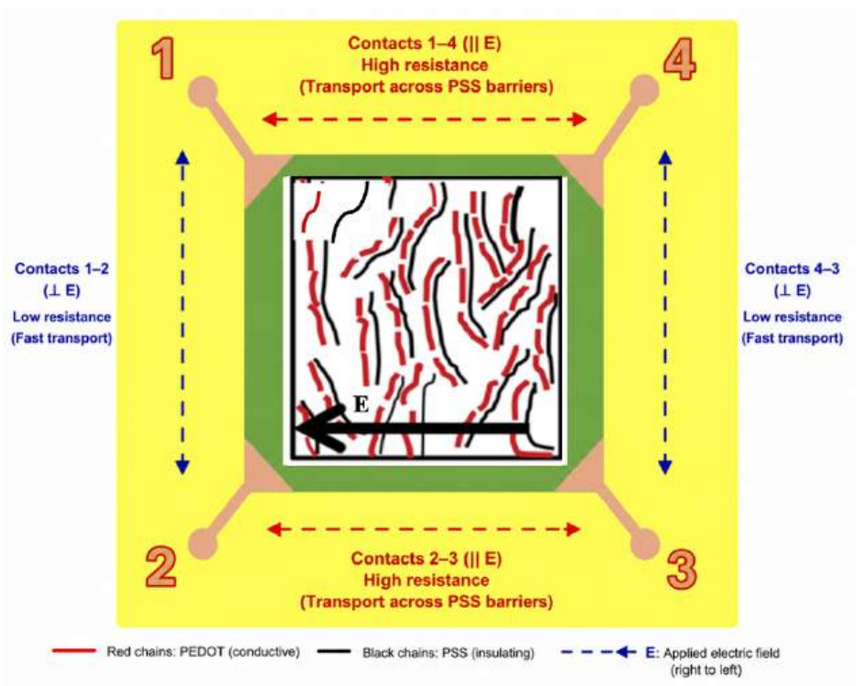

Figure 7.7. Schematic illustration of the proposed anisotropic morphology of the PEDOT:PSS film after application of a lateral electric field during solidification together with the four-probe measurement geometry. The contacts 1-2 and 4-3 correspond to charge transport perpendicular to the applied electric field and exhibit lower resistance due to transport through more interconnected PEDOT-rich pathways. The contacts 1-4 and 2-3 correspond to charge transport parallel to the electric field and exhibit higher resistance because charge carriers encounter aligned PSS-rich insulating barriers.

7.9.3 Electrical Conductivity of PEDOT:PSS Thin Films on Square and Rectangular Substrates

The electrical conductivity values of representative PEDOT:PSS thin films deposited on both square (S) and rectangular (R) substrates are summarized in Table 7.5. All samples exhibit conductivities in the range of approximately 320-535 S/cm, confirming the high electrical performance of the films under the applied processing conditions. The variations in conductivity are consistent with the corresponding differences in sheet resistance, while the film thickness remained constant (~80 nm). Furthermore, no systematic dependence on substrate geometry is observed, indicating that the electrical properties are primarily governed by the intrinsic film morphology rather than geometric factors.

Table 7.5. Electrical conductivity of representative PEDOT:PSS thin films (~80 nm) deposited on square and rectangular substrates under identical conditions. The corresponding sheet resistance values are included for comparison.

Sample	Geometry	R_sheet (Ω)	Conductivity (S/cm)
S1	Square	266.01	469.90
S2	Square	392.06	318.84
S3	Square	305.34	409.37
R1	Rectangular	320.03	390.59
R2	Rectangular	300.46	416.02
R3	Rectangular	233.69	534.89

7.9.4 Real-Time Monitoring of Voltage and Current During Polymer Solidification in PEDOT:PSS (F HC Solar) Thin Films Under a Lateral Electric Field

The real-time current measurements recorded during the electric-field-assisted spin-coating process provide direct insight into the electrical and morphological evolution of the PEDOT:PSS film during polymer solidification. In all samples, both square (10 × 10 mm^2) and rectangular (10 × 8 mm^2), the current remained essentially zero before deposition, as expected for an open circuit with no conductive film bridging the Indium contacts. Immediately upon dispensing the PEDOT:PSS solution onto the substrate (t=0 s), a sharp rise in current was observed in every sample, reaching

peak values in the range of approximately 150-500 μA depending on the specific sample and contact wetting dynamics. This rapid increase reflects the moment at which the fluid PEDOT:PSS solution establishes electrical connectivity between the two biased Indium contacts.

In its liquid state, the aqueous PEDOT:PSS dispersion forms a continuous ionic conduction pathway, enabling significant current flow dominated by mobile ions, charged species, and loosely associated PEDOT:PSS colloidal particles. At this stage, the polymer chains remain highly mobile because the film still contains a substantial amount of solvent. Consequently, even the relatively small applied lateral electric field of approximately 3 V mm^{-1} is sufficient to influence the orientation of the dipolar PEDOT:PSS complexes. The electric field can therefore exert a torque on the ionic dipoles while the film is still wet, initiating the earliest stages of field-driven chain and domain reorganization. In contrast, once the polymer layer becomes dry and solidified, the mobility of the polymer chains is strongly reduced, and such a relatively small electric field would no longer be sufficient to induce significant molecular reorientation. This highlights the importance of applying the electric field during the liquid-state spin-coating and solidification process rather than after complete film formation.

Following the initial current maximum, all samples exhibit an overall monotonic decay in current over the duration of spinning (~30 s). This decay directly correlates with solvent evaporation, progressive thinning of the film, and the gradual reduction of ionic mobility within the polymer layer. As the solvent evaporates, the ionic conduction pathways progressively collapse because the motion of ions and charged colloidal species becomes increasingly restricted. Consequently, the electrical resistance increases continuously during drying, resulting in the characteristic decrease in current observed in nearly all samples under constant applied voltage. This behavior can therefore be interpreted as a dynamic transition from ionic conduction in the wet polymer state to predominantly electronic transport in the solidified PEDOT:PSS network.

As the film approaches solidification, charge transport becomes increasingly dominated by electronic hopping between PEDOT-rich domains rather than ionic motion through the liquid dispersion. The residual low-level current observed near the end of the spin-coating cycle reflects the intrinsic conductivity of the partially solidified PEDOT:PSS network under the applied lateral electric field. Interestingly, in several samples, particularly samples 1, 4, and 6 shown in Figure 7.8, secondary features such as small current increases or fluctuations appear after approximately 20–30 s. Although the exact origin of this behavior remains unclear, it likely reflects sudden microstructural changes occurring during the final stages of polymer solidification. Possible explanations include transient redistribution of residual solvent pockets, local rearrangement of PEDOT:PSS microdomains under the continuing electric field, or abrupt changes in ionic mobility as the polymer transitions from a liquid-like to a solid-like state. Such behavior is consistent with

the highly complex and dynamic nature of solvent evaporation and microstructural evolution in conducting polymer dispersions.

Importantly, although the detailed current evolution is not perfectly reproducible for every sample, the overall behavior remains remarkably consistent. In nearly all cases, the current exhibits a strong initial rise followed by a gradual decay during drying. Minor variations between samples are expected because the system consists of a highly complex liquid polymer dispersion in which small differences in solvent distribution, local film thickness, contact wetting, ionic concentration, and polymer domain organization can influence the transient electrical response. Therefore, the observed current evolution should primarily be interpreted qualitatively rather than as perfectly reproducible quantitative curves. In this context, sample 6 appears somewhat exceptional and exhibits behavior that cannot yet be fully explained within the present framework.

Despite these variations, the overall similarity of the current evolution profiles observed for both square (Figure 7.8) and rectangular (Figure 7.9) samples demonstrates that the electrical response during solidification is governed primarily by intrinsic electrohydrodynamic and ionic processes within the PEDOT:PSS film rather than by substrate geometry. More importantly, these real-time measurements provide a unique opportunity to directly monitor the dynamic evolution of the polymer during film formation. In contrast to conventional approaches, where samples are characterized only after preparation, the present method allows direct observation of the electrical behavior of the film during the actual spin-coating and solidification process. The time-dependent current evolution therefore acts as a “magnifying glass” into the transient processes occurring inside the polymer film during drying, providing valuable insight into solvent evaporation, ionic transport, dipolar mobility, and field-induced microstructural reorganization.

To the best of our knowledge, real-time monitoring of the electrical response of PEDOT:PSS thin films during electric-field-assisted spin coating and solidification has not been extensively reported in the literature. Most previous studies investigate the electrical properties of conducting polymer films only after complete film formation. In contrast, the present approach enables direct observation of the dynamic electrical evolution of the polymer during the actual preparation process. This provides a unique opportunity to correlate transient current behavior with solvent evaporation, ionic mobility, dipolar reorientation, and microstructural evolution occurring during film solidification. Consequently, the present method opens a new experimental pathway toward a deeper understanding of the relationship between processing conditions, microstructure formation, and anisotropic charge transport in conductive polymer thin films.

Together, these real-time electrical measurements strongly support the interpretation that the PEDOT:PSS film undergoes a continuous transition from ionic conduction in the wet state to electronic conduction in the dry state, while the applied lateral electric field actively influences

dipolar alignment and domain organization throughout the period in which the polymer remains mobile.

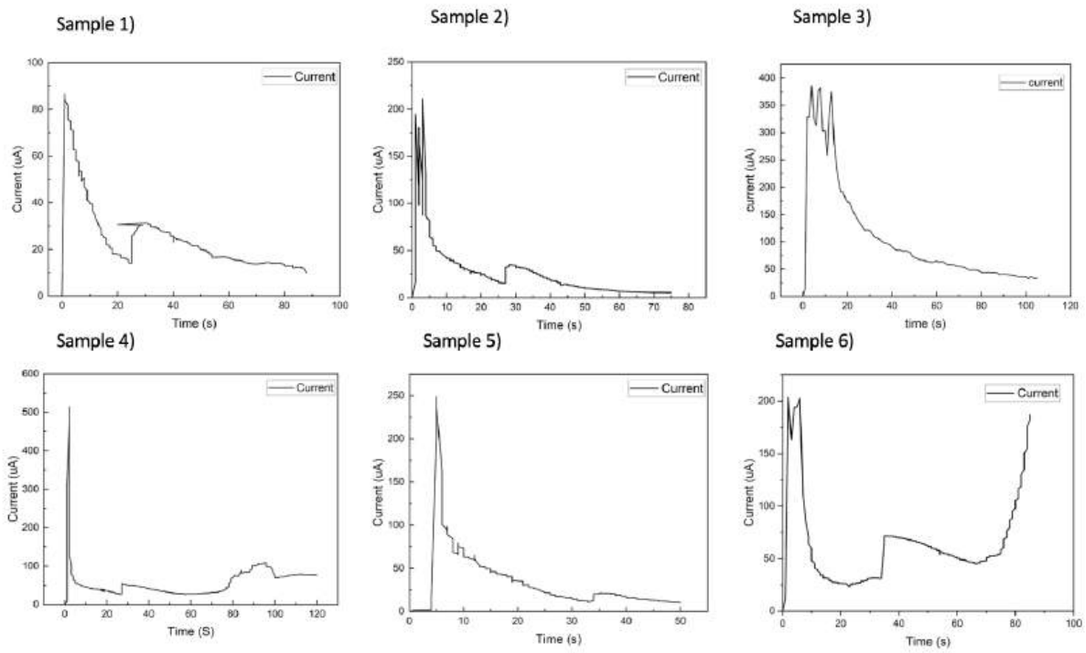

Figure 7.8. Real-time current evolution during the 30-s spin-coating process for PEDOT:PSS (F HC Solar) square thin films (80 nm, 10 × 10 mm^2) under an applied lateral electric field of 3 V mm⁻¹.

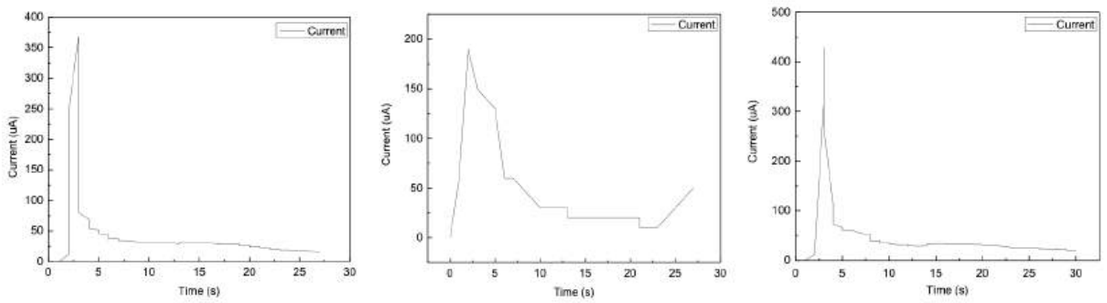

Figure 7.9. Real-time current evolution during the 30s spin-coating process for PEDOT:PSS (F HC Solar) rectangular thin films (80 nm, 10 × 8 mm^2) under an applied lateral electric field of 3 V mm⁻¹.

7.9.5 Conductive Atomic Force Microscope Analysis and Multiscale Charge Transport in PEDOT:PSS Thin Films

Conductive atomic force microscope (C-AFM) was employed to investigate the nanoscale charge transport behavior of PEDOT:PSS thin films prepared under different processing conditions. While macroscopic electrical measurements provide information on in-plane transport and anisotropy, C-AFM enables spatially resolved probing of vertical (cross-plane) charge transport pathways. The combination of these two complementary techniques allows direct correlation between local

conduction mechanisms and macroscopic electrical performance. In C-AFM measurements, a bias voltage applied between the conductive tip and the bottom electrode enables mapping of vertical current flow across the film thickness, thereby providing insight into nanoscale transport channels associated with PEDOT-rich regions. Furthermore, the C-AFM current maps allow quantitative estimation of the effective cross-plane electrical conductivity using the relation [37]:

$$\sigma = \frac{I \cdot L}{V \cdot A} \qquad (7.4)$$

where I is the total current obtained by summing the current values of all pixels within the scanned area, L is the film thickness, V is the applied tip-sample bias voltage, and A is the scan area. This approach, previously reported in the literature [37], enables conversion of nanoscale current distributions into average vertical conductivity values, providing a direct link between local transport pathways and bulk electrical behavior. A summary of the measured current, applied bias voltage, film thickness, surface roughness, and extracted cross-plane conductivity is provided in Tables 7.6 and 7.7, corresponding to samples prepared with and without an applied lateral electric field, respectively.

7.9.6 C-AFM Analysis of PEDOT:PSS Thin Films Prepared Under Lateral Electric Field

Figures 7.10 (a-h) present the simultaneously acquired current and topography images for samples 6 and 7, deposited under identical conditions (3 V/mm applied field, ~80 nm thickness, glass substrate) and measured at a tip-sample bias of 400 mV. At the 2 × 2 μm² scan scale (a-d), both samples exhibit a highly non-uniform current distribution characterized by numerous localized conductive regions embedded within a comparatively insulating background. These bright current "hot spots" are consistently observed across both samples, indicating good reproducibility of the field-assisted deposition process. The lateral homogeneity of the current distribution over micrometer-scale areas suggests that the observed nanoscale transport features are intrinsic to the PEDOT:PSS film. Higher-resolution scans performed on Sample 7 over 1 × 1 μm² and 0.5 × 0.5 μm² areas (e-h) reveal more clearly resolved conductive domains with characteristic lateral dimensions on the order of tens of nanometers. These localized conductive features are attributed to PEDOT-rich domains that are either exposed at or located near the film surface, while the surrounding low-current regions are associated with PSS-rich insulating phases. The persistence of this heterogeneous transport pattern across multiple length scales confirms that charge transport in PEDOT:PSS films occur through a percolative network of discrete conductive pathways rather than uniformly across the surface.

Comparison between the current and topography maps indicates only a weak direct correlation between surface height variations and local current magnitude. Although some elevated surface features exhibit enhanced conductivity, many conductive hot spots appear independent of pronounced topographical protrusions. This observation is consistent with previous reports and suggests that vertical transport is primarily governed by subsurface PEDOT connectivity and local compositional variations rather than purely by surface roughness. Importantly, the overall current levels and density of conductive pathways observed in the E-field-treated samples are significantly higher than those measured for films prepared without an applied electric field (discussed in the following section). This behavior indicates that the lateral electric field applied during spin coating promotes enhanced vertical connectivity between PEDOT-rich domains. The field-assisted solidification likely facilitates partial polymer chain reorientation and redistribution of PEDOT and PSS phases, resulting in improved interdomain coupling and a higher density of effective charge transport channels. Furthermore, the similarity in current distribution patterns between samples 6 and 7 confirms that the electric-field-induced morphological modification is robust and reproducible under identical processing conditions. The enhanced nanoscale conductivity observed by C-AFM is consistent with the macroscopic increase in electrical conductivity reported earlier in this chapter for films processed under an applied field. Although electric-field-assisted deposition significantly enhances local charge transport by increasing the number and connectivity of PEDOT-rich domains, the accompanying increase in surface roughness suggests that conductivity enhancement is not achieved without morphological consequences. To better evaluate this trade-off and isolate the role of electric-field-induced reorganization, the following section compares these results with PEDOT:PSS films prepared without an applied electric field and with $CuCl_2$-doped formulations. This comparison enables a direct assessment of how processing-induced microstructural changes influence nanoscale charge transport pathways.

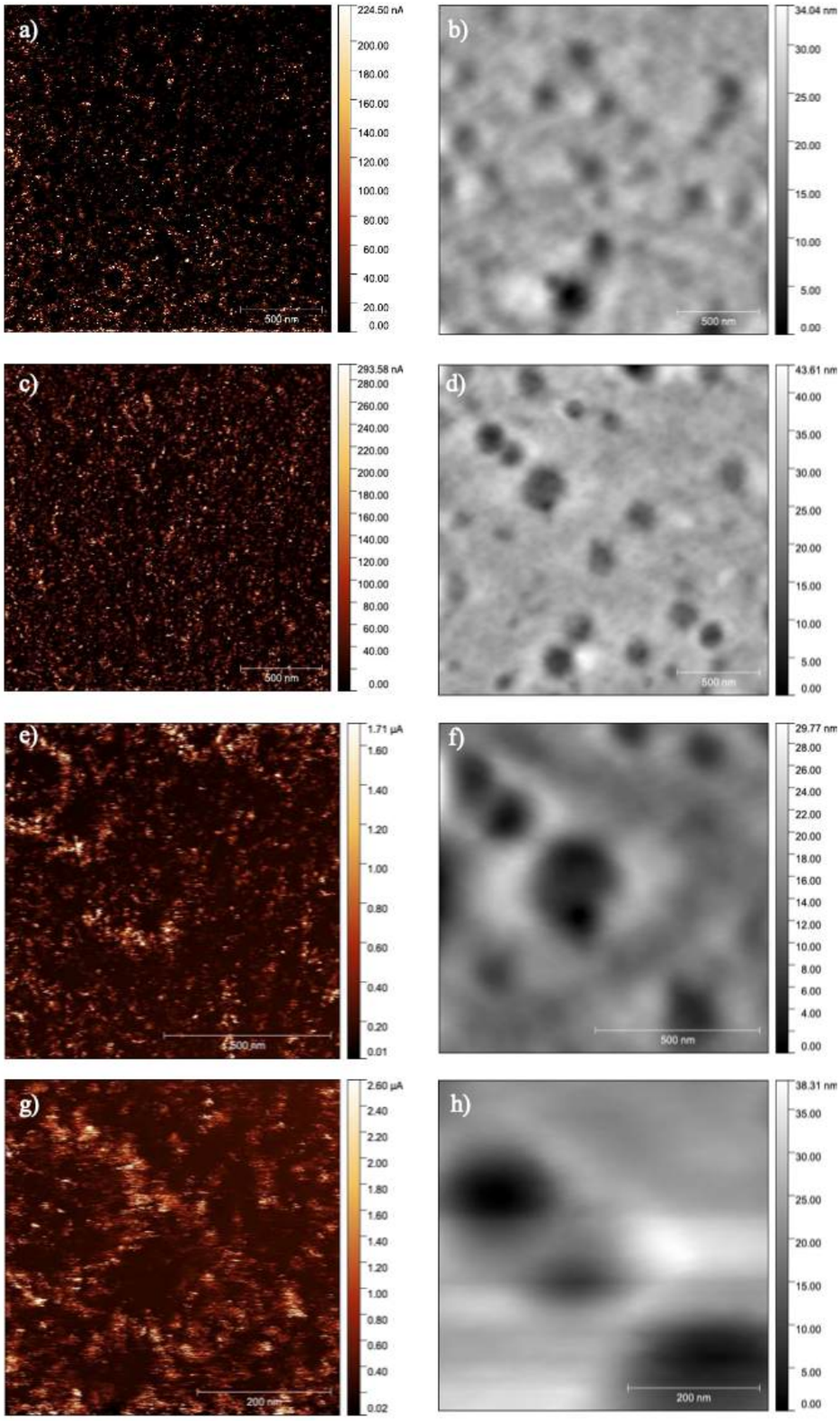
a)
224.50 nA
200.00
180.00
160.00
140.00
120.00
100.00
80.00
60.00
40.00
20.00
0.00
500 nm
b)
34.04 nm
30.00
25.00
20.00
15.00
10.00
5.00
0.00
500 nm
c)
293.58 nA
280.00
260.00
240.00
220.00
200.00
180.00
160.00
140.00
120.00
100.00
80.00
60.00
40.00
0.00
500 nm
d)
43.61 nm
40.00
35.00
30.00
25.00
20.00
15.00
10.00
5.00
0.00
500 nm
e)
1.71 µA
1.60
1.40
1.20
1.00
0.80
0.60
0.40
0.20
0.01
500 nm
f)
29.77 nm
28.00
26.00
24.00
22.00
20.00
18.00
16.00
14.00
12.00
10.00
8.00
6.00
4.00
0.00
500 nm
g)
2.60 µA
2.40
2.20
2.00
1.80
1.60
1.40
1.20
1.00
0.80
0.60
0.40
0.02
200 nm
h)
38.31 nm
35.00
30.00
25.00
20.00
15.00
10.00
5.00
0.00
200 nm

Figure 7.10. Conductive atomic force microscopy (C-AFM) current maps and corresponding topography images of PEDOT:PSS thin films prepared under a lateral electric field (3 V mm^{-1}) during spin coating. (a-b) Sample 6 measured over a 2 × 2 μm^2 area, showing current distribution and surface morphology. (c-d) Sample 7 measured over a 2 × 2 μm^2 area. (e-f) Sample 7 measured over a 1 × 1 μm^2 area. (g-h) Sample 7 measured over a 0.5 × 0.5 μm^2 area. All measurements were performed using a tip-sample bias of 400 mV. Bright regions in the current maps correspond to locally enhanced conductive pathways associated with PEDOT-rich domains, while the topography images illustrate the nanoscale surface morphology of the films.

7.9.7 Comparison with Films Prepared Without Electric Field and Doped Samples

Figure 7.11 (a-h) presents the C-AFM current maps and corresponding topography images of PEDOT:PSS thin films prepared without applying an external electric field during spin coating. For the pristine PEDOT:PSS (FHC Solar) film with a thickness of 480 nm (Figures a-d), the current images reveal a heterogeneous distribution of localized conductive regions embedded within a predominantly low-conductivity background. The brighter areas correspond to PEDOT-rich domains that provide preferential vertical transport pathways, while the darker regions are attributed to PSS-rich insulating phases. Similar current distribution patterns are observed at both 1 × 1 μm^2 and 0.5 × 0.5 μm^2 scan areas, indicating that the nanoscale heterogeneity is intrinsic to the film morphology and persists across different length scales. The corresponding topography images show a comparatively smoother surface than that observed for field-treated samples, consistent with the reduced degree of PEDOT domain aggregation in the absence of electric-field-induced chain reorganization. For the water-diluted PEDOT:PSS (1.3%) film (e-f) and the $CuCl_2$-doped PEDOT:PSS sample (g-h), noticeable changes in both morphology and current distribution are observed. While water dilution leads to a more uniform surface morphology with moderate conductive contrast, the incorporation of $CuCl_2$ unexpectedly results in a reduced density of conductive hotspots and lower overall current levels. This suggests that metal salt incorporation does not necessarily enhance vertical charge transport and may instead disrupt PEDOT domain connectivity or increase carrier scattering. Compared to the films processed under an applied electric field, all non-field-treated samples exhibit a lower density of conductive pathways and reduced local current intensity, confirming that electric-field-assisted deposition is the dominant factor contributing to enhanced surface conductivity, albeit at the expense of increased surface roughness.

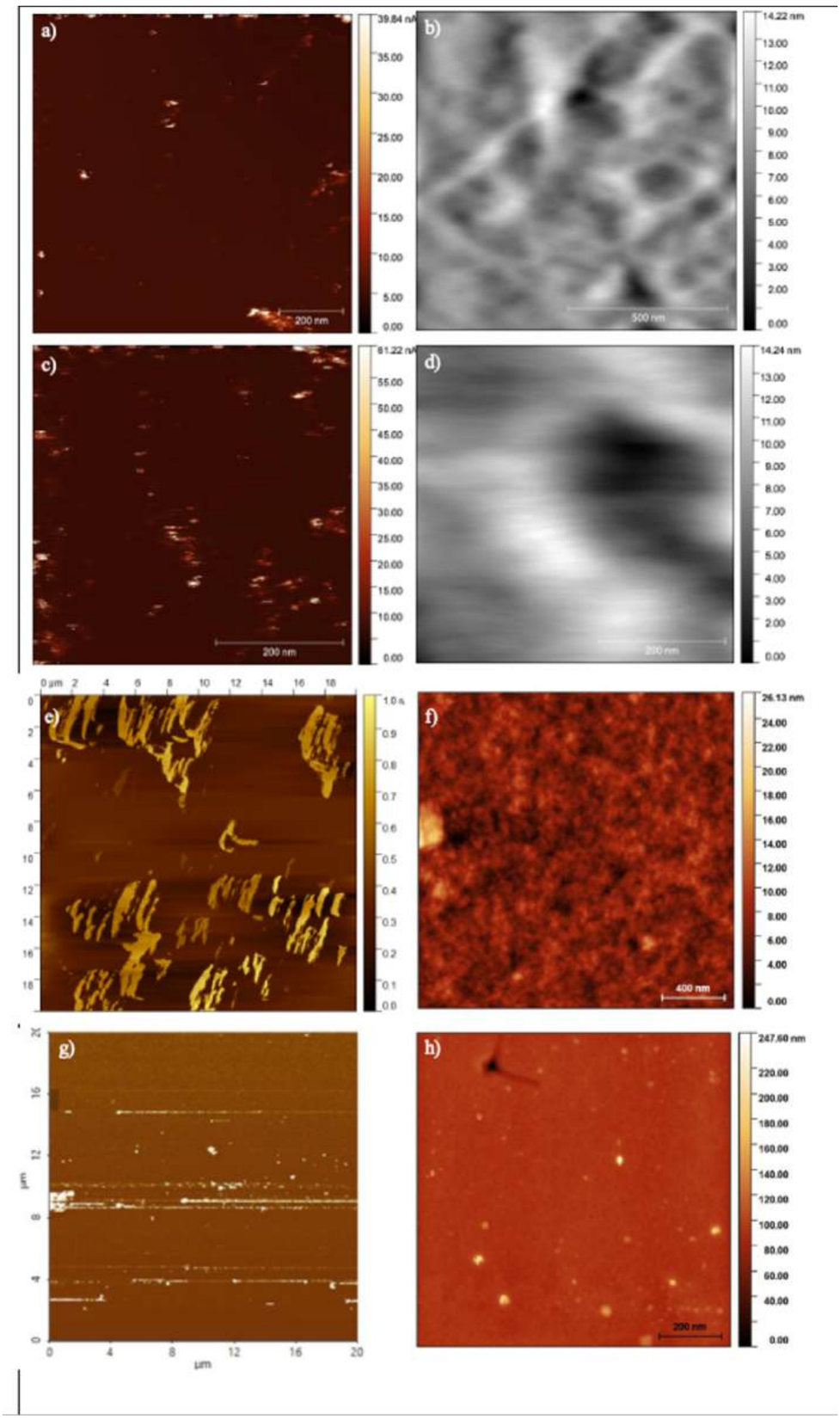
a)
200 nm
b)
500 nm
c)
200 nm
d)
200 nm
e)
f)
400 nm
g)
µm
h)
200 nm

Figure 7.11. C-AFM current and corresponding topography images of PEDOT:PSS thin films prepared without an applied electric field: (a-d) pristine PEDOT:PSS (~480 nm) at 1 × 1 μm² and 0.5 × 0.5 μm² scan areas; (e-f) water-diluted PEDOT:PSS (1.3%); (g-h) $CuCl_2$-doped PEDOT:PSS.

Table 7.6. Summary of the measured current values applied tip-sample bias voltages, film thicknesses, surface roughness, and the corresponding extracted local cross-plane electrical conductivities for PEDOT:PSS thin films prepared under an applied lateral electric field.

Sample	L (nm)	V (mV)	A (μm²)	I	σ (S/cm)	R_q (nm)	R_a (nm)
6	80	400	2×2	224.5nA	1.12×10^{-4}	3.4	2.58
7	80	400	2×2	293.5nA	1.47×10^{-4}	4.4	3.0
7	80	400	1×1	1.7μA	3.4×10^{-3}	3.9	2.9
7	80	400	0.5×0.5	2.6 μA	2.08×10^{-2}	7.6	5.8

Table 7.7. Summary of the measured current values applied tip-sample bias voltages, film thicknesses, surface roughness, and the corresponding extracted cross-plane electrical conductivities for PEDOT:PSS thin films prepared without the application of a lateral electric field.

Sample	L (nm)	V (mV)	A (μm²)	I	σ (S/cm)	R_q (nm)	R_a (nm)
PEDOT:PSS (FHC Solar)	480	500	1×1	39.8nA	3.82×10^{-4}	1.7	1.3
PEDOT:PSS (FHC Solar)	480	500	0.5×0.5	61.2nA	2.35×10^{-3}	2.8	2.3
PEDOT:PSS 3-4%	480	500	2×2	20nA	4.8×10^{-5}	2.9	6.2
PEDOT:PSS 1.3% + $CuCl_2$	480	500	2×2	10nA	2.4×10^{-5}	1.8	1.4

7.9.8 Correlation Between Cross-Plane and In-Plane Transport Properties

An important outcome of this study is the simultaneous characterization of charge transport along both in-plane and cross-plane directions. While C-AFM measurements probe vertical transport pathways by directly measuring local current flow across the film thickness, macroscopic electrical measurements under lateral electrode configurations provide information on in-plane conductivity and anisotropy induced by electric-field-assisted processing. By combining these two approaches, it is possible to establish a direct link between nanoscale transport pathways and macroscopic electrical behavior. The increased density of conductive hotspots observed in C-AFM measurements for electric-field-treated films correlates strongly with the enhanced in-plane conductivity anisotropy measured using the Van der Pauw configuration. This demonstrates that electric-field-induced molecular reorganization not only modifies lateral charge transport but also improves vertical connectivity between PEDOT domains.

7.10 Conclusion

This chapter demonstrates that applying a lateral electric field during spin coating and solidification induces strong and reproducible directional in-plane electrical anisotropy in PEDOT:PSS thin films. The observed anisotropy is attributed to electric-field-induced reorganization of PEDOT:PSS domains during solvent evaporation, leading to direction-dependent conductive pathways. Real-time in situ current monitoring together with conductive AFM measurements confirms that the electrical and structural evolution occurs dynamically during film formation. An important originality of this work lies in the development of a custom-designed spin-coating system capable of simultaneously applying a lateral electric field and performing real-time electrical monitoring throughout the deposition and solidification process. Unlike conventional post-treatment approaches, the present method enables direct manipulation of the PEDOT:PSS morphology while the polymer remains in a mobile state. This is done with very weak electric fields which do not harm the chemical integrity of the organic molecules. Overall, the results demonstrate that electric-field-assisted spin coating provides an effective strategy for engineering directional charge transport in conducting polymer thin films for future electronic and optoelectronic applications.

7.11 References

[1] M. N. Gueye, A. Carella, M. Faure-Vincent, R. Demadrille, and J.-P. Simonato, “Progress in understanding structure and transport properties of PEDOT-based materials: A critical review,” *Prog. Mater. Sci*., **108**, 100616, (2020).

[2] M. Kong, M. Garriga, J. S. Reparaz, and M. I. Alonso, “Advanced optical characterization of PEDOT:PSS by combining spectroscopic ellipsometry and Raman scattering,” *ACS Omega*, **7**, 39429–39436, (2022).

[3] S. Kirchmeyer and K. Reuter, “Scientific importance, properties and growing applications of poly(3,4-ethylenedioxythiophene),” *J. Mater. Chem*., **15**, 2077–2088, (2005).

[4] J. Dong, Structure–Property and Film Formation Mechanism in PEDOT:PSS, Ph.D. dissertation, Univ. Groningen, Groningen, The Netherlands, 2021.

[5] A. M. Nardes, M. Kemerink, R. A. J. Janssen, J. A. M. Bastiaansen, N. M. M. Kiggen, B. M. W. Langeveld-Voss, A. J. J. M. van Breemen, and M. M. de Kok, “Microscopic understanding of the anisotropic conductivity of PEDOT:PSS thin films,” *Adv. Mater*., **19**, 1196–1200, (2007).

[6] A. W. Salamon, C. Mauger, J. D. Gale, K. B. Burke, L. Thomsen, N. Kirby, and A. N. Sokolov, “Thermal conductivity and elastic constants of PEDOT:PSS with high electrical conductivity,” *Macromolecules*, **48**, 585–591, (2015).

[7] L. Dong, S. Read, Y. Hou, Y. Shi, and Z. Wang, “Coupling electronic and phonon thermal transport in polymeric conductors,” *npj Comput. Mater*., **8**, (2022).

[8] D. Scheunemann and M. Kemerink, “Non-Wiedemann–Franz behavior of the thermal conductivity of organic semiconductors,” *Phys. Rev. B*, **101**, 075206, (2020).

[9] H. Sirringhaus, P. J. Brown, R. H. Friend, M. M. Nielsen, K. Bechgaard, B. M. W. Langeveld-Voss, A. J. H. Spiering, R. A. J. Janssen, E. W. Meijer, and P. Herwig, “Two-dimensional charge transport in self-organized, high-mobility conjugated polymers,” *Nature*, **401**, 685–688, (1999).

[10] N. S. Sariciftci, Conjugated Polymer Physics and Devices. Bellingham, WA, USA: SPIE Press, 2015.

[11] S.-I. Na, S.-S. Kim, J. Jo, and D.-Y. Kim, “Evolution of nanomorphology and anisotropic conductivity in solvent-modified PEDOT:PSS films for polymeric anodes of polymer solar cells,” *J. Mater. Chem*., **19**, 9045–9053, (2009).

[12] Q. Wei, M. Mukaida, K. Kirihara, and T. Ishida, “Experimental studies on the anisotropic thermoelectric properties of conducting polymer films,” *ACS Macro Lett*., **3**, 948–952, (2014).

[13] A. M. Nardes, R. A. J. Janssen, and M. Kemerink, “A morphological model for the solvent-enhanced conductivity of PEDOT:PSS thin films,” *Adv. Funct. Mater*., **18**, 865–871, (2008).

[14] M. Girtan, R. Mallet, M. Socol, and A. I. Stanculescu, “On the physical properties of PEDOT:PSS thin films,” *Mater. Today Commun*., **22**, 100735, (2020).

[15] A. M. Nardes, On the Conductivity of PEDOT:PSS Thin Films, Ph.D. dissertation, Eindhoven Univ. Technol., Eindhoven, The Netherlands, 2007.

[16] M. Singh, A. Kumar, D. K. Avasthi, Y. K. Vijay, and A. Mansingh, “Variable-range hopping conduction in conducting polymers,” *Phys. Rev. B*, **50**, 7007–7010, (1994).

[17] O. Ivanov, M. Yaprintsev, and E. Danshina, “Electric field effect on variable-range hopping conductivity in $Bi_{1.9}Lu_{0.1}Te_3$,” *J. Phys. Chem. Solids*, **124**, 247–252, (2019).

[18] A. N. Aleshin, H. J. Lee, S. W. Chu, J. S. Kim, and Y. W. Park, “One-dimensional transport in polymer nanofibers,” *Phys. Rev. B*, **69**, 214203, (2004).

[19] X. Crispin, F. Jakobsson, A. Crispin, P. Grim, C. Andersson, A. Volodin, C. van Haesendonck, M. Van der Auweraer, W. R. Salaneck, and M. Berggren, “The origin of the high conductivity of poly(3,4-ethylenedioxythiophene)-poly(styrenesulfonate) (PEDOT-PSS) plastic electrodes,” *Chem. Mater*., **18**, 4354–4360, (2006).

[20] Z. Fan and J. Ouyang, “Thermoelectric properties of PEDOT:PSS,” *Adv. Electron. Mater*., **5**, 1800769, (2019).

[21] J. Ouyang, Q. Xu, C.-W. Chu, Y. Yang, G. Li, and J. Shinar, "On the mechanism of conductivity enhancement in poly(3,4-ethylenedioxythiophene):poly(styrene sulfonate) film through solvent treatment," *Adv. Funct. Mater*., **15**, 203–208, (2005).

[22] M. S. Mahajan., "Changes in in-plane electrical conductivity of PEDOT:PSS thin films due to electric field induced dipolar reorientation," *RSC Adv*., **5**, 63954–63961, (2015).

[23] Y. Xia and J. Ouyang, "Significant conductivity enhancement of conductive poly(3,4-ethylenedioxythiophene):poly(styrenesulfonate) films through a treatment with organic carboxylic acids and inorganic acids," *Adv. Mater*., **2**, 2174–2177, (2009).

[24] J. Y. Kim, J. H. Jung, D. E. Lee, and J. Joo, "Enhancement of electrical conductivity of poly(3,4-ethylenedioxythiophene)/poly(4-styrenesulfonate) by a change of solvents," *Synth. Met*., 126, 311–316, (2002).

[25] J. L. Carter, Processing Optimization, Conductivity Enhancement & Adhesion Improvement of PEDOT:PSS Films, Ph.D. dissertation, School Metall. Mater., Univ. Birmingham, Birmingham, U.K., 2022.

[26] M. Kim, J. H. Park, J. Kim, Y. H. Jeong, and J. Joo, "Electrical and structural characterization of PEDOT:PSS films prepared by electric-field-assisted deposition," *Org. Electron*., **12**, 2145–2151, (2011).

[27] B. Winther-Jensen and K. West, "Stability of highly conductive poly(3,4-ethylenedioxythiophene)/poly(styrenesulfonate) (PEDOT:PSS)," *Macromolecules*, **37**, 4538–4543, (2004).

[28] A. M. Nardes, M. Kemerink, R. A. J. Janssen, J. A. M. Bastiaansen, N. M. M. Kiggen, B. M. W. Langeveld-Voss, A. J. J. M. van Breemen, and M. M. de Kok, "Anisotropic hopping conduction in spin-coated PEDOT:PSS thin films," *Phys. Rev. B*, **76**, 085208, (2007).

[29] A. M. Nardes, M. Kemerink, R. A. J. Janssen, J. A. M. Bastiaansen, N. M. M. Kiggen, B. M. W. Langeveld-Voss, A. J. J. M. van Breemen, and M. M. de Kok, "Conductivity, work function, and environmental stability of PEDOT:PSS thin films treated with sorbitol," *Org. Electron*., **9**, 727–734, (2008).

[30] K. van de Ruit, I. Katsouras, D. Bollen, T. van Mol, R. A. J. Janssen, D. M. de Leeuw, and M. Kemerink, "The curious out-of-plane conductivity of PEDOT:PSS," *Adv. Funct. Mater*., **23**, 5787–5793, (2013).

[31] X. Wang, M. Madsen, F. C. Krebs, and T. M. Larsen, “Anisotropic conductivity of cellulose–PEDOT:PSS composite materials studied with a generic 3D four-point probe tool,” *Org. Electron*., **62**, 132–138, (2018).

[32] G. Gaál, G. Hegedűs, B. Réti, G. Molnár, A. Magrez, and C. Visy, “High electrical anisotropic multilayered self-assembled organic films based on graphene oxide and PEDOT:PSS,” *Adv. Electron. Mater*., **7**, 2100255, (2021).

[33] S. Fujii, Y. Suzuki, J. Kawamata, and R. Tsunashima, “Large in-plane/out-of-plane anisotropic conduction in PEDOT-based hybrid films: Lamellar assemblies structured by mono-layered nanosheets,” *J. Mater. Chem. C*, **6**, 6272–6279, (2018).

[34] Y.-W. Kim., “Anisotropically conductive hydrogels with directionally aligned PEDOT:PSS in a PVA matrix,” *ACS Appl. Mater. Interfaces*, **16**, (2024).

[35] Z. Chen., “Construction of flexible, self-supporting, and in-plane anisotropic PEDOT:PSS thermoelectric films via the wet-winding approach,” *ACS Appl. Polym. Mater*., **5**, (2023).

[36] M. S. Mahajan., “Changes in in-plane electrical conductivity of PEDOT:PSS thin films due to electric field induced dipolar reorientation,” *RSC Adv*., **5**, 63954–63961, (2015).

[37] A. J. Diaz, H. Noh, T. Meier, and S. D. Solares, “High-stress study of bioinspired multifunctional PEDOT:PSS/nanoclay nanocomposites using AFM, SEM and numerical simulation,” *Beilstein J. Nanotechnol*., **8**, 2069–2082, (2017).